

University of Kentucky

UKnowledge

---

Theses and Dissertations--Chemistry

Chemistry

---

2016

## UNDERSTANDING DNA CONDENSATION BY LOW GENERATION (G0/G1) AND ZWITTERIONIC G4 PAMAM DENDRIMERS

Min An

University of Kentucky, man223@g.uky.edu

Digital Object Identifier: <http://dx.doi.org/10.13023/ETD.2016.194>

[Right click to open a feedback form in a new tab to let us know how this document benefits you.](#)

### Recommended Citation

An, Min, "UNDERSTANDING DNA CONDENSATION BY LOW GENERATION (G0/G1) AND ZWITTERIONIC G4 PAMAM DENDRIMERS" (2016). *Theses and Dissertations--Chemistry*. 58.  
[https://uknowledge.uky.edu/chemistry\\_etds/58](https://uknowledge.uky.edu/chemistry_etds/58)

This Doctoral Dissertation is brought to you for free and open access by the Chemistry at UKnowledge. It has been accepted for inclusion in Theses and Dissertations--Chemistry by an authorized administrator of UKnowledge. For more information, please contact [UKnowledge@lsv.uky.edu](mailto:UKnowledge@lsv.uky.edu).

## **STUDENT AGREEMENT:**

I represent that my thesis or dissertation and abstract are my original work. Proper attribution has been given to all outside sources. I understand that I am solely responsible for obtaining any needed copyright permissions. I have obtained needed written permission statement(s) from the owner(s) of each third-party copyrighted matter to be included in my work, allowing electronic distribution (if such use is not permitted by the fair use doctrine) which will be submitted to UKnowledge as Additional File.

I hereby grant to The University of Kentucky and its agents the irrevocable, non-exclusive, and royalty-free license to archive and make accessible my work in whole or in part in all forms of media, now or hereafter known. I agree that the document mentioned above may be made available immediately for worldwide access unless an embargo applies.

I retain all other ownership rights to the copyright of my work. I also retain the right to use in future works (such as articles or books) all or part of my work. I understand that I am free to register the copyright to my work.

## **REVIEW, APPROVAL AND ACCEPTANCE**

The document mentioned above has been reviewed and accepted by the student's advisor, on behalf of the advisory committee, and by the Director of Graduate Studies (DGS), on behalf of the program; we verify that this is the final, approved version of the student's thesis including all changes required by the advisory committee. The undersigned agree to abide by the statements above.

Min An, Student

Dr. Jason DeRouchey, Major Professor

Dr. Dong-Sheng Yang, Director of Graduate Studies

UNDERSTANDING DNA CONDENSATION BY LOW GENERATION (G0/G1)  
AND ZWITTERIONIC G4 PAMAM DENDRIMERS

---

Dissertation

---

A dissertation submitted in partial fulfillment of the  
requirements for the degree of Doctor of Philosophy in the  
College of Art and Science at the University of Kentucky

By

Min An

Lexington, Kentucky

Director: Dr. Jason DeRouchey

Assistant Professor of Department of Chemistry

Lexington, Kentucky

2016

Copyright © Min An

## ABSTRACT OF DISSERTATION

### UNDERSTANDING DNA CONDENSATION BY LOW GENERATION (G0/G1) AND ZWITTERIONIC G4 PAMAM DENDRIMERS

Cationic polymers have shown potential as gene delivery vectors due to their ability to condense DNA and protect it from cellular and restriction nucleases. Dendrimers are hyperbranched macromolecules with precisely defined molecular weights and highly symmetric branches stemming from a central core. The nanosize, tunable surface chemistries and ease of surface functionalization has made dendrimers an attractive alternative to conventional linear polymers for DNA delivery applications. The commercially available, cationic dendrimer poly(amidoamine) or PAMAM is the most widely studied dendrimer for use as a gene delivery vector. The aim of this dissertation is to provide an increased understanding of the packaging and forces within PAMAM–DNA complexes.

In Chapter 4, we will discuss the effect of molecular chain architecture on DNA-DNA intermolecular forces by examining DNA condensed by low generation (G0 & G1) PAMAM and comparing them to comparably charged linear arginine peptides. Using osmotic stress coupled with X-ray scattering, we are able to determine the structure and forces within dendrimer-DNA complexes, or dendriplexes. We show that PAMAM–DNA assemblies display significantly different physical behavior than linear cation–DNA assemblies. In Chapter 5, we examine the role of pH on condensation in these same low generation PAMAM-DNA complexes. PAMAM dendrimers have both terminal primary amines and internal tertiary amines with different pK<sub>a</sub>s of approximately 9 and 6, respectively. We show changes in the pH at condensation greatly influence the resulting packaging as well as the resulting phase behavior for PAMAM dendriplexes. In Chapter 6, we examine the packaging of DNA by G4 PAMAM as a function of the percent zwitterionic modification. Many cationic polymers, including PAMAM, have shown high transfection efficiency in cell culture and potential for in vitro and in vivo applications, but its development is hindered by cytotoxicity in many cell lines and tissues. We hypothesize that zwitterionic PAMAM (zPAMAM) represent a new means to tune polymer-DNA interactions through PAMAM surface charge potentially enhancing intracellular unpackaging while reducing cellular toxicity. These zPAMAM complexes are currently under investigation for their potential as safer and more efficient materials for DNA delivery.

Key words: PAMAM, dendrimer, DNA condensation, phase behavior, SAXS, osmotic pressure,

Min An

---

April 25<sup>th</sup>, 2016

---

Date

UNDERSTANDING DNA CONDENSATION BY LOW GENERATION (G0/G1)  
AND ZWITTERIONIC G4 PAMAM DENDRIMERS

By  
Min An

Dr. Jason DeRouchey

Director of Dissertation

Dr. Dong-Sheng Yang

Director of Graduate Studies

April 25<sup>th</sup> 2016

## **Acknowledgement**

As I move toward the end of an important and long journey in my life, I really need to say thank you to a lot of loved ones for their help during this period.

First of all, I would like to thank my advisor Dr. Jason DeRouchey. What I achieved in my doctoral studies depended on the guidance from Dr. DeRouchey. He taught me a lot of valuable skills and knowledge. He helped me in writing my papers and gave me guidance when I met problems in research. Also he is a good friend to talk to when I felt frustration with my work and life.

I need to thank Dr. Sean Parkin for helped me a lot with my small angle X-ray scattering experiments. Through his course and working on his x-ray instrument, I learned a lot about X-ray diffraction and scattering. He also provided me with a lot of useful suggestions in setting up our SAXS system. Without his help, I could not have finished collecting all my data for this work.

I also want to thank all of my committee members and Dr. Edward Spires (former committee member, since retired) for their help and guidance with my research.

Finally, I want to give a lot of thanks to my parents. I could not have survived doing my PhD abroad without my parents' support. They gave up a lot for me. Back in China, many children my age already take care of their parents in life and work. While completing my studies, I did not have the opportunity to help take care of my father when he suffered from stroke in hospital. During the last few years, my mother had been the backbone of my family in my absence. It has been difficult to be so far away and not be able to help in taking care of my parents while in Lexington. I really appreciate their strong support during this whole time.

## Table of Contents

ABSTRACT OF DISSERTATION .....	i
Acknowledgement .....	iii
Lists of Figures .....	vi
Lists of Table.....	ix
Chapter 1 Background and Introduction.....	1
1.1 Dendrimers.....	1
1.2 Applications of Dendrimers .....	4
1.3 DNA Condensation .....	6
1.4 Structure of PAMAM-DNA Complexes .....	8
Chapter 2 Small Angle X-ray Scattering (SAXS).....	11
2.1 Introduction.....	11
2.2 Production of X-rays.....	11
2.3 X-ray Scattering .....	12
2.4 Experimental Setup.....	15
2.5 SAXS Calibration .....	18
2.6 SAXS of Condensed DNA Samples .....	21
Chapter 3 Osmotic Pressure and Force Study .....	24
3.1 Theory of Osmotic Pressure.....	24
3.2 Vapor Pressure Osmometer.....	26
3.2.1 Theory of Operation.....	26
3.2.2 Operation Procedure to Measure Osmotic Pressure .....	27
3.2.3 Temperature versus Osmolality .....	28
3.3 Unit Conversion .....	30
3.4 Using Osmotic Stress for the Direct Measurement of Intermolecular Forces in DNA Condensates.....	31
3.5 Summary .....	36
Chapter 4 The Role of Cation Architecture on DNA Condensation .....	37
4.1 Introduction.....	37
4.2 Materials and Methods.....	39
4.2.1 Materials: .....	39
4.2.2 Sample Preparation .....	41
4.2.3 Critical Concentrations .....	41
4.2.4 Osmotic Stress .....	42
4.2.5 X-ray Scattering .....	42
4.2.6 Force Analysis.....	43
4.3 Results.....	44
4.3.1 Packing and Forces in DNA Condensed with G0-PAMAM, G1-PAMAM, Tetraarginine (R4), and Octaarginine (R8) .....	44
4.3.2 Role of pH on Equilibrium Spacings .....	49
4.3.3 Salt Dependence of R4, R8, G0-PAMAM and G1-PAMAM .....	51
4.4 Discussion .....	54
4.5 Conclusions.....	60
Chapter 5 Role of pH on DNA Condensation by Low Generation Dendrimers.....	62

5.1 Introduction.....	62
5.2 Materials and Methods.....	65
5.2.1 Materials .....	65
5.2.2 Sample Preparation.....	65
5.2.3 Osmotic Pressure.....	66
5.2.4 X-ray Scattering.....	67
5.2.5 Force Analysis.....	67
5.3 Results.....	69
5.4 Discussion.....	78
5.5 Conclusion .....	84
Chapter 6 Packaging of DNA by G4 PAMAM and Zwitterionic G4 PAMAM.....	86
6.1 Introduction.....	86
6.2 Material and Methods .....	88
6.2.1 Material .....	88
6.2.2 pUC18 Plasmid Transformation into E. coli.....	88
6.2.3 Plasmid Extraction .....	89
6.2.4 Gel Retardation Assay.....	90
6.2.5 Dissociation of DNA from Complexes .....	90
6.2.6 Dynamic Light Scattering (DLS) Measurements .....	91
6.2.7 Sample Preparation for X-ray Analysis .....	91
6.2.8 Small Angle X-ray Scattering .....	92
6.3 Results.....	93
6.3.1 Complex Formation Detected by Agarose Gel Retardation Assay .....	93
6.3.2 Stability of zPAMAM/DNA Complexes.....	93
6.3.3 Effect of Percent Modification on Particle Size of zPAMAM Dendriplexes .....	95
6.3.4 Structural Studies of G4 PAMAM/DNA .....	97
6.3.5 Structural Studies of zPAMAM/DNA .....	106
6.3.6 Phase Behavior of PAMAM/DNA and zPAMAM/DNA as a Function of Added Salt Concentration .....	112
6.4 Discussion .....	117
6.5 Conclusions.....	121
Chapter 7 Summary and Future Perspective.....	123
Reference .....	128
Vita.....	141

## List of Figures

<b>Figure 1.1</b> The structure of G0 (left) and G1 (right) PAMAM dendrimers with ethylenediamine cores.....	2
<b>Figure 1.2</b> A dimensionally scaled comparison of a series of PAMAM dendrimers (G4-G7) with a variety of comparably sized biological assemblies .....	3
<b>Figure 1.3</b> The multi-step processes for nucleic acid delivery to cells .....	5
<b>Figure 1.4</b> The electrostatic zipper model used to explain DNA condensation by linear polycations .....	7
<b>Figure 1.5</b> The hydration model used to explain DNA condensation .....	8
<b>Figure 1.6</b> Proposed structures of Dendrimer:DNA complexes including (a) square columnar package, (b) beads-on-string structure, and (c) hexagonally packaged structure .....	10
<b>Figure 2.1</b> Scattering of X-rays by well-organized structure .....	14
<b>Figure 2.2</b> Experimental in-house setup for SAXS at the University of Kentucky. ....	16
<b>Figure 2.3</b> Components of the sample mount used for SAXS .....	17
<b>Figure 2.4</b> SAXS diffraction pattern of AgBeh standard shown by Fit2D. ....	19
<b>Figure 2.5</b> Small-angle X-ray scattering profile of silver behenate .....	20
<b>Figure 2.6</b> Basic geometry of scattering involving the incident beam, the sample, the scattered beam, and the detector .....	20
<b>Figure 2.7</b> Sketch of the condensed DNA and resulting diffraction pattern as measured by SAXS. ....	22
<b>Figure 2.8</b> (left) A typical 2-D SAXS pattern obtained from cation condensed DNA. The radius of the ring on the left gives the Bragg spacing ( $D_{Br}$ ), i.e., the spacing between packed layers of the condensed DNA. (right) Cartoon depiction of the hexagonal packaging of DNA rods shown end on showing the geometric relationship between $D_{Br}$ and the interhelical DNA spacing $D_{int}$ .....	23
<b>Figure 2.9</b> Typical SAXS signal of DNA complexes.....	23
<b>Figure 3.1</b> Illustration of osmosis .....	24
<b>Figure 3.2</b> Typical plot of thermocouple temperature versus time as the VPO instrument cycles through the four step program described in 3.2.2 .....	29
<b>Figure 3.3</b> Illustration of DNA arrays under osmotic stress .....	33
<b>Figure 3.4</b> Idealized osmotic stress force curves for condensed DNA (red) and free DNA (black).....	35
<b>Figure 4.1</b> UV-vis absorption spectra of DNA in buffer solution .....	40
<b>Figure 4.2</b> Osmotic force stress curves are shown for DNA condensed by low generation (G0 and G1) PAMAM.....	45
<b>Figure 4.3</b> Osmotic stress force curves are shown for DNA condensed by tetraarginine (R4) and octaarginine (R8) peptides .....	46
<b>Figure 4.4</b> Small-angle X-ray scattering (SAXS) profiles of DNA assemblies condensed by R4, R8, G0-PAMAM, and G1-PAMAM in 10 mM Tris, pH 7.5	

.....	48
<b>Figure 4.5</b> Effect of changing pH at condensation.....	49
<b>Figure 4.6</b> (A) Bragg spacing dependence ( $D_{Br} = 2\pi/Q_{100}$ ) vs added NaCl concentration for R4, R8, G0 and G1-DNA systems. (B) The change in the Bragg spacing relative to $D_{Br}$ in 10 mM Tris without added salt.....	53
<b>Figure 4.7</b> Scattering profiles for DNA assemblies condensed by R4, R8, G0-PAMAM and G1-PAMAM at 10 mM Tris, pH 7.5 and with higher added NaCl concentration .....	54
<b>Figure 5.1</b> Osmotic stress force curves are shown for G0-PAMAM/DNA as a function of pH at condensation .....	69
<b>Figure 5.2</b> Osmotic stress force curves are shown for G1-PAMAM/DNA as a function of pH at condensation .....	70
<b>Figure 5.3</b> Dependence of the free energy contributions, $\Delta G_R$ (open) and $\Delta G_A$ (filled), evaluated at 25 Å for G0- and G1-PAMAM condensed DNA as a function of the inverse net charge, $N$ , of the PAMAM estimated for the various pH's used in this study.....	73
<b>Figure 5.4</b> (A) Bragg spacing dependence as a function of added NaCl concentration for G0-DNA and (B) G1-DNA condensed systems at different pHs. (C) and (D) plot the change in the Bragg spacing relative to $D_{Br}$ in 10 mM monovalent buffer without added salt ( $D_{Br,eq}$ ).....	75
<b>Figure 5.5</b> Scattering profiles for G1-DNA assemblies at (A) pH 4 and (B) pH 8 for both low salt and high salt conditions .....	77
<b>Figure 5.6</b> (A) Normalized $D_{Br}$ spacing and (B) in-plane correlation lengths, $\xi = 2\pi/\Delta Q_{Br}$ , for DNA condensed with G1-PAMAM at different pH as a function of the salt concentration normalized by the critical salt concentration for each system ( $c/c^*$ ) .....	78
<b>Figure 6.1</b> Agarose gel electrophoresis retardation of pUC18 plasmid DNA by zwitterionic PAMAM polyplexes .....	94
<b>Figure 6.2</b> Stability of zwitterionic G4 PAMAM polyplexes to competition with anionic dextran sulfate (DS) .....	96
<b>Figure 6.3</b> Evolution of G4 PAMAM/DNA assembly structure with time made by the low salt preparation method.....	99
<b>Figure 6.4</b> The X-ray scattering profiles of DNA condensed by G4-PAMAM dendrimer by high salt preparation at different time points.....	100
<b>Figure 6.5</b> X-ray scattering intensity profiles for G4-PAMAM polyplexes after 2 weeks.....	101
<b>Figure 6.6</b> The X-ray scattering profiles of reformed G4-PAMAM complexes by high salt preparation.....	102
<b>Figure 6.7</b> Scattering profiles of DNA condensed by G4-PAMAM at different N/P ratios using (A) the high salt preparation and (B) the low salt preparation method described in methods.....	104
<b>Figure 6.8</b> High salt prepared G4-PAMAM/DNA complexes condensed at different pH.....	105
<b>Figure 6.9</b> Low salt prepared G4-PAMAM/DNA complexes condensed at	

different pH.....	108
<b>Figure 6.10</b> High salt prepared zPAMAM/DNA complexes as a function of the percent modification of the G4 PAMAM surface (A) Scattering profiles for PAMAM/DNA condensed at pH 7.5 after two weeks equilibration. (B) Calculated Bragg spacing. Packaging within the zPAMAM/DNA scales with the percent zwitterionic nature of the dendrimer. ....	110
<b>Figure 6.11</b> Scattering profiles of zPAMAM/DNA condensed using the high salt method compared to unmodified G4 PAMAM/DNA complexes formed by low (pink line) and high salt preparation (black line).....	111
<b>Figure 6.12</b> Scattering profiles of z-PAMAM/DNA complexes made by low salt preparation .....	112
<b>Figure 6.13</b> Time evolution of X-ray scattering profiles of zPAMAM/DNA complexes .....	114
<b>Figure 6.14</b> Bragg spacings for G4 PAMAM/DNA as a function of increasing added NaCl concentration.....	115
<b>Figure 6.15</b> Salt effects on z-PAMAM/DNA complexes.....	116
<b>Figure 6.16</b> The relative changes of $D_{Br}$ for different z-PAMAM complexes as a function of NaCl concentration.....	117
<b>Figure 6.15</b> The SAXS profiles of dendriplexes as $dp=0.5$ at different N/P ratios .....	121

### List of Tables

<b>Table 1.1</b> Physical data for PAMAM dendrimers (ethylenediamine core) .....	3
<b>Table 2.1</b> The scattering angles and the $d$ -spacings of AgBeh obtained by CuK $\alpha$ radiation analysis .....	21
<b>Table 4.1</b> The equilibrium interhelical spacings ( $\pm 0.1$ Å) from direct X-ray measurements and repulsive and attractive force component contributions to osmotic pressures ( $\pm 0.5\%$ ) and free energies ( $\pm 0.5\%$ ) at 25 Å calculated from fits to force curves are shown for DNA condensed by R4, R8, G0- and G1-PAMAM.....	47
<b>Table 4.2</b> Effect of changing buffer pH after condensation for low generation PAMAM-DNA complexes .....	51
<b>Table 5.1</b> The equilibrium interhelical spacings ( $\pm 0.1$ Å) from x-ray measurements and repulsive and attractive force component contributions to osmotic pressures and free energies ( $\pm 5\%$ ) for G0 and G1 PAMAM condensed DNA at different pHs .....	71
<b>Table 6.1</b> DLS table of hydrodynamic diameter of dendrimer/DNA complexes vs zwitterionic modification percent .....	97

## Chapter 1 Background and Introduction

In this study, we are interested in understanding the self-assembly behavior of DNA condensed by highly branched, cationic PAMAM dendrimer molecules. In this introductory chapter, we will describe dendrimers and discuss their potential applications. We will then give some background on DNA condensation as well as discuss recent structural studies on PAMAM-DNA complexes. Lastly, we will briefly discuss our research motivation and introduce the specific projects described in this dissertation.

### 1.1 Dendrimers

Dendrimers are highly branched synthetic macromolecules which have a highly symmetric, tree-like geometry and a well-defined molar mass.<sup>1,2</sup> The synthesis of dendrimers was first discovered in the late 1970s by Fritz Vogtle and early 1980s by Donald Tomalia and coworkers and the research lab of George Newkome. Dendrimers are macromolecules grown in a highly controlled, step-wise manner consisting of symmetric branching units built around a small molecule core. Dendrimers consist of three central components: a central core, interior dendritic branch structures and exterior functional surface groups. Typically dendrimers are grown through an iterative process resulting in a new generation of dendrimer. Increasing generations result in dendrimers with larger molecular weights, larger molecule diameters, and twice the number of reactive surface groups of the proceeding generation. One of the first dendrimers to be synthesized was the water soluble polyamidoamine (PAMAM), referred to as Starburst polymers by Tomalia and coworkers, which consists of repetitively branched subunits containing amide and amine functionalities.<sup>3</sup> PAMAM is synthesized by successive reactions of an amine to methyl acrylate by Michael's addition followed by amidation with ethylene diamine resulting in amines capable of further reaction or generation growth. The structure of zero and first generation (G0 and G1) PAMAM are shown in Figure 1.1 where ethylene diamine was used as the core material. As depicted in Figure 1.1, PAMAM consists of dendritic branches containing tertiary amines as well as functional surface groups consisting of primary

amines. At physiological pH, the PAMAM molecules are positively charged due primarily to the primary amines. Polyionic dendrimers, such as PAMAM, has varying changes in size, shape and molecule flexibility as a function of increasing generation

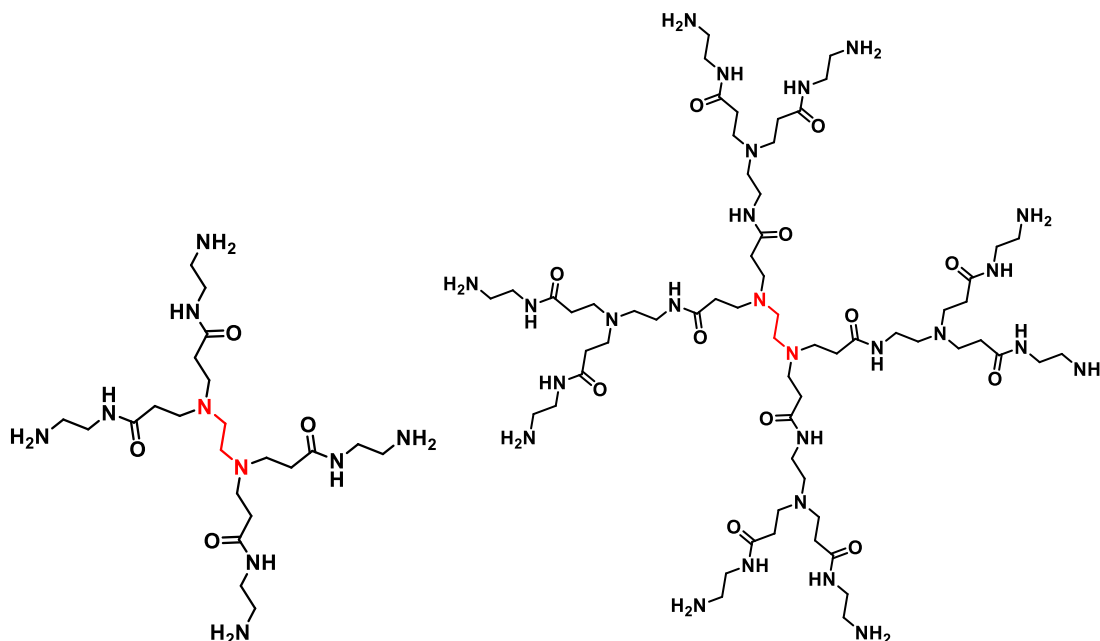


**Figure 1.1** The structure of G0 (left) and G1 (right) PAMAM dendrimers with ethylenediamine cores.

number. Dendrimer size and charge are systematically tunable through generation number and control of the surface functional chemistry. The PAMAM dendrimer family has sizes and contours that closely match many important proteins and biologically important assemblies as shown in Figure 1.2 below. For example, compared to proteins, G3-G5 PAMAM dendrimers built from ammonia core molecules have sizes and shapes similar to insulin (~30 Å), cytochrome C (~40 Å) and hemoglobin (~55 Å), respectively. Larger generation PAMAM have sizes comparable to other bioassemblies including the lipid bilayer (G5 PAMAM) or DNA-histone complex (G7 PAMAM). Table 1.1 shows the basic physical properties for commercially available G0-G10 PAMAM dendrimers (Dendritech) with ethylene diamine cores. As shown, with each increasing generation number, there is an approximate doubling of the dendrimer molar mass as well as doubling in the number

of surface functional groups. For unmodified PAMAM, these surface groups are primary amines.

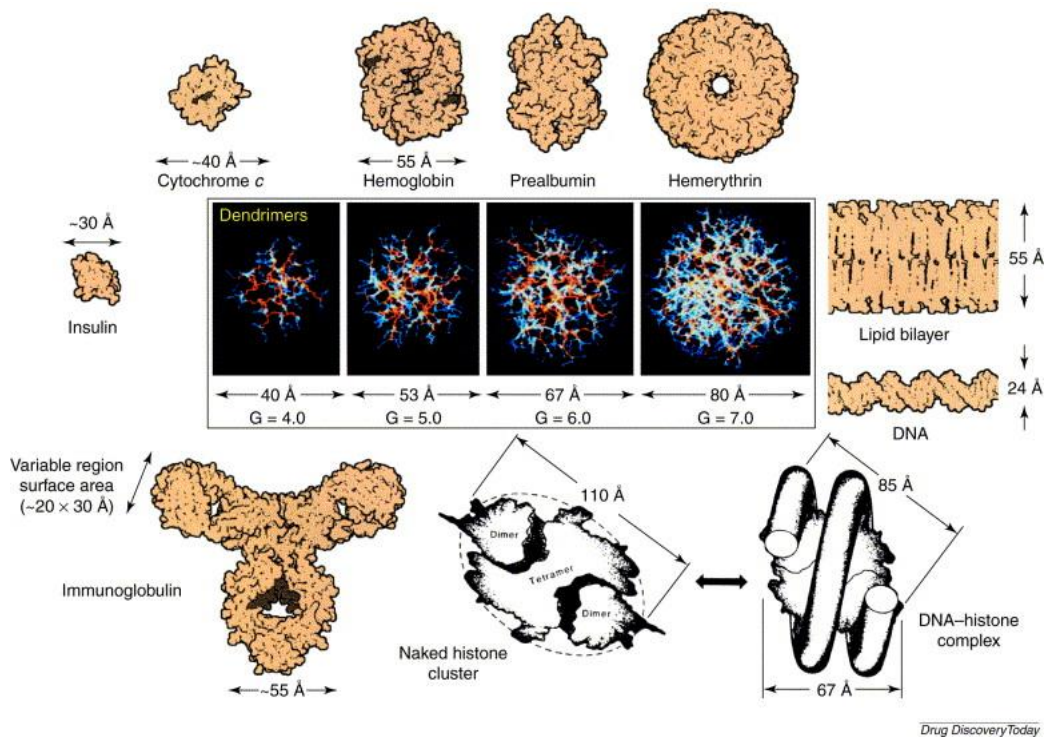


**Figure 1.2** A dimensionally scaled comparison of a series of PAMAM dendrimers (G4-G7) with a variety of comparably sized biological assemblies.<sup>4</sup> (Reprint from reference: Esfand, R. et al. *Drug Discovery Today* **2001**, *6*, Page:430.)

**Table 1.1** Physical data for PAMAM dendrimers (ethylenediamine core) (Data from Dendritech®). G0, G1 and G4 PAMAM were used in this work.

Generation	MW (g·mol <sup>-1</sup> )	Primary amines	Total amines	Measured diameter (Å)
0	517	4	6	15
1	1,430	8	14	22
2	3,256	16	30	29
3	6,909	32	62	36
4	14,215	64	126	45
5	28,826	128	254	54
6	58,048	256	510	67

## 1.2 Applications of Dendrimers

Dendrimers are man-made macromolecules that consist of three critical architectural features: (1) a surface containing a high concentration of potentially reactive functional groups (2) interior void volumes created by the multiple branched units of monomers and (3) a core to which the dendrons are attached. Dendrimers have several unique properties compared to most synthetic macromolecules and their unique structure and size range have a great impact on their physical and chemical properties. These properties include a monodisperse molecular weight, tunable size, variable concentration of functional surface groups and the presence of internal cavities for a wide range of applications. Tailoring the functional surface groups also allows for the further varying of the dendrimer solubility, nonimmunogenicity and biocompatibility making them attractive candidates for biomedical and nanotechnological applications.

In recent years, the applications of dendrimers have received a great deal of attention. Dendrimers may interact with small guest molecules either at the surface (exo-complexation) or in the dendrimer internal void space (endo-complexation) which makes them useful candidates for sensors. For example, recent work has highlighted the potential of dendrimers to detect heavy metals in the environment.<sup>5</sup> Commercially available PAMAM and PPI (polypropyleneimine) dendrimers have been used as MRI contrast agents to improve clinical diagnostics<sup>6</sup> or used in conjunction with transfection agents to label and isolate particular cells.<sup>7</sup> Boronated PAMAM have shown potential as efficient anti-cancer reagents<sup>8</sup> and phosphorus containing dendrimers have shown anti-prion activity.<sup>9</sup> Dendrimers are promising candidates for drug delivery due to the ability to modify the cavities inside the dendritic structure to incorporate hydrophobic and hydrophilic drugs.<sup>10-12</sup> It has even been suggested that high generation dendrimers, comparable in size to histones, may be useful systems for the study of the regulation of gene expression *in vitro*.<sup>13,14</sup> Unlike real proteins, a significant advantage of dendrimers over real biological system is their robustness to a wide range of environments.

In non-viral gene therapy, synthetic cationic vectors, such as polyethyleneimine (PEI), are used to form nanoparticles through electrostatically interacting with DNA or RNA. The gene delivery vectors are often polymeric and must be designed to overcome a number of extracellular barriers to achieve successful gene delivery. Successful materials must bind and protect the DNA, form sufficiently small and stable nanoparticles for cell internalization, mediate endocytotic vesicle escape as well as ultimately release the nucleic acid cargo for transcription.<sup>13-16</sup> A schematic of the processes involved in intracellular polyplex trafficking is shown in Figure 1.3. The precise chemistry and high tunability of cationic dendrimers, such as PAMAM and PPI, make them promising candidates for engineering new materials with improved structure-function activities. Compared to other non-viral vectors, PAMAM has shown lower toxicity and a lower chance to induce humoral immune responses.<sup>17</sup> PAMAM has also been shown effective for siRNA delivery into cells.<sup>18</sup> The high variability and precision in chemical composition available in dendrimers makes them promising candidates for understanding structure-function activities to better engineer materials capable of optimizing the various steps in successful gene delivery.

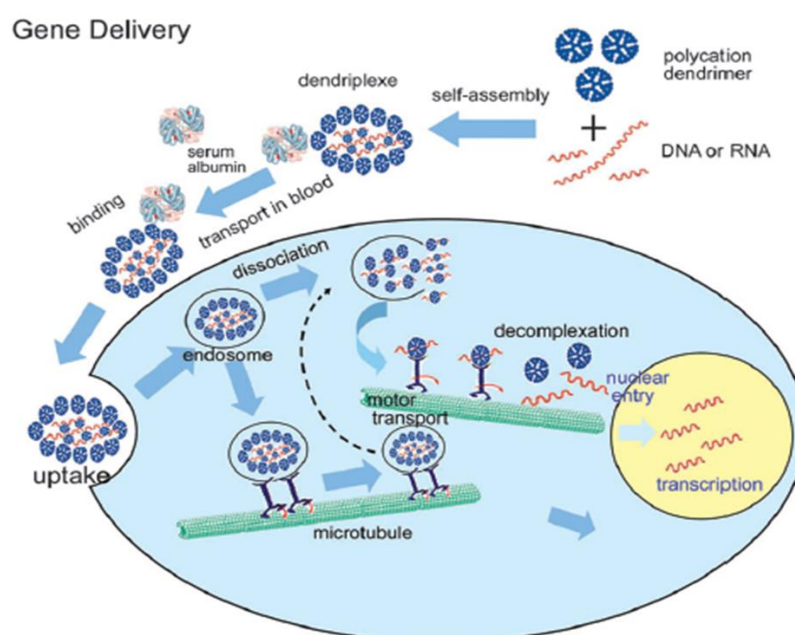


**Figure 1.3** The multi-step processes for nucleic acid delivery to cells. <sup>19</sup> (Reprint from reference: Tian, W. D. et al. *Chem Soc Rev* **2013**, *42*, 705).

### 1.3 DNA Condensation

In nature, DNA exists primarily in a highly condensed state. DNA packaging in the cell is typically protein mediated using, for example, histones (in eukaryotic nuclei) or protamines (in sperm cells). The scale of this compaction is immense. In human cells, nearly 2 meters of DNA is compacted within its roughly 10  $\mu\text{m}$  size. Packaged DNA is ubiquitous in nature and the laboratory with examples ranging from viruses, sperm cells, bacterial nucleoids and gene therapy constructs.<sup>15,20</sup> Generally in the presence of cations of charge greater than 3, DNA in vitro spontaneously condenses. Usually, DNA condensation is defined as the collapse of extended DNA chains into compact, orderly particles containing only one or a few molecules.<sup>20</sup> In aqueous solutions, DNA in vitro spontaneously condenses in the presence of counterions with charge 3+ or higher. The resulting polycationic DNA assemblies often form toroidal or rod-like particles typically with DNA helices arranged parallel to one another on a hexagonal lattice.<sup>21</sup>

Upon condensation, the resulting compacted DNA structures have well defined equilibrium surface separations. These surface separations between DNA helices typically range from 5–15  $\text{\AA}$  of water between hexagonally packaged DNA. This surface separation represents a balance of cation-mediated attractive and repulsive forces. Despite significant work in recent years, the phenomena of DNA condensation remains poorly understood. There remains a need for direct knowledge of the underlying thermodynamic forces driving DNA condensation. The failure of classical Poisson–Boltzmann (PB) mean-field theory, assuming simple electrostatic attraction between cation and DNA, to fully explain the observed attractions observed in DNA condensation has inspired the development of several new theories including correlated counterions, screened Debye–Hückel interactions between helical molecules and water-structuring forces.<sup>22–25</sup> To account for the attractions driving DNA condensation, these theories require correlations of charges or water structuring. The recently proposed electrostatic zipper model provides a convenient model for discussing correlations and attractions (Figure 1.4). They propose binding of cationic

charges in the major or the minor grooves of DNA, thus leading to attractive interhelical correlations between apposing helices. The continued development of these and other theories has highlighted the need for more experimental measurements that can help limit and distinguish between theories.

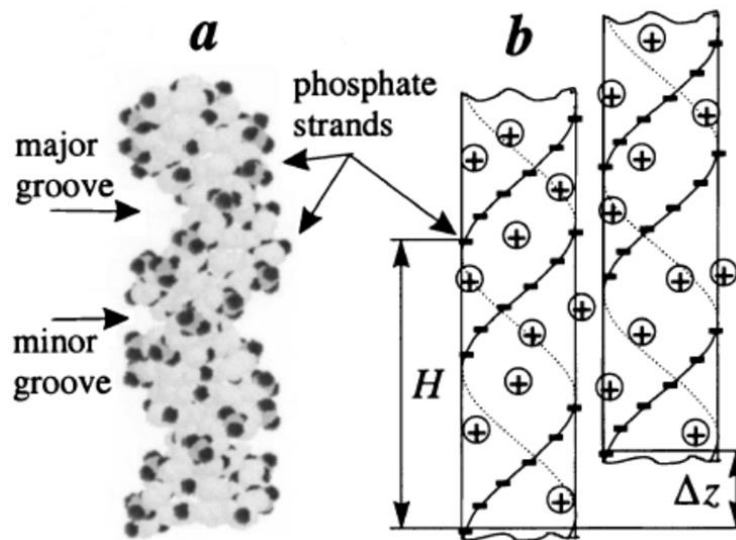


**Figure 1.4** The electrostatic zipper model used to explain DNA condensation by linear polycations. This model suggests that the polycations work like a “zipper” to fasten DNA together by binding into DNA grooves. (Reprint from reference: Kornyshev, A. A. et al. *Physical Review Letters* **1999**, 82, page 4138.)

Another model proposed to explain DNA condensation involves the structuring of water molecules.<sup>22,25</sup> Since the double helices come very closely to each other in the condensed phase, this leads to the restructuring of water molecules along the DNA giving rise to the so-called hydration forces. Each water molecule represents a dipole, which would predominantly orient in the solution perpendicular to the charged surface. This water structuring can occur between helices so as to be attractive or repulsive (Figure 1.5). Despite different physical origins, both the electrostatic zipper and hydration models predict similar decay lengths and a constant ratio with the long-range attractive force being two times the short range repulsive force. At equilibrium, the observed DNA-DNA spacing represents a balance between

the attractive and repulsive forces within the DNA condensate.

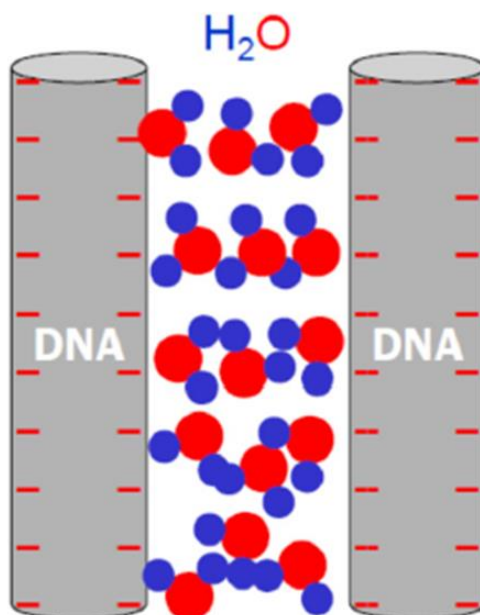


**Figure 1.5** The hydration model used to explain DNA condensation. To get DNA molecules closer, the water needs to be rearranged which produces a stronger force than van der Waals force. (Reprint from reference: Li, J. Q. et al. *Nanomaterials-Basel* **2015**, 5, Page 250.)

#### 1.4 Structure of PAMAM-DNA Complexes

Hyperbranched polycations, such as polycationic dendrimers, presumably would not be able to bind to DNA and correlate their charges with the phosphates of adjoining DNA in the same manner as linear cations. Other binding modes, such as bridging interactions between DNA double helices, may be necessary to induce condensation with dendrimers. While no studies on the intermolecular forces of PAMAM-DNA have been previously reported, there have been some SAXS studies to investigate internal structures primarily in complexes of DNA condensed by high generation PAMAM and PPI dendrimer.<sup>15,26,27</sup> Depending on the dendrimer chemistry and generation, tetragonal and hexagonally packaged columnar mesophases, as well as DNA wrapping, have been reported in dendrimer-DNA complexes mostly determine by solution small angle X-ray scattering (SAXS) experiments. In contrast, TEM studies primarily observe toroidal or rod-like particles similar to linear

cation-DNA complexes where DNA was observed to be hexagonally packaged.

In our early studies, we focused on low generation PAMAM-DNA (Chapters 4 and 5) but in Chapter 6 will discuss G4-PAMAM: DNA complexes. Some structural studies of G4-PAMAM were previously reported examining internal structure under a variety of different condensing conditions (Figure 1.6).<sup>28-30</sup> They report that the internal structure of G4 PAMAM dendriplexes is primarily affected by three factors: (i) degree of protonation of amine groups in PAMAM molecules (dp), (ii) the ratio between protonated amine groups in PAMAM dendrimer and phosphate groups in DNA (N/P charge ratio), and (iii) DNA concentration. They report square columnar phase, hexagonally-packed DNA superhelices, as well as beads on string structures thought to be similar to DNA wrapping around histones are all observed depending on the condensing conditions. Yang et al. propose that BOS structure are formed due to a balance of the entropy gain upon counterions release into solution by the energy required to bend DNA.<sup>28</sup> The complex structure condensed by PAMAM also shows time dependence. Elsayed et al. visualized the structure changes of G4-PAMAM condensed siRNA at 20min and 24hour by AFM. They argue this is because the condensation process is biphasic: a rapid exothermic binding followed by a slow endothermic formation of highly packaged structure.<sup>18</sup> siRNA, while quite short, is also double stranded like dsDNA and it was proposed this two-step process may occur in PAMAM: DNA as well. The formation of kinetic, non-equilibrium states may also explain the variety of observed interior structures in dendriplexes.

Chapter 6 will focus on a hypothesis to incorporate zwitterionic moieties into PAMAM molecules to form zPAMAM as a potential improved transfection agent as described further in the introduction to the chapter. Transfection efficacy and cellular toxicity has not been evaluated yet. The focus of chapter 6 is to examine the effect of zPAMAM on the resulting structure and phase behavior in dendriplexes and compare it to the unmodified G4 PAMAM-DNA assemblies. In Chapter 7, we will provide a summary for the entire dissertation as well as suggest future perspectives.

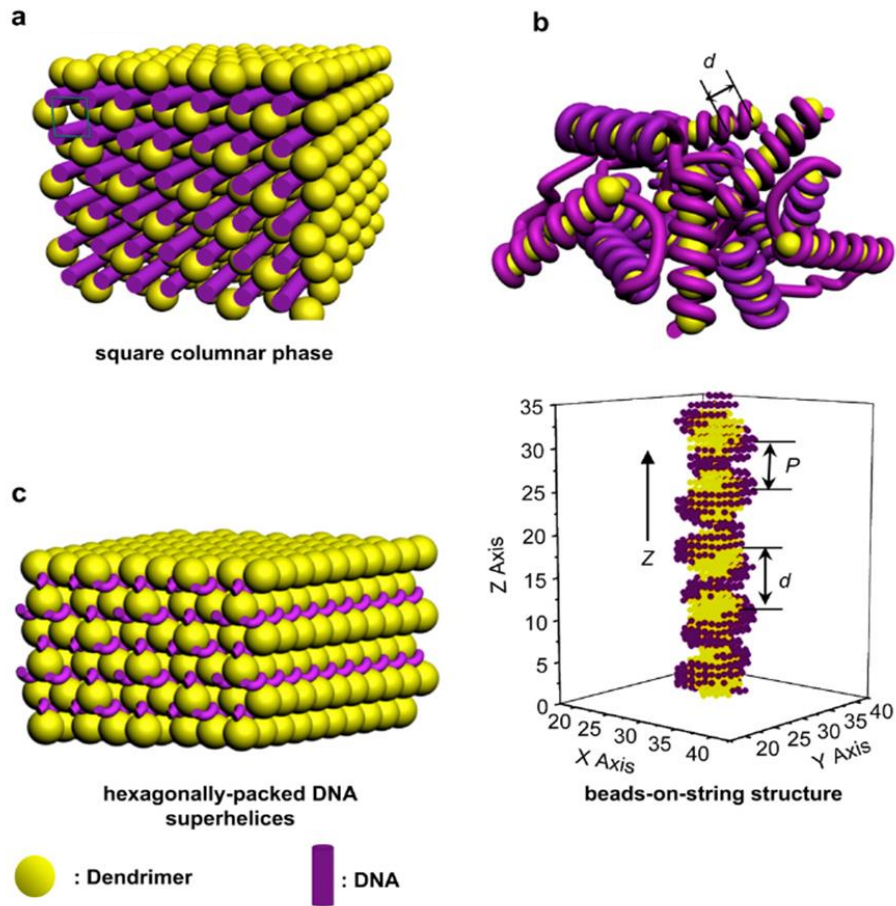


**Figure 1.6** Proposed structures of Dendrimer:DNA complexes including (a) square columnar package, (b) beads-on-string structure, and (c) hexagonally packaged structure. (Reprint from reference: Yang, C.-C. et al. *Macromolecules* **2014**, *47*, Page:3125.)

## Chapter 2 Small Angle X-ray Scattering (SAXS)

Small-angle X-ray scattering (SAXS), either on its own measurement or coupled with measurement of osmotic pressure, is the primary analytical tool used throughout this work. This chapter provides a brief overview of SAXS.

### 2.1 Introduction

SAXS is a variant of conventional X-ray scattering in which measurements are restricted to small diffraction angles, close to the incident X-ray beam. The scattered intensity at small angles provides information on the size, shape and internal structure of particles. SAXS is a widely used method for the study of macromolecules as it provides information covering lengths scales from approximately 5-200 nanometers.<sup>31-35</sup> A major advantage of SAXS, compared to other structural methods, is its versatility with respect to the sample preparation. SAXS can be used to measure a wide range of samples including solids, dry powders, liquid crystals, colloidal solutions, and aqueous solutions.<sup>32,34,36</sup> The ability to measure scattering from solutions is particularly important since many macromolecules, especially in biology, are not capable of being crystallized. Another advantage is that scattering methods yield structural information that averages over all the material the X-ray beam passes through, and is therefore consistent with the bulk properties of a sample. This is in contrast to direct imaging methods, such as transmission electron microscopy (TEM), which can give structural information but is limited to localized regions within a sample. Chapter 3 will discuss in more detail the method of osmotic pressure and the measurement of intermolecular forces within the condensed DNA phase through coupling of SAXS and osmotic pressure.<sup>25,37</sup>

### 2.2 Production of X-rays

X-rays are a form of short-wavelength (typically 0.1 Å to 100 Å) electromagnetic radiation. Monochromatic X-rays ( $\Delta\lambda/\lambda \approx 10^{-3} \sim 10^{-4}$ ) with wavelengths in the approximate range of 0.5–2.5 Å are especially useful to probe the structure of

materials because these wavelengths are comparable to the interatomic distances in chemical bonds ( $\sim 1 \text{ \AA}$ ).<sup>38</sup> Throughout this work we have used the most energetic characteristic X-rays from a copper target anode, the  $K\alpha$  emission, which results in a wavelength of  $1.54 \text{ \AA}$ .<sup>38</sup>

For a laboratory X-ray source, X-rays are produced when electrons of sufficient energy impinge on a suitable target material. In brief, an electrical current is passed through a metal filament (the cathode). This current heats the filament wire, exciting electrons out of the filament. These electrons are then accelerated by an applied field (typically 45-60 kV) and used to bombard a metal target anode. The choice of metal for the target anode determines the X-ray energies. Upon impacting the target, the electrons rapidly decelerate, which produces a broad-spectrum emission named 'bremstrahlung' or 'braking radiation'. In addition to this bremstrahlung, some accelerated electrons will eject electrons from the core of atoms in the target anode. Relaxation of higher-energy electrons into these vacancies results in the release of a photon with a characteristic wavelength determined by the energy level difference. In our set-up, the filament is operated with 20 mA current and 45 kV potential difference between cathode and anode. Since X-rays are a form of light, they display a wave-particle duality.<sup>39</sup> Certain properties of X-rays are best understood by considering them as a stream of photons. For example, flux describes the strength of the emitted radiation and is defined as the number of photons passing through a unit area per second.<sup>39</sup>

### **2.3 X-ray Scattering**

When dealing with X-rays, there are two terminologies that need to be distinguished: diffraction and scattering. Diffraction of X-rays results from a combination of two phenomena: (1) the scattering of radiation by individual electrons and (2) interference between the scattered waves from the primary radiation.<sup>39</sup> Scattering is primarily concerned with the first phenomena.<sup>39</sup> However, in experiments, these two terminologies are sometimes taken to have the same meaning.

In this work 'diffraction' is used to describe scattering from crystals, while 'scattering' is used to describe experiments on materials that are not true crystals. On occasion the term 'wide-angle scattering', or 'WAXS' is used to mean diffraction, especially from crystalline materials.<sup>39</sup>

The fundamental phenomena underlying all types of small-angle scattering experiments are the elastic scattering of electromagnetic radiation by electrons and the subsequent interference of the scattered photons. Upon interaction with the sample, a small portion of the photons are scattered elastically by electrons in the sample and these scattered photons then interfere with each other following classic electromagnetic phenomena. In SAXS, the structure of a material is probed when a beam of monochromatic X-rays are directed on a (semi)crystalline material and the scattered X-rays are observed at small angles (within a few degrees) with respect to the primary beam.<sup>38</sup> Since X-rays are electromagnetic radiation, they will interact with electrons in the sample. From the Thomson formula, the scattered beam flux is inversely proportional to the magnitude of the square of the electron mass ( $I \propto \frac{1}{m_e^2}$ ).<sup>39</sup> The electron density distribution is dependent on the type and arrangement of atoms. In single-crystal X-ray diffraction, by measuring the distribution and flux of these scattered beams, the electron density within the samples can be reconstructed in a three-dimensional electron density map. Thus, in a single crystal analysis it is possible to determine the mean position of the atoms and therefore identify chemical bonds. In this manner, X-ray scattering is used to determine the structure of crystalline materials. For non-crystalline or semi-crystalline materials, the structural information is somewhat less definitive and precise, but important structural information can still be obtained.

Conventional crystals are regular, repeating three-dimensional stacks of a well-defined chemical motif. The unit cell may be defined in more than one way, so the particular unit cell used for any given crystal is governed by a set of conventional rules. The important point is that the electron density within the crystal is periodic in

three dimensions, and thus forms a specific, well-organized pattern that is unique to that particular crystal. As a result of the periodicity, crystals can be described by sets of crystallographic planes of electron density. Under certain geometric conditions, X-rays scattered by parallel crystallographic planes, as shown in Figure 2.1, will constructively interfere, so that the scatter X-rays form a diffracted beam. When the X-ray plane wave interacts with an electron (O) in the crystal, the incoming wave AO will be diffracted to the OB direction. The same thing will happen for electron O'. The X-ray beams travel different lengths, with the wave passing through O' being longer than that through O. In other words, A'O' + O'B' is longer than AO + BO. The difference of the length is  $2d_{hkl} \sin \theta$ . The interference is constructive only when the scattered X-rays obey Bragg's law:  $n\lambda = 2d \sin \theta$ . In this manner, the spacing  $d$  between parallel crystallographic planes can be determined from the diffraction pattern of a crystal, where  $2\theta$  is the scattering angle,  $n$  is an integer and  $\lambda$  is the wavelength of the incoming X-ray radiation.<sup>40</sup> The lattice spacing,  $d$ , is inversely proportional to  $\sin \theta$ , meaning that the larger the repeat distance, the smaller the angle

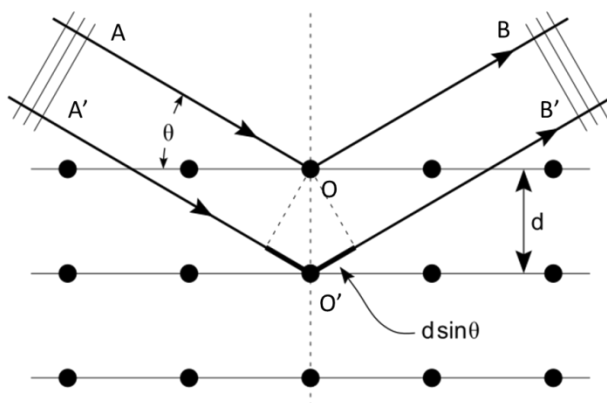


**Figure 2.1** Scattering of X-rays by well-organized structures. The incoming X-ray beam (from the upper left) will be scattered by electrons and reradiate a small portion of its flux following Bragg's law. (Reprinted from [https://en.wikipedia.org/wiki/X-ray\\_crystallography](https://en.wikipedia.org/wiki/X-ray_crystallography).)

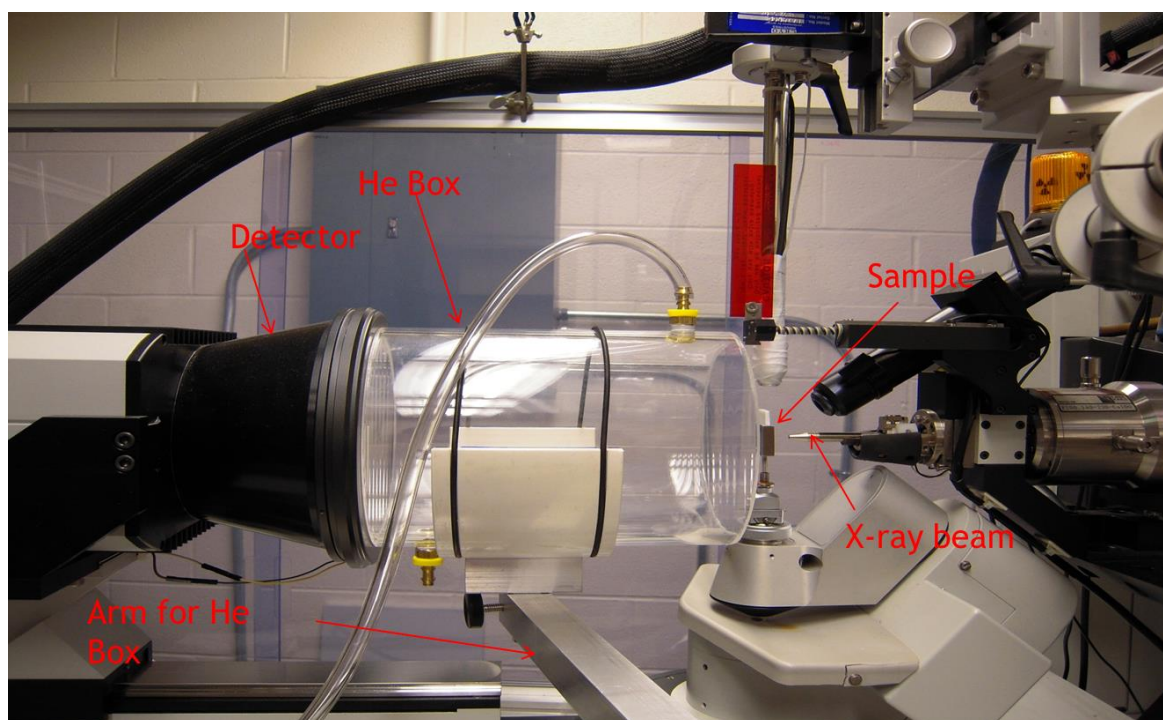
at which scattering is observed. In single crystals, the directions observed for diffraction events can be used to accurately determine the lattice parameters of the unit cell. The unit cell of a crystal in real space consists of three repeat vectors (a,b,c) and the three angles ( $\alpha,\beta,\chi$ ) between them.<sup>39,40</sup> In diffraction, or reciprocal space, this indexing of the unit cell allows us to define a series of crystallographic planes denoted as (h k l). Measurement of the Bragg peak positions thus allows the determination of the shape and size of the unit cell of the crystal. In powder diffraction, the regular, repeating nature of a single crystal is rotationally scrambled, such that discrete diffraction maxima are uniformly spread out into 'cones' of diffraction at well-defined  $2\theta$  angle. Diffraction from semi-crystalline materials also leads to rotational smearing of the diffraction events, to an extent that depends upon the degree of crystallinity. Additional broadening of diffraction in  $2\theta$  occurs as the size of crystalline (or semi-crystalline) domains within a sample decreases.

SAXS is typically used to study structure of size on the order of 1-200 nm. Using Bragg's law, we can calculate that for lattice spacings (d) of a few angstroms and  $\lambda = 1 \text{ \AA}$ , the scattering angle  $2\theta$  is typically about  $20^\circ$ . For  $d = 100 \text{ \AA}$  and the same wavelength, we would calculate the scattering angle to be about  $0.6^\circ$ . Therefore, in SAXS typically scattering angles of  $2\theta$  less than  $2^\circ$  are used. SAXS can be adopted to four models: a dilute particulate system, a non-particulate two-phase system, a periodic system, and a soluble blend system.<sup>41</sup> For our system of cation condensed DNA, the system contains periodic structural features and is thus suitable for analysis by SAXS. However, these structural motifs are rotationally scrambled and tend to exhibit a range of domain sizes. Thus diffraction features from the DNA assemblies in this work typically take the form of diffuse rings with radius that is characteristic of the particular sample.

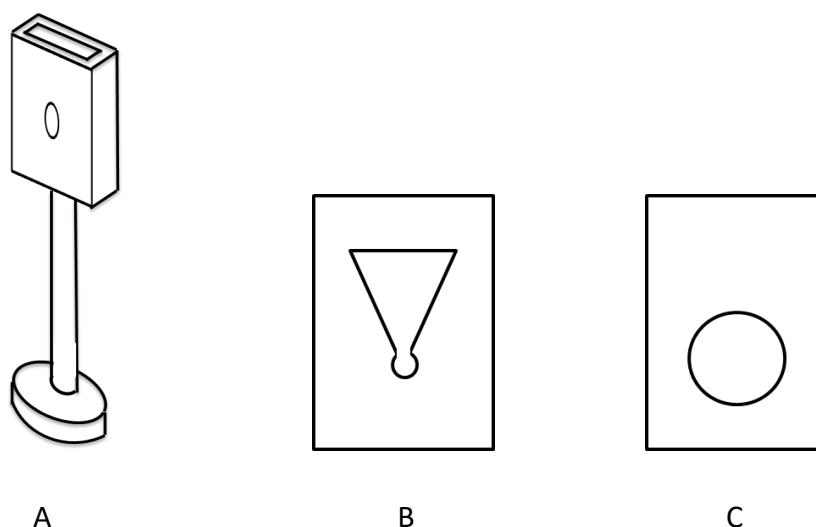
## 2.4 Experimental Setup

Figure 2.2 shows the in-house setup used for sample examination. The X-ray source consists of graded-multilayer focused  $\text{CuK}\alpha$  radiation ( $1.54 \text{ \AA}$ ) from a Nonius

FR-591 rotating-anode fine-focus X-ray generator operated at 45 kV and 20 mA. The primary purpose of this machine is conventional small-molecule crystallography, so a number of changes were required for SAXS work. The condensed DNA samples are not 'crystals' in the normal sense of the word, and thus cannot be handled using normal (i.e., crystal sample) mounting techniques. For DNA assemblies, a special sample holder was designed, as shown in Figure 2.3. Samples are sealed in a cell with a bath of buffer solution to maintain equilibrium. The cell inner components are made of Teflon. Samples are placed in the center of the circle in Figure 2.3B, then the sample is sealed with Mylar films on both sides. Using one chip C on each side, a sandwich is made that can be directly inserted into the stainless steel sample holder, as shown in Figure 2.3A. This device holds the sample in the path of the X-ray beam. To eliminate scattering of X-rays by air, a cylindrical box filled with helium gas with front/back mylar windows is placed in the flight path from the sample to the detector. This box is held on a swinging arm to allow rapid and precise movement of the helium box into the correct position. A metal (lead) beam stop is placed in the center of the rear mylar window of the box to prevent incident X-ray radiation from directly



**Figure 2.2** Experimental in-house setup for SAXS at the University of Kentucky.



**Figure 2.3** Components of the sample mount used for SAXS. (A) the stainless steel sample holder. (B) and (C) show the teflon chips used to hold the samples like a sandwich. The sample is placed in the center of the circle in chip B with excess bath solution to ensure that the sample remains at equilibrium. Each side of chip B is then sealed by Mylar membranes, which are then sandwiched tightly between two of the C chips. This prevents the bath solution from leaking when placed within the sample holder, A.

hitting the detector. Diffraction patterns are recorded by a Bruker SMART-6000 CCD detector, which has a phosphor optimized for  $\text{CuK}\alpha$  radiation. Diffraction patterns are analyzed using the software packages Fit2D (reference) and Origin (reference) to extract parameters of structural importance. In most cases, DNA assemblies give scattering similar to a diffuse powder diffraction pattern, i.e., broad rings. The radius of these rings, or rather their  $2\theta$  Bragg angle, allows us to determine the Bragg d-spacings relevant for the condensed DNA samples. The interhelical spacings of the condensed DNA can then be calculated using simple geometrical relationships.

## 2.5 SAXS Calibration

To accurately and reproducibly determine the periodic spacings of the material of interest, it is vital to accurately determine the sample to detector distance for the SAXS instrument.<sup>41</sup> For small-angle measurements, a suitable standard material for calibration must fulfill certain criteria. Such a standard must have a well-defined diffraction peak below the  $2\theta$  values of interest in the DNA samples. It must be stable under ambient conditions and when exposed to X-rays, safe to handle, and straightforward to prepare.<sup>42</sup> In this work, silver behenate (AgBeh,  $\text{CH}_3(\text{CH}_2)_{20}\text{COO}\cdot\text{Ag}$ ) powder was used as a standard. AgBeh is a silver salt with a 22 carbon carboxylic acid, which forms regular plate-like crystals with the lattice spacing 58.38 Å. Previously it was shown by multiple independent users that AgBeh powder has a set of well-defined (0 0  $l$ ) diffraction peaks at  $2\theta$  angles down to  $1.5^\circ$  when using  $\text{CuK}\alpha$  radiation.<sup>42,43</sup> A typical X-ray diffraction pattern for AgBeh is shown in Figure 2.4. We can clearly see a set of scattering peaks corresponding to (0 0  $l$ ) reflections. Within AgBeh powder, the plate-like crystallites are randomly oriented in all directions, resulting in the observed circular scattering patterns.

Using the software Fit2D, we can find the center of these concentric circles, and thus locate the incident beam position. Radial integration of the scattered intensity from the center of these concentric circles allows for the 1D plotting of the scattering intensity curve shown in Figure 2.5. The presence of relatively sharp scattering peaks indicates the presence of a crystalline material. If the scattering is from a perfect crystal, the peak should be infinitely sharp. Bragg peak widths and overall profiles are determined by finite-size effects, defects and other distortions within the lattice.<sup>39</sup> The peaks are well described by a Gaussian distribution and fits to the peaks are used to determine the center position of the Bragg peaks.

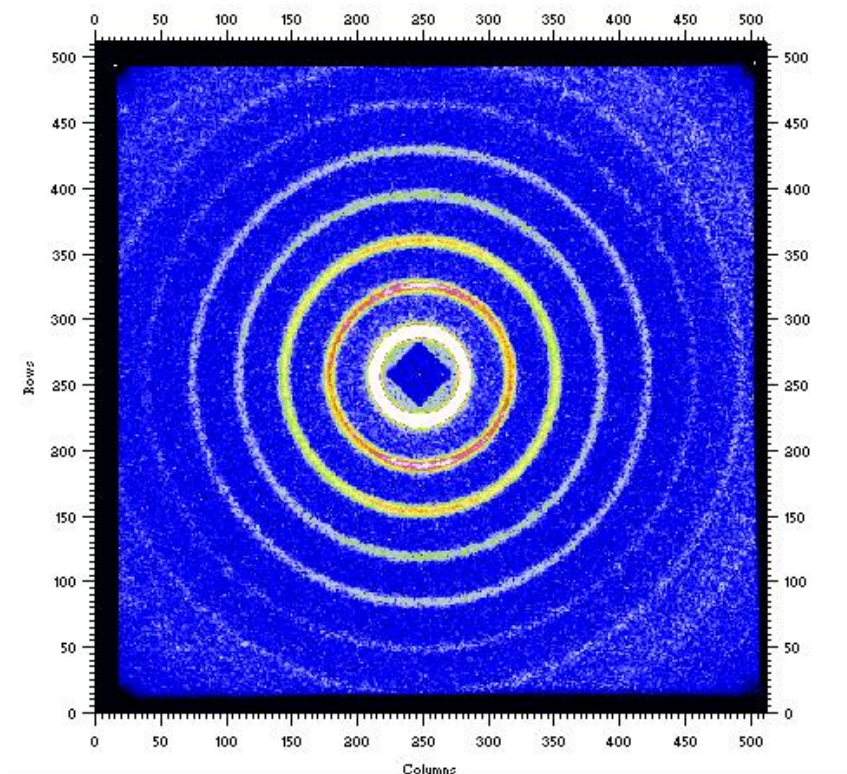


**Figure 2.4** SAXS diffraction pattern of AgBeh standard shown by Fit2D.

As shown in Figure 2.5, seven Bragg peaks are observed given the sample-to-detector distance used for the in-house SAXS setup. Each peak corresponds to one of the concentric rings in Figure 2.4. Integration results are analyzed using Origin plotting software to determine the center position of each Bragg peak, which corresponds to the periodic spacings of the AgBeh crystal. Since these spacings have been previously reported, we can use the peak positions to calculate the sample-to-detector distance for the instrument. Figure 2.6 shows the basic geometry of a typical scattering setup. As depicted, we can determine the sample to detector distance ( $L$ ) with simple geometry from the following relationship:  $\tan(2\theta) = R/L$ , where  $2\theta$  is the scattering angle,  $R$  is the distance measured on the detector of the Bragg reflection.  $2\theta$  can be directly calculated for AgBeh for each hkl reflection as shown in Table 2.1. To accurately determine  $L$ , we calculate  $L$  for each of the seven

Bragg peaks observed at the detector and take the average of the seven calculated values as our sample to detector distance. In this work,  $L=23.2\pm 0.005$  cm.

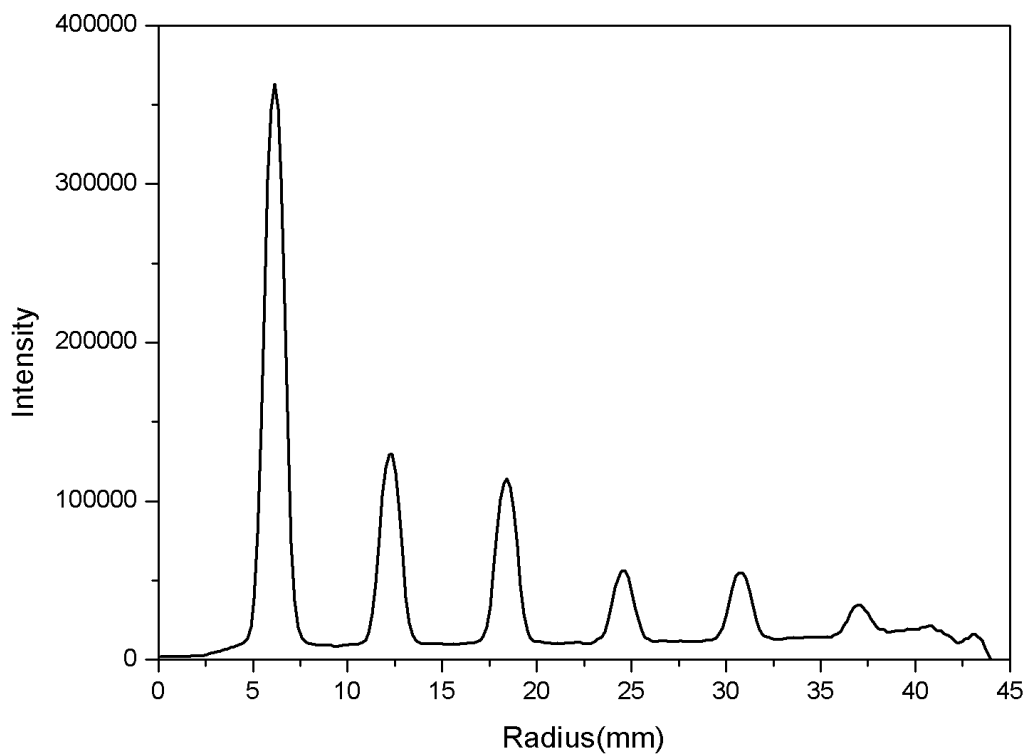


**Figure 2.5** Small-angle X-ray scattering profile of silver behenate. Seven Bragg reflections are observed for the sample-to-detector distance used for the in-house setup.

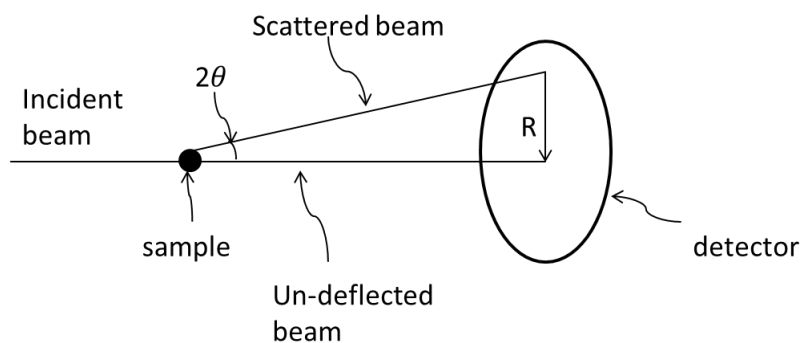


**Figure 2.6** Basic geometry of scattering involving the incident beam, the sample, the scattered beam, and the detector. The scattering angle is  $2\theta$ .

**Table 2.1** The scattering angles and the  $d$ -spacings of AgBeh obtained by  $\text{CuK}\alpha$  radiation analysis. (Reprint from reference Lee, B. et al. J. Appl. Cryst. 2006. 39, Page 750.)

<b>hkl</b>	<b><math>d(\text{\AA})</math></b>	<b><math>2\theta^\circ</math></b>
001	58.380	1.513
002	29.190	3.027
003	19.460	4.537
004	14.595	6.051
005	11.676	7.565
006	9.730	9.081
007	8.340	10.607
008	7.298	12.128
009	6.487	13.651

## 2.6 SAXS of Condensed DNA Samples

When DNA is condensed by linear polycations (typically of charge +3 and higher), it self-assembles into a well-organized structure. DNA packaging within this condensed state is typically hexagonal; consistent with the lowest free-energy state for the packing of rods.<sup>15,16</sup> Unoriented samples typically yield a uniform ring pattern on the 2D detector, which is radially averaged to give the typical plots of diffracted intensity vs. scattering vector  $Q = (4\pi/\lambda) \sin \theta$ , where  $2\theta$  is the scattering angle. Using Bragg's equation, we can calculate the corresponding Bragg spacing from the observed scattering vector. Using Fit2D, we can calculate the scattering intensity profiles for our DNA condensates. A typical scattering profile is shown in Figure 2.9 for a polycation-DNA complex. We then use Origin software, to determine the average peak position for the observed reflections. The scattering vector  $Q$  corresponds to the maximum of the scattering and is inversely proportional to  $d$ .  $D_{Br}$

is then simply calculated as  $D_{Br} = 2\pi/Q$ . For DNA in a hexagonal columnar structure, we can then calculate the average DNA-DNA spacing, or interhelical spacing, as simply  $D_{int} = (2D_{Br})/\sqrt{3}$ . Using simple geometry it can also be shown that if DNA is condensed in a square columnar structure, the corresponding interhelical spacing is  $D_{int} = \sqrt{2}D_{Br}$ .

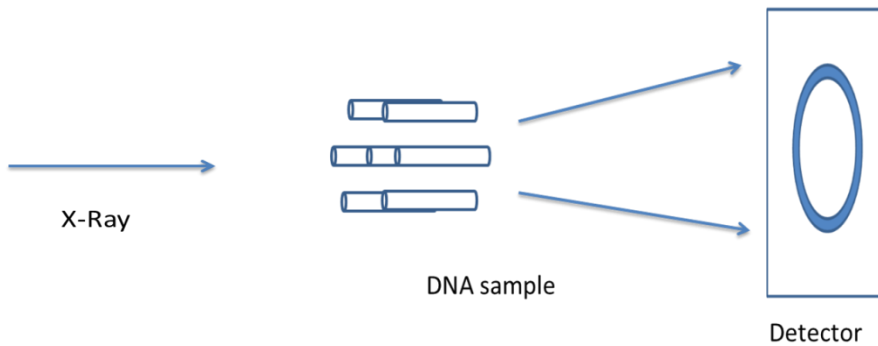


**Figure 2.7** Sketch of the condensed DNA and resulting diffraction pattern as measured by SAXS.

In our studies, we observe scattering consistent with hexagonal packaging in low generation PAMAM/DNA complexes, similar to linear cation-DNA complexes; as discussed further in Chapters 4 and 5. Other studies using high generation PAMAM (often G6 and up) to condense DNA have reported other lattice types, including square columnar and 'beads-on-string' type structures.<sup>17,18</sup> In Chapter 6, we use G4 PAMAM to condense DNA. For the types of samples encountered in this work, typically only one Bragg reflection is observed, which is insufficient for full lattice determination. Therefore, we will discuss only the Bragg spacing,  $D_{Br}$  for the samples, as this is independent of the lattice.

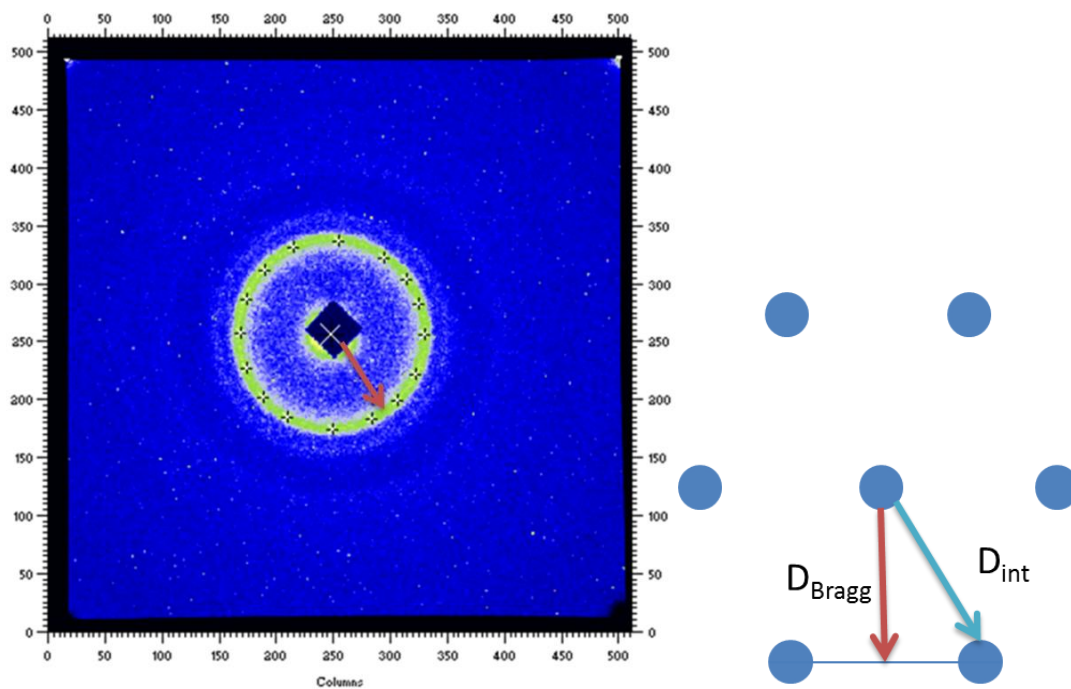


**Figure 2.8** (left) A typical 2-D SAXS pattern obtained from cation condensed DNA. The radius of the ring on the left gives the Bragg spacing ( $D_{Br}$ ), i.e., the spacing between packed layers of the condensed DNA. (right) Cartoon depiction of the hexagonal packaging of DNA rods shown end on showing the geometric relationship between  $D_{Br}$  and the interhelical DNA spacing  $D_{int}$ .

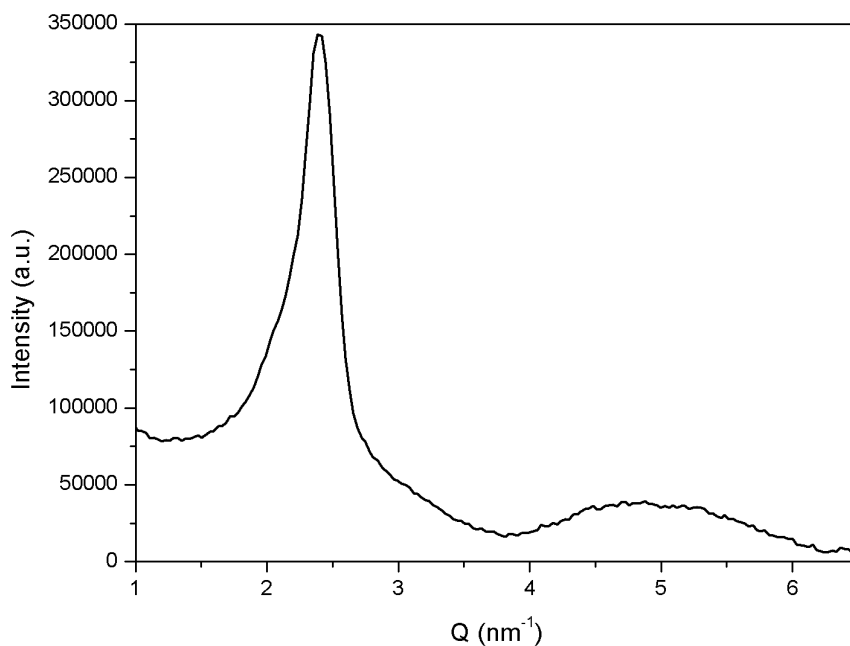


**Figure 2.9** Typical SAXS signal of DNA complexes. The intensity scattering is shown as discrete Bragg peaks.

## Chapter 3 Osmotic Pressure and Force Study

### 3.1 Theory of Osmotic Pressure

Osmosis is the flow of solvent through a semipermeable membrane from a pure or dilute solvent to a more concentrated solution until the concentrations across the membrane are equal. In biology, cell membranes of plants and animals tend to be permeable to water and other small molecules. Therefore osmotic flow plays an essential role in many physiological processes for living organisms.<sup>44-46</sup> Osmosis can be illustrated as shown in Figure 3.1. Here we have two solutions containing different concentrations of solutes separated by a semi-permeable membrane. The large solute molecules are not able to pass through the membrane but water and small molecules can redistribute themselves across the membrane. This process will continue until the chemical potentials of the two phases are equal. Since the system is open, the solutions can change in volume by changing vertical height.

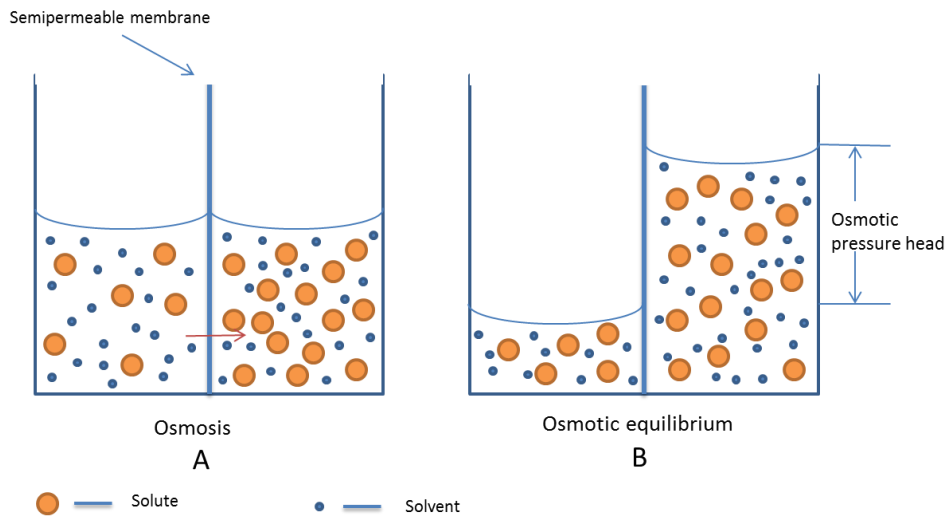


**Figure 3.1** Illustration of osmosis. (A) two solutions of different solute concentrations are separated by a semipermeable membrane. The semipermeable membrane allows solvent and small molecules to pass through it but prevents passage of the large solute molecules. (B) at equilibrium, the fluid level rises until the back pressure equals the osmotic pressure which occurs when the concentration of solutions on both sides are the same.

Due to osmosis, the height of the lower concentration side decreases while the height of the higher concentration side increases.<sup>47</sup> The chemical potential changes with the concentration changes for both solutions. Equilibrium will occur when chemical potentials are the same on both sides of the semipermeable membrane. When an external pressure applied to the solution in order to stop the osmosis of solvent across the semipermeable membrane into the concentrated solution, this external pressure may be defined as the osmotic pressure.

Jacobus van't Hoff analyzed the phenomenon of osmotic pressure and first proposed a law showing the relationship between osmotic pressure and the concentration in solution. He deduced the mathematical expression for osmotic pressure from pure water and salt solution under the condition of osmotic equilibrium, i.e. when the chemical potential of solvent on both sides of the membrane is equal. The mathematic equation for osmotic pressure is:

$$\Pi = MRT \quad (3.1)$$

where  $\Pi$  is osmotic pressure,  $M$  is molarity,  $R$  is gas constant and  $T$  is temperature with unit  $K$ . Later a simple extension has did to this equation and made it more accurate for all kinds of solutions,

$$\Pi = iMRT \quad (3.2)$$

where  $i$  is a dimensionless factor, van't Hoff factor, which represents how many kinds of particles dissociated when the solute dissolved in solvent.<sup>47,48</sup> From the extended van's Hoff law, we can clearly see that the osmotic pressure is only related to the number of solute particles in solution, regardless of the particle size, density, configuration or electrical charge. Osmotic pressure is therefore one of the very few physical properties of a solution that is a colligative property dependent only on the number of particles in solution.<sup>47,48</sup>

## **3.2 Vapor Pressure Osmometer**

One of the most difficult and tedious aspect of using osmotic pressure, or osmotic stress, is getting accurate osmotic pressures of the stressing polymer solutions. Here, we discuss the use of a Wescor Vapor Pressure Osmometer (Model 5600) for the determination of osmolality in our stressing polymer solutions. Osmolality is a measure of the moles (or osmoles) of solute per kilogram of solvent and is typically expressed as mol/kg or m. Since the amount of solvent will remain constant regardless of changes in temperature and pressure, osmolality is easier to evaluate and typically preferred is commercial osmometers to measurements of osmolarity or osmoles of solute per liter of solution.

### **3.2.1 Theory of Operation**

An osmometer is a device for measuring the osmotic strength of a solution, colloid, or compound. Traditionally, the direct way to measure osmotic pressure was a membrane osmometer using a semipermeable membrane as described previously to measure the pressure difference across the membrane. Membrane osmometry however is limited by the lack of a perfect semi-permeable membrane and typically requires larger volumes of sample and can be time consuming and difficult to operate. This has led to a need for means to accurately measure osmotic pressure indirectly.

Two other commercially available osmometers leverage the measurement of another colligative property to indirectly determine the osmotic strength of the solution of interest. In particular, they are freezing point osmometers and vapor pressure osmometers which determine the osmotic strength of solution by determining the freezing point depression or reduction in vapor pressure, respectively. In a single solvent solution, these colligative properties are directly related to the total number of solute particles in solution.<sup>49</sup> Osmolality is determined by comparing the basic colligative properties of the solution of interest to the basic colligative property of pure solvent. Freezing point osmometry (FPO) is rapid and inexpensive and requires

only small sample sizes (nL to L range) but is limited to samples of low viscosity. Vapor pressure osmometry also is less accurate than FPO but is rapid and inexpensive and can be used on a broader range of viscosities. Our VPO uses a new technology based on the measurement of vapor pressure depression by hygrometry using a thermocouple. The vapor pressure depression method enjoys a significant advantage over the measurement of freezing point depression or boiling point elevation is that it can be performed without the need to change the physical state of the specimen.<sup>49</sup>

Typically in our experiments, 10  $\mu\text{l}$  of the solution to be examined is pipetted onto a small, solute-free paper disc. This paper disc is then inserted into a sample chamber on the VPO and sealed. A thermocouple hygrometer is incorporated within the chamber. This thermocouple is a sensitive temperature sensor that operates on the basis of a thermal energy balancing principle to measure the dew point temperature depression within the chamber. The dew point temperature depression is itself a colligative property of the solution of interest and directly related to the solution vapor pressure.

### **3.2.2 Operation Procedure to Measure Osmotic Pressure**

To better understand the vapor osmometers measurements, we will focus here on explaining each step of the operation of the instrument. There are four individual steps occurring inside the osmometers chamber for any measurement. In the first step, the sample is introduced into the chamber and the chamber is closed. The sensing element in the instrument is a fine wire thermocouple hygrometer. The sensor is suspended in a metal mount which forms a closed chamber with the sample holder enclosing the specimen. Upon loading, there will generally be some temperature difference between the sample and the sample chamber. Temperature equilibrium occurs within a few seconds. For many samples, this time may be sufficient for the vapor pressure to also reach equilibrium. At vapor pressure equilibration, the rate for water change into the vapor is the same as the rate for the reverse process. After equilibration, step two is cooling. During cooling, an electric current is passed through the thermocouple

reducing the temperature by means of the Peltier effect to a temperature below the dew point. At this point, water condenses from the air in the chamber to form microscopic droplets upon the thermocouple surface. In step three, we see dew point convergence. Thermal energy is pumped from the thermocouple via Peltier cooling electronically to cancel out the heat influx to the thermocouple by conduction, convection and radiation. In this way, the temperature of the thermocouple is controlled exclusively by the water condensing upon its surface. The temperature of the thermocouple that was depressed below the dew point in step 2 now rises asymptotically toward the dew point as water continues to condense. When the temperature of the thermocouple reaches the dew point, condensation ceases and the thermocouple temperature stabilizes. The temperature difference between ambient and the measured dew point is the dew point depression, which is directly related to the solution vapor pressure. Dew point depression is measured with a resolution of  $0.00031^{\circ}\text{C}$ .<sup>49</sup> In the fourth and final step, the final results are read and displayed on the screen. Results are given in the SI units of osmolality – mmol/kg. After measurement, it is critical to thoroughly clean the sample holder of all sample material using lint-free tissue and a cotton-tipped applicator before moving to the next measurement. Contamination can make it impossible to calibrate the osmometer or produce accurate osmolality measurements.

### **3.2.3 Temperature versus Osmolality**

Figure 3.2 is a plot of thermocouple temperature as a function of time through the four step operating procedure described in 3.2.2. beginning with chamber closure (time = 0) and then proceeding through each of the four program steps described above.  $T_A$  is the ambient temperature in the chamber.  $T_D$  is the dew point temperature and  $\Delta T$  is the dew point temperature depression. The final output is proportional to  $\Delta T$ . Assuming the chamber remains closed after the osmometer displays the final reading, the thermocouple temperature will gradually return to  $T_A$  as all the water has evaporated from the thermocouple.<sup>3</sup> If the chamber is opened, the water will

evaporate almost immediately and the thermocouple temperature will quickly return to ambient temperature.

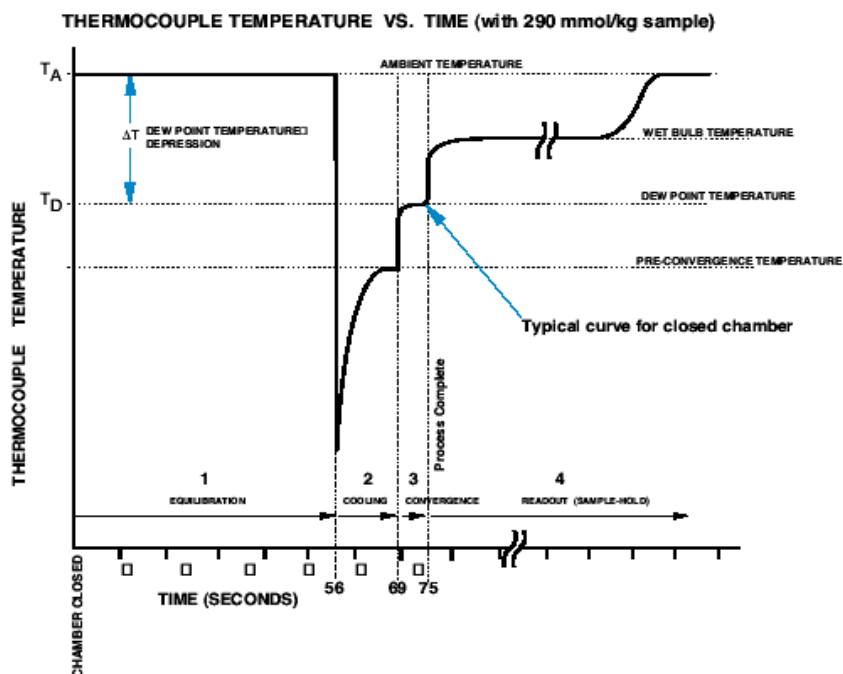


**Figure 3.2** Typical plot of thermocouple temperature versus time as the VPO instrument cycles through the four step program described in 3.2.2. (Reprint from Vapro Model 5600 Vapor Pressure Osmometer application manual)

The relationship between the reading obtained by the osmometer and the sample osmolality is directed by fundamental considerations. Vapor pressure depression is a colligative property of a solution and is known to be a linear function of osmolality. The relationship between vapor pressure depression and dew point temperature depression is given by:

$$\Delta T = \Delta e / S$$

where  $\Delta T$  is the dew point temperature depression in degrees Celsius,  $\Delta e$  is the difference between saturation and chamber vapor pressure and  $S$  is the slope of the vapor pressure temperature function at ambient temperature.<sup>49</sup> According to the

Clausius-Clapeyron equation, which characterizes, a discontinuous phase transition between two phases of matter of a single constituent, the slope  $S$  can be given as a function of temperature ( $T$ ), saturation vapor pressure ( $e_o$ ) and latent heat of vaporization ( $\lambda$ ) as

$$S = \frac{e_o \lambda}{RT^2}$$

where  $R$  is the universal gas constant. In our case, the latent heat of vaporization is the energy absorbed by water on the thermocouple during a constant-temperature process.<sup>49</sup>

The dew point temperature depression,  $\Delta T$ , is measured out by the voltage signal from the thermocouple. This voltage is equal to  $\Delta T$  multiplied by the thermocouple responsivity, which is approximately 62 microvolts per degree Celsius. After voltage amplification, the signal is processed to provide calibrate and compensate functions and display the final reading in  $mmol/kg$ .<sup>49</sup>

### 3.3 Unit Conversion

The unit displayed on our vapor pressure osmometers (VPO) is  $mmol/kg$ , while the unit we used for osmotic pressure ( $P$ ) in our study is  $erg/cm^3$ . It is convenient therefore to discuss briefly unit conversions for the osmotic studies.

The VPO gives the molality of the solution in mmol solute per kg solution. Stressing solutions used in this study to provide osmotic pressure are polyethylene glycol (PEG) dissolved in DI water or aqueous buffer. According to the van't Hoff law,  $\Pi = iMRT$ , thus we need to know the solution molarity. For PEG solutions,  $i$  equals to 1. The density of water or aqueous buffer is approximately 1 kg/L. Therefore if the molality of the PEG solution of interest is 1 mmol/kg; then the molarity is ~1 mmol/L. Assuming room temperature of 25 °C (298K), the osmotic pressure for 1 mmol/kg PEG solution is

$$\Pi = 1 \times (1 mmol/L) \times (8.314 J / (mol \cdot K)) \times (298 K) = 2.478 \text{ J/L}$$

Because joules ( $J$ ) is a unit for energy,  $1 J$  of work is equal to the work done by 1 Newton ( $N$ ) of force acting on an object for 1 meter ( $m$ ). So  $1 J = 1 N \times m$ . Thus,

$$\Pi = 2.478(N \times m)/L = 2.478(N \times m)/(10^{-3} m^3) = 2.478 \times 10^3 N/m^2$$

The pascal ( $Pa$ ) is the SI unit of pressure and is equivalent to one newton ( $1 N$ ) of force applied over an area of 1 meter squared ( $1 m^2$ ). So the osmotic pressure provided by  $1 mmol/kg$  PEG water solution is  $2.478 \times 10^3 Pa$ .

The *erg* is a unit of energy and work and represents the amount of work done by a force of one dyne ( $1 \text{ dyne} = 10^{-5} N$ ) exerted for a distance of one centimeter.  $1 \text{ erg}$  is equal to  $1 \text{ dyne cm}$  or approximately  $10^{-7} J$ . This can be used to approximate pressure as:

$$1 \text{ erg/cm}^3 = 10^{-7} J/cm^3 = 10^{-7} (N \times m)/(10^{-6} m^3) = 0.1 N/m^2 = 0.1 Pa$$

So, using these numbers we can calculate that a solution of  $1 mmol/kg$ , would provide an osmotic pressure  $\Pi \sim 2.478 \times 10^3 Pa$ , or  $2.478 \times 10^4 \text{ erg/cm}^3$ . Or converting to atmospheres,  $1 \text{ atm} = 1.013 \times 10^6 \text{ erg/cm}^3 = 1.013 \times 10^6 \text{ dyn/cm}^2$ . For our experiments, we will primarily use PEG with an average molecular weight of 8kDa as our stressing solution. Varying the PEG concentration (weight percent) from 0 to 50 wt%, we can vary the applied osmotic pressure from zero to nearly 100 atmospheres of osmotic pressure.

### **3.4 Using Osmotic Stress for the Direct Measurement of Intermolecular Forces in DNA Condensates**

It has been shown that small perturbations of water solvent several layers away from a macromolecular surface are what dominate the interaction of large bodies as they approach contact. The energies of these tiny perturbations are quite small, but the displacement of many water molecules can add up and ultimately dominate macromolecular interactions. Determining these intermolecular energies can be very

difficult as the energy of the perturbations is typically much smaller than the thermal energy of the water molecules.

To visualize these forces, we use osmotic stress coupled with SAXS. Osmotic stress allows for the gentle but strictly controlled removal of water from a macromolecular system. The basis of the method is to let the system of interest come to equilibrium against a stressing polymer solution of known osmotic pressure. Many rod-like structures, such as DNA, form ordered arrays during osmotic equilibration. This is shown in Figure 3.3. DNA, are equilibrated against a bathing polymer solution of known osmotic pressure. The bathing polymer, typically PEG, is too large to enter the condensed DNA phase, thus applying a direct osmotic pressure on the condensate. Water, salt, and other small solutes are free to exchange between the PEG and condensed DNA phases. After equilibration, the osmotic pressures in both phases are the same. Figure 3.3 right shows by increasing the polymer concentration in the stressing solution, we increase the osmotic pressure of the PEG subphase, resulting in a decrease in DNA-DNA spacings in the condensed phase at equilibrium. By measuring the change in the DNA-DNA spacings as a function of the applied osmotic pressure, we can create the osmotic equivalent of a pressure-volume (P-V) curve.<sup>50</sup> At its center is the equivalence of the mechanical work (osmotic pressure) needed to bring macromolecules like DNA closer in spite of the interactions between them and the chemical work (removal of water) needed to concentrate the macromolecular subphase. This osmotic stress method allows therefore for the direct determination not only of the molecular separations but the chemical potentials and ultimately intermolecular forces within the condensed DNA system through thermodynamic expressions based on the Gibbs-Duhem equation.

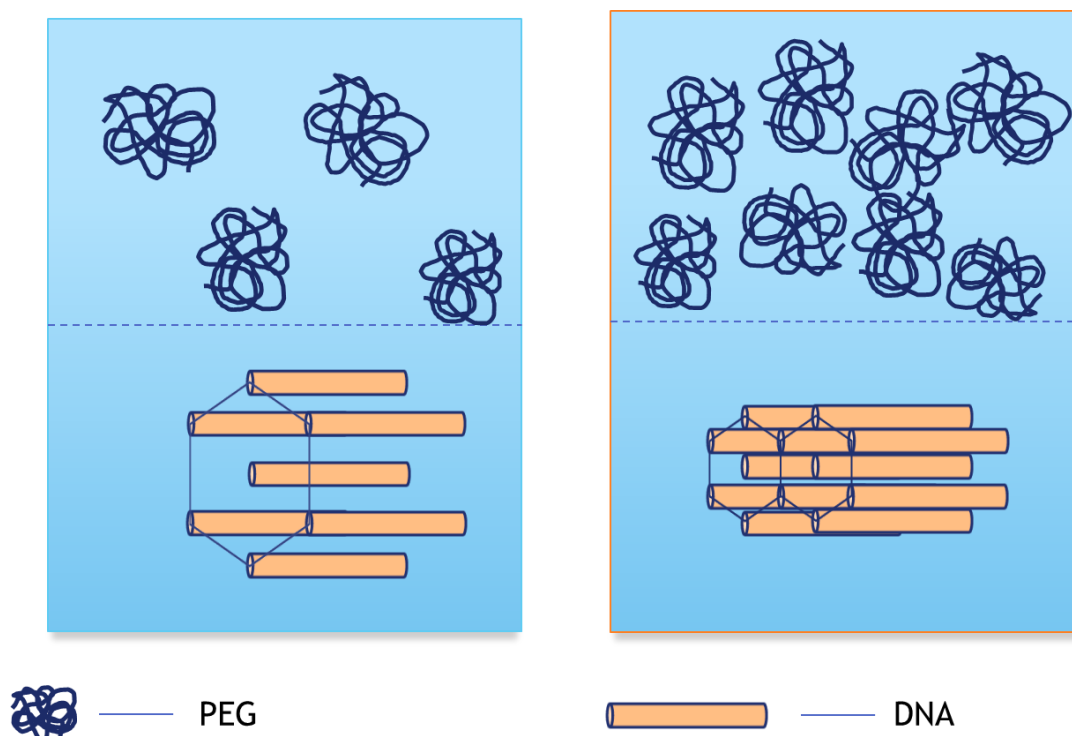


**Figure 3.3** Illustration of DNA arrays under osmotic stress. (left) PEG solutions provide osmotic pressure for the whole system. Rod-like systems, such as DNA, will form ordered arrays during osmotic equilibration. Due to the large molecular size, PEG 8kDa is excluded from the DNA phase even in the absence of a semi-permeable membrane. (right) Increasing the PEG concentration, increases the applied osmotic pressure, resulting in a decrease in DNA-DNA spacings in the condensed phase.

Figure 3.4 shows idealized osmotic stress force curves for non-condensed DNA (black) and condensed (right) DNA systems. With DNA in solution, we see no DNA-DNA spacings. At sufficient osmotic pressure, however, the DNA rods will order in an array characterized by a pressure dependent DNA-DNA spacing that scales exponentially (black line). In previous studies of polycation condensed DNA phases, DeRouchey has explored relationships between cation chemistry, packing densities, and compaction energies. Exposed to cations of charge  $> +3$ , DNA typically condenses spontaneously to form a hexagonal array with each molecule separated from its neighbors by 5-15 Å of water (red line, Figure 3.4). This spacing represents a balance of attractive and repulsive forces in the condensate. At high applied pressure, the forces are dominated by the short-range repulsive force only. We have shown that

using osmotic stress to drive volume change and SAXS to measure intermolecular spacing allows characterization of these intermolecular force balance mediated by cations.<sup>51-55</sup> Importantly, in the context of this work, the DeRouchey lab has recently learned how to separate and quantitate attractive and repulsive contributions to the overall force.

From the previous studies, we know that the osmotic curves shown in Figure 3.4 can fit into a double-exponential equation with variable pre-exponential factors A and R<sup>56</sup>:

$$\Pi = \Pi_R + \Pi_A = R e^{-2D/\lambda} + A e^{-D/\lambda} \quad (3.1)$$

where  $\Pi$  is the applied osmotic pressure,  $\Pi_R$  and  $\Pi_A$  are the repulsive and attractive forces respectively, and  $\lambda$  is the decay length.

For cations that spontaneously condensing DNA, the coefficients R and A can be related through equilibrium spacing,  $D_{eq}$ , since  $\pi(D_{eq}) = 0$ , then the coefficients can be combined into one, R.

$$A = -R e^{-D_{eq}/\lambda} \quad (3.2)$$

Substitute (3.2) into (3.1), then we can get

$$\Pi(D) = R e^{-2D/\lambda} - R e^{-D_{eq}/\lambda} e^{-D/\lambda} = R (e^{-2D/\lambda} - e^{-(D+D_{eq})/\lambda}) \quad (3.3)$$

or equivalently  $\log \Pi(D) = \log R (e^{-2D/\lambda} - e^{-(D+D_{eq})/\lambda})$

$$\begin{aligned} &= \log(R) + \log[e^{-2D/\lambda}(1 - e^{-(D_{eq}-D)/\lambda})] \\ &= \log(R) + \log e^{-2D/\lambda} + \log(1 - e^{-(D_{eq}-D)/\lambda}) \\ &= \log(R) + \frac{2D}{2.303\lambda} + \log(1 - e^{-(D_{eq}-D)/\lambda}) \end{aligned} \quad (3.4)$$

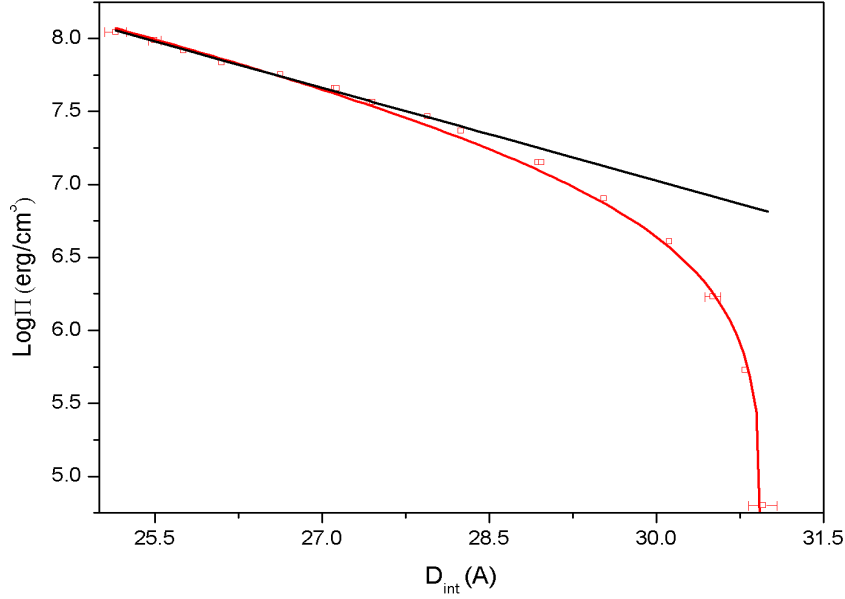


**Figure 3.4** Idealized osmotic stress force curves for condensed DNA (red) and free DNA (black).

Previous studies combining magnetic tweezing with osmotic stress/SAXS, it was shown that the attractive and repulsive forces were coupled as suggested by various theoretical models of DNA condensation including the electrostatic zipper model and hydration models. Consistent with the models, the experimental results showed that the decay length for the repulsive force was approximately half the decay length of the attractive force and were approximately  $2.5\text{\AA}$  and  $5.0\text{\AA}$  respectively. Using this constraint, we can measure osmotic stress force curves and describe the data with the double-exponential curve fits of equation 3.4 with only one free parameter,  $R$ .

As stated, the repulsive force  $\Pi_R = Re^{-2D/\lambda}$ , and the attractive force  $\Pi_A = Re^{-(D_{eq}-D)/\lambda}$  are coupled. In our work, where DNA is condensed by linear polycations or low generation PAMAM dendrimers into hexagonal structures we can use geometry to relate the osmotic measurements to the repulsive and attractive free energies. If the inter-helical spacing is  $D$  and the spacing change is  $dD$ , then the volume change of DNA is  $b\sqrt{3}DdD$ , where  $b$  is the rising of DNA along the helical axis between two base pairs,  $3.4\text{\AA}$ . Then the repulsive and attractive free energy

contribution by per DNA base pair can be calculated by integrating  $\Pi dV$  from  $\infty$  to  $D$ . Then we can get the free energy distributions as

$$\frac{\Delta G_R(D)}{kT} = \frac{\sqrt{3}b(\lambda/2)(D+\lambda/2)}{kT} \Pi_R(D) \quad (3.5)$$

and

$$\frac{\Delta G_A(D)}{kT} = \frac{\sqrt{3}b\lambda(D+\lambda)}{kT} \Pi_A(D) \quad (3.6)$$

This ability to codify the intermolecular forces will be used to understand how PAMAM mediates DNA-DNA forces different than comparably charged linear cations (Chapter 4) as well as the pH dependence of these forces (Chapter 5).

### 3.5 Summary

This chapter we focused on the basic theory of osmotic pressure. We discussed the definition of osmotic pressure and the effect factors. Also the mechanism of the osmometer was discussed. Because the unit used in the osmotic stress force curves are different from the osmolality determined by the osmometers, we also discussed unit transformation here. Then we discussed briefly how to couple osmotic pressure with SAXS for the determination of intermolecular forces in macromolecular systems that form condensed arrays.

## Chapter 4 The Role of Cation Architecture on DNA Condensation

(This chapter is taken from paper “An, M.; Parkin, S. R.; DeRouchey, J. E. Intermolecular forces between low generation PAMAM dendrimer condensed DNA helices: role of cation architecture. *Soft Matter* 2014, 10, 590-599” with permission from Royal Society of Chemistry)

### 4.1 Introduction

Cationic dendrimers have shown potential as gene delivery vectors due to their ability to condense DNA and protect it from cellular and restriction nuclease.<sup>57-60</sup> Dendrimers are hyperbranched macromolecules with precisely defined molecular weights and highly symmetric branches stemming from a central core. Each generation of dendrimer represents an iterative growth step resulting in twice the number of reactive surface groups of the preceding generation. Due to their potential as gene delivery agents, characterization of packaging and forces within cationic dendrimer-DNA complexes, or dendriplexes, is needed. Theoretical studies and simulations have predicted behaviour similar to a semi-flexible polyelectrolyte interacting with a hard sphere with wrapping of DNA around dendrimers or so-called ‘beads on a string’ structures possible.<sup>61,62</sup> However, early experimental studies have shown highly varied results with relation to the structure inside the dendriplexes. Depending on the dendrimer chemistry and generation, tetragonally and hexagonally packaged columnar mesophases, as well as DNA wrapping, have been reported in dendrimer–DNA complexes as observed by small angle X-ray scattering (SAXS), atomic force and transmission electron microscopy (AFM and TEM) experiments and single molecule tweezing.<sup>15,26,63-71</sup> While large generation dendrimers are thought to have spherical shapes, low generation dendrimers are estimated to be more disc-like.<sup>72</sup> In this Chapter, we focus on low generation poly(amidoamine) (PAMAM) dendrimers.

The physical origins of the forces acting on DNA condensation are still debated. Experimental studies have aimed to elucidate the fundamental physical mechanisms responsible for DNA condensation.<sup>53,55,73-80</sup> *In vitro* experiments have shown that DNA condensation from bulk solution critically depends on the cation net charge. Typically +3 or larger cations are required to overcome the inherently large electrostatic repulsive barrier between the like-charged double stranded DNA.<sup>81,82</sup> Upon condensation, the resulting compacted structures have well defined equilibrium surface separations. Depending on the identity of the cation, these surface separations between DNA helices range from 7-15 Å. The finite separation of helices indicates a delicate balancing of a short range repulsive force with a longer range attraction.<sup>73,77,78</sup> Concurrent to experiments, theoretical studies have also been pursued to shed light on the nature of these condensed soft matter phases. This work is driven in part due to the inability of classical Poisson-Boltzmann (PB) mean-field theory to fully explain the observed attractions in DNA condensation.<sup>83</sup> Theoretical treatments of the interhelical forces range from classical electrostatics in a continuum dielectric<sup>84-86</sup> to hydration interactions that emphasize the disruption of water structures in tight spaces.<sup>37,73,77</sup> To account for the attractions driving DNA condensation, these theories require correlations of charges or water structuring. A recently proposed electrostatic zipper model by Kornyshev and Leikin provides a convenient model for discussing correlation and attraction.<sup>23,87,88</sup> They propose binding of cationic charges in the major or the minor grooves, thus leading to attractive interhelical correlations between the bound positive charges and the phosphate backbone of apposing helices. Experimental studies suggest such groove binding is present in a variety of linear polycations.<sup>89-93</sup> Hyperbranched polycations, such as polycationic dendrimers, presumably would not be able to bind to DNA and correlate their charges with the phosphates of adjoining DNA in the same manner as linear cations. Other binding modes, such as bridging interactions between DNA double helices, may be necessary to induce condensation with dendrimers.<sup>22,94-97</sup>

Osmotic stress combined with x-ray diffraction allows us to directly measure

fundamental molecular scale interactions between DNA helices in ordered assemblies. It was previously shown both attractive and repulsive forces can be described by exponential functions with fixed  $\sim 2.5$  Å and  $\sim 5$  Å decay lengths for DNA condensed by a wide variety of cations including  $\text{Co}(\text{NH}_3)_6^{3+}$ , spermidine<sup>3+</sup>, spermine<sup>4+</sup>, oligoarginines (Arg<sub>1</sub>-Arg<sub>6</sub>) and salmon protamine.<sup>77,78</sup> Recently we have learned how to separate and quantitate attractive and repulsive contributions to the overall force.<sup>53,78,80</sup> Herein, we have used low generation PAMAM dendrimers (G0-PAMAM (+4) and G1-PAMAM (+8)) to condense high molecular weight DNA. The force curves of hyperbranched PAMAM molecules are compared to linear arginine peptides of the same net charge (tetra-arginine [R<sub>4</sub><sup>+4</sup>] and octa-arginine [R<sub>8</sub><sup>+8</sup>]). We have previously shown a length dependent attraction resulting in higher packaging densities with increasing charge for linear cations.<sup>78,80</sup> Our results show PAMAM-DNA complexes give lower DNA packaging densities with higher dendrimer generation number. Fits to the force curve data suggest this packaging difference arises from both increased repulsions and greatly reduced attractions in PAMAM-DNA compared to the linear cation. We also examined the salt and pH dependence on packaging in dendrimer-DNA complexes compared to the arginine-DNA complexes. The increased pH and salt sensitivities of PAMAM polyplexes are suggestive that different binding modes may be active in the hyperbranched cations.

## 4.2 Materials and Methods

### 4.2.1 Materials

Polyamidoamine (PAMAM) dendrimers (Generation 0 and Generation 1, ethylenediamine core, amine-terminated and 20 wt% solution in methanol) were obtained from Sigma-Aldrich (St Louis, MO). Before use, methanol was removed under reduced pressure at room temperature using a Labconco Centrivap. G0- and G1-PAMAM were subsequently dissolved in deionized water and buffered with acid or base to the desired pH. Tetra-arginine (R4) and octa-arginine (R8) peptides were custom synthesized and purified (>98%) by GenScript Corporation. The peptides

were neutralized with Tris base and used without further purification. Bioultra grade polyethylene glycol (PEG), with an average molecular weight (MW) of 8000, was purchased from Fluka Chemical Co. All chemicals were used without further purification. Highly polymerized calf-thymus DNA sodium salt (molecular weight  $\sim 10\text{--}15$  million daltons) was purchased from Sigma-Aldrich and subsequently purified by phenol/chloroform extraction to remove excess proteins. High molecular weight DNA ( $>5 \times 10^6$ ) was prepared and purified from adult chicken whole blood as described previously.<sup>98</sup> After purification, both chicken blood and calf-thymus DNA were extensively dialyzed against 10mM Tris-HCl (pH 7.5) and 1mM EDTA. The successful removal of protein was verified by measuring the ratio of absorbance at 260 nm and 280 nm of DNA solutions ( $A_{260}/A_{280}$ ) and it was found to be acceptable with values  $>1.8$ .

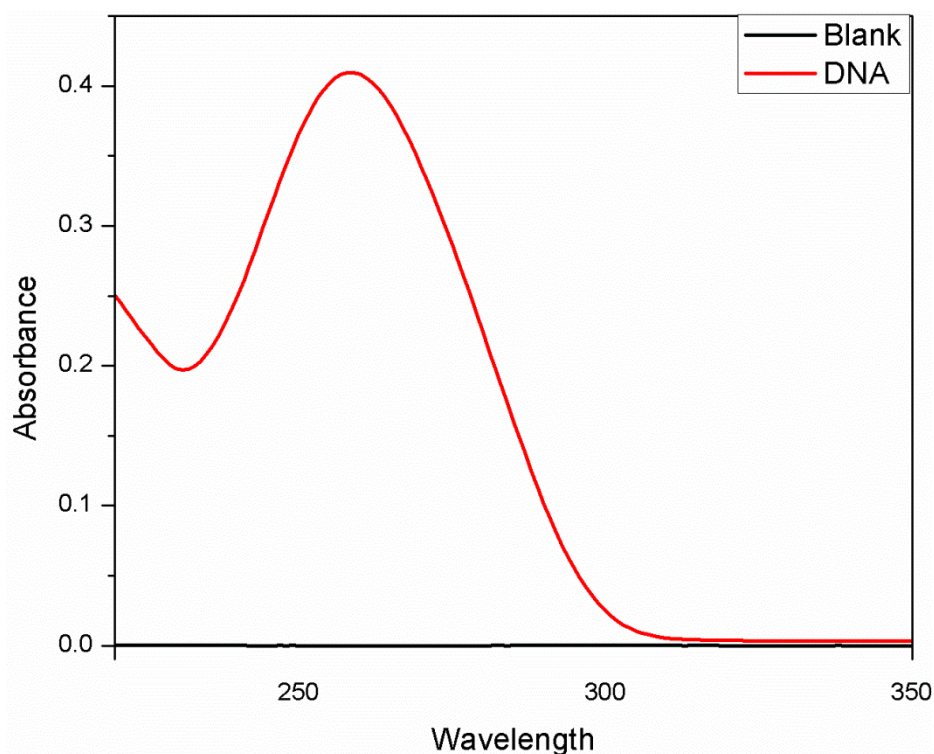


**Figure 4.1** UV-vis absorption spectra of DNA in buffer solution. DNA concentration was determined by using the  $A_{260}$  while DNA purity was verified by the  $A_{260}/A_{280}$  ratio.

#### 4.2.2 Sample Preparation

For all four cations used in this study (R4, R8, G0-PAMAM and G1-PAMAM), DNA spontaneously precipitates and samples for X-ray scattering were prepared in one of two ways. Concentrated polycation solutions were added to 1mg/mL chicken erythrocyte DNA or calf-thymus DNA (~250 mg of DNA) in 10 mM Tris-HCl (pH 7.5) in steps of 0.2 mM. Each addition was thoroughly mixed before adding more condensed ions and the process was continued until all DNA was precipitated. Alternatively, condensing cations were added to DNA in a single aliquot to an equivalent final concentration. Typically, the cation to DNA phosphate ratio was 1.5–2 at the end point. The resulting fibrous samples were centrifuged at ~10 000g for 10 min and transferred to corresponding PEG–salt solutions and allowed to equilibrate for ~2 weeks. X-ray scattering profiles did not depend on the type of DNA (calf thymus or chicken blood) or the method used to prepare the DNA precipitate. No change in the X-ray scattering pattern was observed after 6 months of storage. PEG osmotic pressures were measured directly using a Wescor Vapro Vapor Pressure Osmometer (model 5660).

For pH dependent studies, samples were prepared with calf thymus DNA dissolved in deionized water. Cations were dissolved in water and buffered to the desired pH (pH range 4–8) with HCl or NaOH. Condensed DNA was then prepared as described above and equilibrated for 2 weeks in pH appropriate buffer. A second set of pH experiments were performed by condensing calf thymus DNA with cations buffered to pH 5 or pH 8 as described above. After equilibration, these samples were examined by SAXS to determine the interhelical spacing,  $D_{int}$ . Subsequently, these condensed DNA samples were then equilibrated for 2 weeks in the opposite pH solution and measured by SAXS to determine the change in  $D_{int}$  after changing the pH bath solution.

#### 4.2.3 Critical Concentrations

The critical concentration of each condensing cation used for precipitation of DNA from dilute solution was determined as described by Pelta et al.<sup>30</sup> A series of DNA samples was prepared with varied cation concentrations in 10mM Tris buffer. The DNA concentration was  $\sim 15 \mu\text{M}$  base pairs in a total volume of 1 mL. After incubation at room temperature for  $\sim 1$  hour, the solution was centrifuged at 16 000g for 10 min and the DNA absorbance at 260 nm of the supernatant was measured. Critical concentrations were observed to decrease approximately by an order of magnitude for each additional charge, as seen by others.<sup>99,100</sup> The cation concentrations used in the bathing PEG–salt solution for the osmotic stress measurements were  $\sim 2$ – $10$  fold higher than the critical concentration. Over this range, the observed spacing between helices does not depend on the cation concentration.

#### **4.2.4 Osmotic Stress**

The method for direct force measurements by osmotic stress has been previously described in detail.<sup>37,73</sup> In brief, condensed macromolecular arrays, such as DNA, are equilibrated against a bathing polymer solution of known osmotic pressure. The bathing polymer, typically PEG, is too large to enter the condensed DNA phase, thus applying a direct osmotic pressure on the condensate. Water, salt, and other small solutes are free to exchange between the PEG and condensed DNA phases. After equilibration, the osmotic pressures in both phases are the same. Using small-angle X-ray scattering (SAXS),  $D_{int}$  can be determined from the Bragg scattering of X-rays as a function of the applied PEG osmotic pressure to obtain force-versus-separation curves.

#### **4.2.5 X-ray Scattering**

Graded-multilayer focused Cu K $\alpha$  radiation from a Nonius FR-591 rotating anode fine-focus X-ray generator operating at 45kV and 20mA was used for the small-angle X-ray scattering experiments. The primary beam cross-section was limited using a

fine rear aperture beam tunnel. Samples were sealed with a bath of equilibrating solution in the sample cell and then mounted into a sample holder at room temperature (25°C). The flight path between the sample and the detector was filled with helium to minimize background scattering. Diffraction patterns were recorded with a SMART 6000 CCD detector, with phosphor optimized for Cu K $\alpha$  radiation. The images were analyzed with Fit2d and Origin 8.0 software. The distance from the sample to detector, calibrated using silver behenate, was found to be ~23.2 cm. In typical scattering experiments, we see not only the Bragg reflection, to determine the interaxial DNA-DNA spacings, but also weak higher order diffraction typical of hexagonal packaging. The Bragg spacing is calculated as  $D_{Br}=2\pi/Q_{100}$ , where  $Q_{100}$  is the scattering vector,  $Q$ , which corresponds with the maximum in the scattering.  $Q$  is defined as  $Q = (4\pi/\lambda) \sin \theta$  where  $2\theta$  is the scattering angle. For a hexagonal lattice, the Bragg spacing,  $D_{Br}$ , and the actual distance between helices,  $D_{int}$ , are related by  $D_{int} = (2/\sqrt{3})D_{Br}$ . For different samples equilibrated under the same PEG-salt conditions,  $D_{int}$  values were reproducible to within ~0.1 Å. X-ray scattering patterns were reproducible over at least 6 months of storage and no sample degradation was apparent. Typical exposure times were of the order of 2 min.

#### 4.2.6 Force Analysis

We fitted the osmotic pressure  $\Pi$  versus spacing  $D$  curves to a double exponential equation with variable pre-exponential factors A and R:

$$\Pi(D) = \Pi_R(D) + \Pi_A(D) = R e^{-2D/\lambda} + A e^{-D/\lambda} \quad (4.1)$$

or equivalently

$$\log(\Pi(D)) = \log(R) - \frac{2D}{2.303\lambda} + \log\left(1 + \frac{A}{R} e^{D/\lambda}\right) \quad (4.2)$$

with decay length fixed at 5 Å. This form and decay length constraint are the result of experiments combining osmotic stress measurements with single molecule, magnetic tweezer experiments to separate the attractive and repulsive free energies at the equilibrium spacing for several commonly used condensing agents. Equation (2) with

$\lambda = 5.0 \text{ \AA}$  gives very good fits for the arginine-DNA complexes previously examined. The results are only slightly dependent on the decay length  $\lambda$  over the range of approximately  $\pm 0.5 \text{ \AA}$ . For cations that induce DNA condensation, such as those used in this study, the coefficients R and A are connected through the equilibrium interaxial spacing  $D_{eq}$  because  $\Pi(D_{eq}) = 0$ , giving a fitting equation with only a single variable R.

$$\log(\Pi(D)) = \log(R) - \frac{2D}{2.303\lambda} + \log(1 - e^{-(D_{eq}-D)/\lambda}) \quad (4.3)$$

Assuming the DNA were packed into hexagonal structure, the repulsive and attractive free energy contributions per DNA base pair can be calculated as a spacing  $D$  by integrating  $\Pi dV$  for each exponential from  $\infty$  to  $D$ ,

$$\frac{\Delta G_R(D)}{kT} = \frac{\sqrt{3}b(\lambda/2)(D+\lambda/2)}{kT} \Pi_R(D) \quad (4.4)$$

and

$$\frac{\Delta G_A(D)}{kT} = \frac{\sqrt{3}b\lambda(D+\lambda)}{kT} \Pi_A(D) \quad (4.5)$$

where b is the linear spacing between DNA base pairs,  $3.4 \text{ \AA}$ .

## 4.3 Results

### 4.3.1 Packing and Forces in DNA Condensed with G0-PAMAM, G1-PAMAM, Tetraarginine (R4), and Octaarginine (R8)

Figure 4.2 shows the osmotic stress curves for G0-PAMAM (G0) and G1-PAMAM (G1) condensed DNA. Plotted are log osmotic pressure ( $\Pi$ ) values versus DNA interaxial spacing,  $D_{int}$ . These dendrimer-DNA complexes were precipitated at pH7.5 and buffered with 10mM Tris (pH7.5) for all samples. Arrows show the interaxial spacing in the absence of applied osmotic pressure. Solid lines are fits of the data to eqn(4.3) with the decay length  $\lambda$  fixed at  $5.0 \text{ \AA}$ . Results depend only weakly on the decay length over the range of  $\sim \pm 0.5 \text{ \AA}$ . These fits allow us to separate the net force into its attractive and repulsive components. The protonation of

G0 and G1 was thoroughly studied previously<sup>101</sup>. At near neutral pH, PAMAM has the complete protonation of the primary amine groups at the dendrimer surface resulting in +4 and +8 surface charges for G0 and G1 respectively. The equilibrium spacing in the absence of applied osmotic pressure increases with increasing PAMAM generation. In addition, the high pressure data do not converge despite the similar chemical moieties on the surface amine groups as we have seen with other homologous cations.

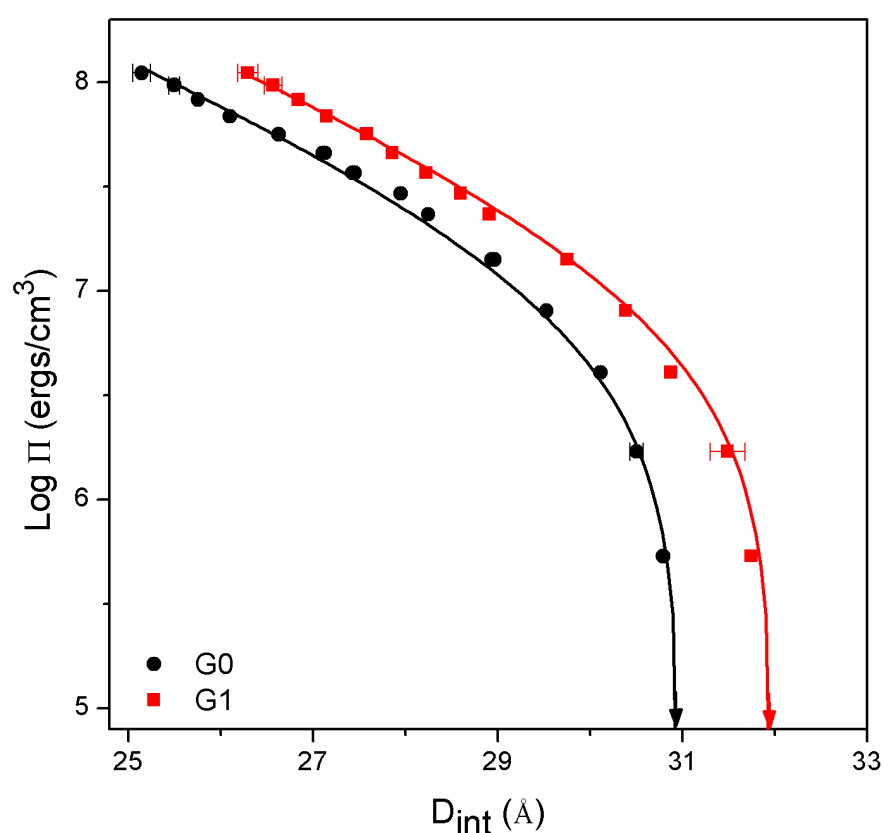


**Figure 4.2** Osmotic force stress curves are shown for DNA condensed by low generation (G0 and G1) PAMAM. The arrows indicate the equilibrium spacing in the absence of applied PEG osmotic pressure. The solid lines are fit of the data to eqn(4.3) with  $\lambda=5$  Å.

Figure 4.3 shows the osmotic stress curves for tetraarginine (R4) and octaarginine (R8) condensed DNA at pH7.5. These linear polycations are the charge equivalent

arginine peptides to G0 and G1. Arrows show the interaxial spacing in the absence of applied osmotic pressure. Solid lines are fits to eqn (4.3) with  $\lambda$  fixed at 5.0 Å. As reported previously, despite starting at very different equilibrium spacings without applied osmotic pressure, the high pressure data converge to the same high pressure limit. To emphasize this convergence at high pressure, we have also plotted previously published data for R4, R6 and poly-arginine (MW ~35.5 kDa, PArg)<sup>78</sup>. Increasing the number of arginines in this linear series results primarily in an increase of the magnitude of the 5.0 Å attractive decay length. At the highest osmotic pressures, the 2.5 Å repulsive decay length dominates and is only slightly dependent on the

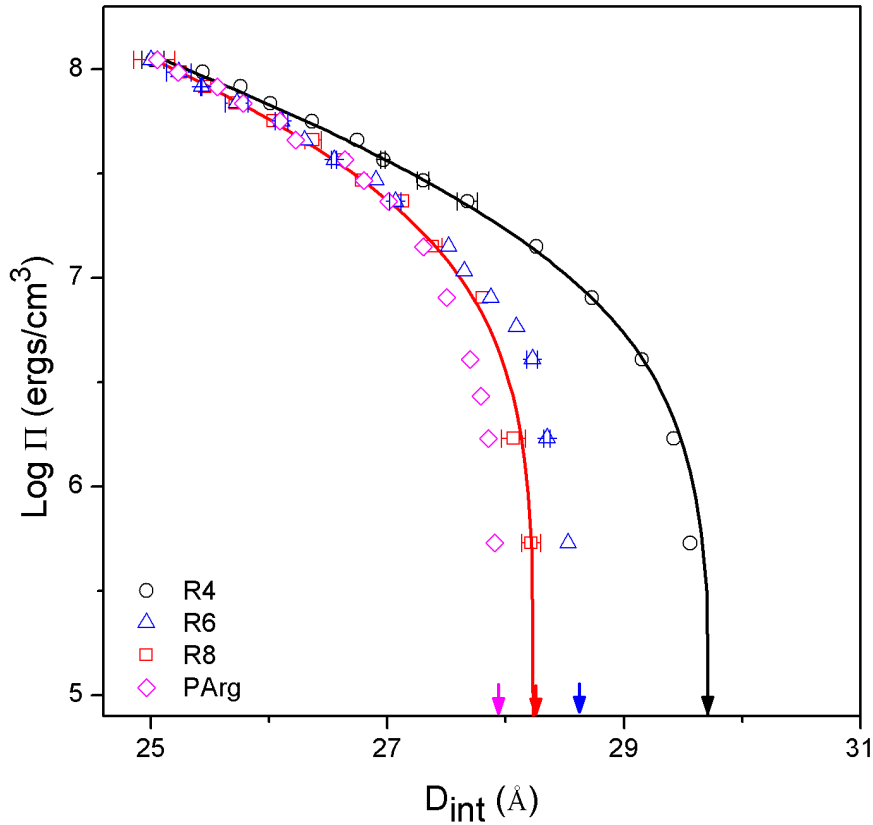


**Figure 4.3** Osmotic stress force curves are shown for DNA condensed by tetraarginine (R4) and octaarginine (R8) peptides. The arrows indicate the equilibrium spacing in the absence of applied PEG osmotic pressure. The solid lines are fits of the data to eqn(4.3) with  $\lambda=5$  Å. Also shown are hexaarginine (R6) and polyarginine data published previously.

number of arginines. We previously showed that the attractive free energy for linear arginine has a  $\sim 1/N$  dependence for the arginine series from R2 through R6 and poly(Arg).<sup>78</sup> The R4 and R8 data shown in Fig.4.3 are consistent with these previous observations.

Figure 4.4 shows typical X-ray scattering intensity profiles for all four cation polyplexes in Tris buffer (pH 7.5) without additional salt. Without applied osmotic pressure, the equilibrium interaxial spacings,  $D_{int}$ , between helices in G0-DNA and G1-DNA complexes are 31.0 Å and 32.0 Å ( $\pm 0.1$  Å) respectively. R4-DNA and R8-DNA have  $D_{int}$  of 29.8 Å and 28.3 Å ( $\pm 0.1$  Å), respectively. The sharp peak for all complexes is the helix-helix Bragg reflection. The peaks at larger  $Q$  are consistent with 101 and 110 reflection for a hexagonal lattice. These higher order reflections are indicated by arrows in Fig. 4.4. The presence of these higher order reflections has been previously assigned as evidence of the binding of cations in grooves<sup>89</sup>. The amplitude of these higher order reflections is much larger for the linear arginine condensed polyplexes than the hyperbranched PAMAM dendriplexes. We also note

**Table 4.1** The equilibrium interhelical spacings ( $\pm 0.1$  Å) from direct X-ray measurements and repulsive and attractive force component contributions to osmotic pressures ( $\pm 0.5\%$ ) and free energies ( $\pm 0.5\%$ ) at 25 Å calculated from fits to force curves are shown for DNA condensed by R4, R8, G0- and G1-PAMAM

Cation	$D_{eq}$	$\Pi_R(25\text{Å})$ ( $10^8 \text{ er cm}^{-3}$ )	$\Pi_A(25\text{Å})$ ( $10^8 \text{ er cm}^{-3}$ )	$\Delta G_R(25\text{Å})kT$ per base pair	$-\Delta G_A(25\text{Å})kT$ per base pair
R <sub>4</sub>	29.8	1.91	0.74	1.89	1.59
R <sub>8</sub>	28.3	2.35	1.23	2.32	2.64
G0-PAMAM	31.0	1.80	0.55	1.79	1.18
G1-PAMAM	32.0	2.67	0.66	2.64	1.43

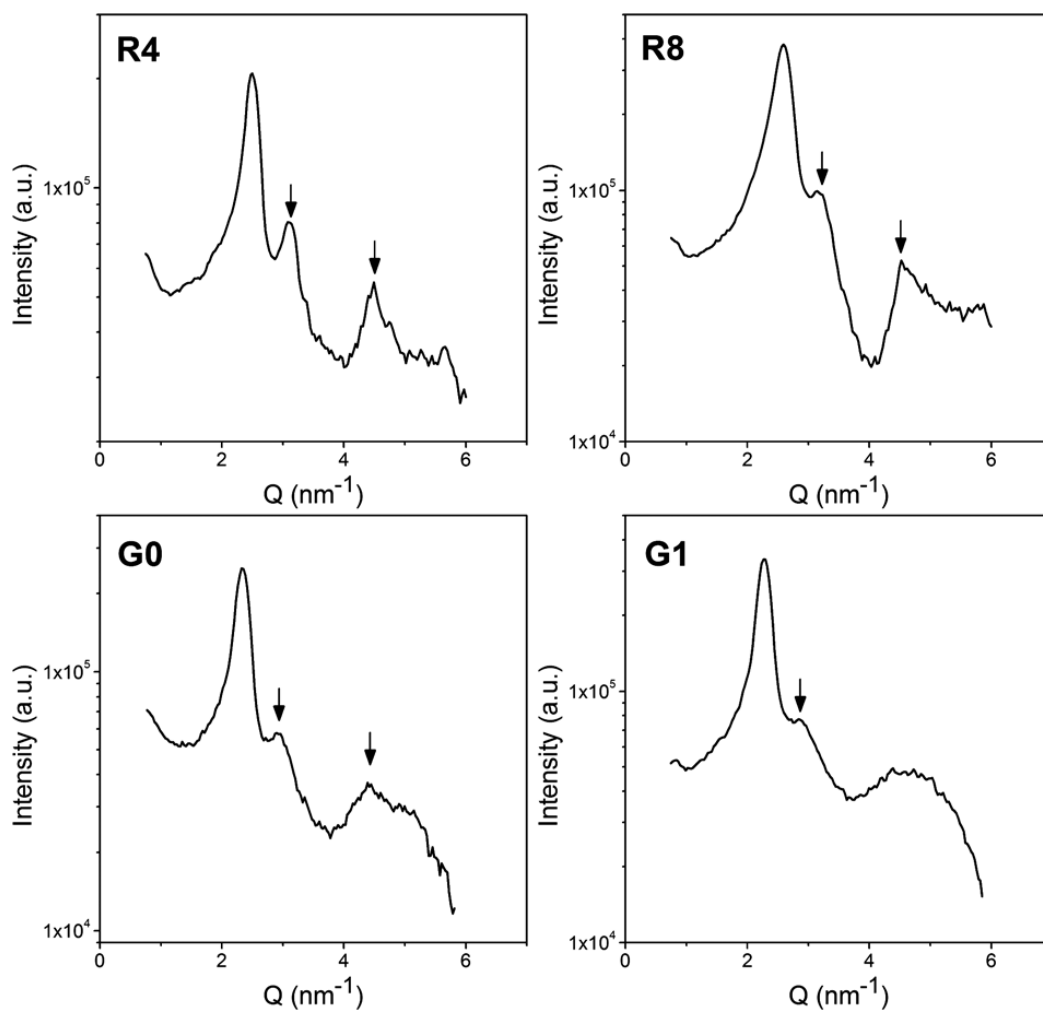


**Figure 4.4** Small-angle X-ray scattering (SAXS) profiles of DNA assemblies condensed by R4, R8, G0-PAMAM, and G1-PAMAM in 10 mM Tris, pH 7.5. Higher order reflections are consistent with (101) and (110) reflections of a hexagonal lattice. These reflections are clearly evident in R4 and R8 condensed DNA. G0-PAMAM also shows these peaks but they are reduced. G1-PAMAM shows further reduction of the (101) reflection and no evidence of the (110) reflection.

that while the PAMAM dendriplexes do maintain a 101 reflection, the 110 reflection ( $Q \sim 4.5\text{--}5 \text{ nm}^{-1}$ ) is very weak in G0-DNA and non-existent in the larger G1-DNA samples. The equilibrium spacings, osmotic pressure contributions at 25 Å,  $\Delta\Pi_R$  (25 Å) and  $\Delta\Pi_A$  (25 Å), and the free energy contributions  $\Delta G_R$ (25 Å) and  $\Delta G_A$ (25 Å) for the PAMAM and arginine cations are given in Table 4.1. The free energy contributions show that PAMAM dendrimers have comparable repulsive

contributions to their arginine equivalents. G1 has increased repulsions compared to R8. Significantly, the attractive free energy contributions are greatly reduced for both G0 and G1 when compared to the linear R4 and R8 systems.

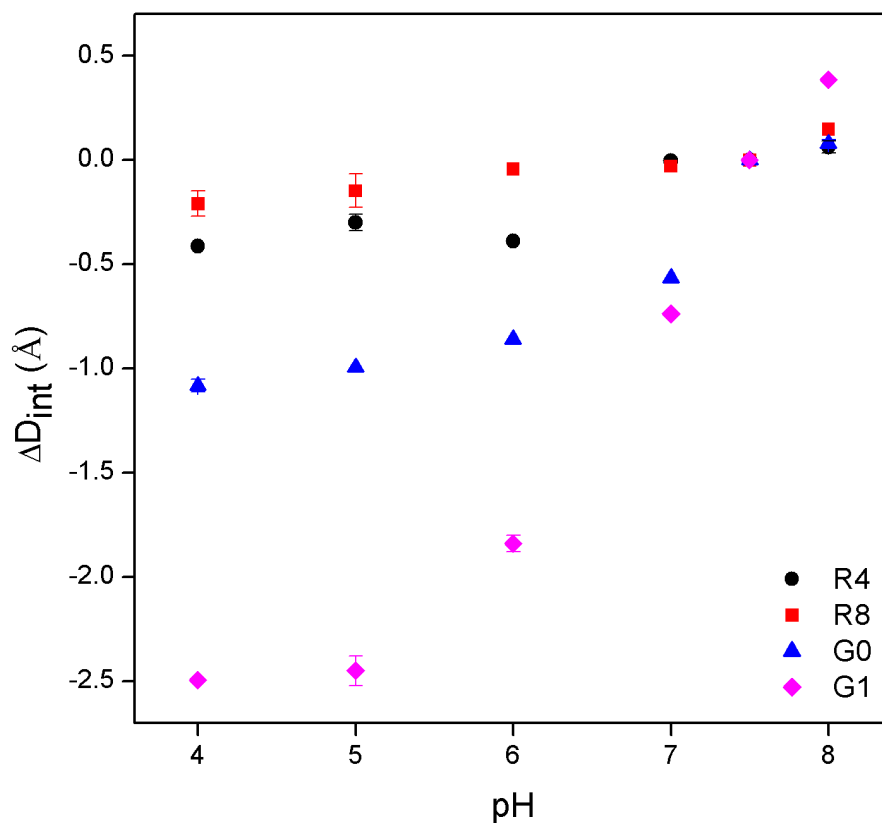


**Figure 4.5** Effect of changing pH at condensation. The changes in inter-helical spacings ( $\Delta D_{int} = D_{int,pH} - D_{int,Tris}$ ) are shown as a function of the solution pH at condensation. All cations are normalized relative to condensation at 10 mM Tris, pH 7.5.

### 4.3.2 Role of pH on Equilibrium Spacings

To investigate the role of pH on the resulting equilibrium interaxial spacings, two sets of experiments were performed. In the first set of experiments, condensing agents were buffered to different pH values (pH 4–8) from stock solutions with HCl or NaOH. Calf thymus DNA in distilled water was then precipitated with the pH buffered cations as described in the Methods section. Samples were equilibrated for

two weeks in fresh pH buffered aqueous solutions with a slight excess of polycation to maintain the cation concentration above the critical concentration. It is known that at lower pH, the tertiary amines of PAMAM can become protonated thus shifting the charge density higher. Such pH effects are not expected in arginine peptides over most pH values because the pKa value of the guanidyl group in arginine is  $\sim 12.5$ . Fig.4.5 shows the results of the equilibrium spacing as a function of the pH at condensation for R4, R8 and G0, G1 PAMAM condensed DNA. Here, we plot the change in interhelical spacing  $\Delta D_{int}$  relative to precipitation in 10 mM Tris, pH 7.5 ( $\Delta D_{int} = \Delta D_{int,pH} - \Delta D_{int,pH7.5}$ ). As pH decreases, we see decreasing equilibrium spacings for all four cationic species. As expected R4 and R8 show only slight changes ( $\sim 0.3\text{--}0.5$  Å) in equilibrium spacings over the pH range studied. PAMAM complexes show significantly larger pH dependence. G0 changes  $\sim 1.2$  Å between pH 4 and 8 while  $D_{int}$  changed  $\sim 2.9$  Å for G1 over the same pH range. At pH 4, the DNA interhelical spacing is now smaller for G1 than for G0, the opposite of pH 8. These differences highlight the pH sensitivity of the resulting packaging densities in PAMAM dendriplex complexes.

In the second set of experiments, PAMAM–DNA was condensed at pH 5 and pH 8. Samples were equilibrated for one week and measured by SAXS to determine the interaxial equilibrium spacing,  $D_{int}$ . The measured equilibrium spacings were consistent with the pH results described in Fig. 4.5. The change in equilibrium spacing between condensation at pH5 and pH8 was  $\sim 1.1$  Å and  $2.8$  Å for G0 and G1 respectively. The condensed PAMAM–DNA condensates were then switched from pH 5 to pH 8, re-equilibrated, and examined by X-ray diffraction to determine the effect of changing the buffer pH on the condensed PAMAM-DNA fibers. Results are shown in Table 4.2.  $D_{int}$  values were reproducible to within  $\sim 0.1$  Å. Although large changes in  $D_{int}$  were observed upon changing the pH at condensation for PAMAM-DNA, once condensed the effect of pH change on  $D_{int}$  was significantly smaller. A change in pH buffer solutions was evidenced most clearly in G1. Condensing DNA with G1 at pH 5 and then subsequently equilibrating at pH 8 was

observed to increase its interaxial spacing. However, the observed increase of 1.4 Å is only about half of the observed  $D_{int}$  change measured when DNA was condensed by G1 at pH 5 and pH 8. Condensing at pH 8 and then equilibrating to pH 5 resulted in a shift of the  $D_{int}$  for G1-DNA of  $\sim 0.7$  Å from 32.3 Å to 31.7 Å. DNA condensed by G0 displayed a similar behaviour. Both pH buffer changes on condensed PAMAM–DNA complexes were considerably smaller than the  $\Delta D_{int}$  observed from condensing DNA at different pHs. When returned to their initial pH conditions, the measured equilibrium spacings for both G0 and G1 condensed DNA were within 0.2 Å of their original values.

**Table 4.2** Effect of changing buffer pH after condensation for low generation PAMAM-DNA complexes. Samples were condensed at pH 5 or pH 8 and allow to equilibrate for two weeks and measured by X-ray scattering to determine interaxial DNA spacings. Samples were then placed in the opposite pH buffer, allow to re-equilibrate for two weeks and reexamined by scattering.

	G0-PAMAM		G1-PAMAM	
	Condensed at pH 5	Condensed at pH 8	Condensed at pH 5	Condensed at pH 8
$D_{int}$ , buffer pH 5	30.0 Å	30.9 Å	29.5 Å	31.7 Å
$D_{int}$ , buffer pH 8	30.2 Å	31.0 Å	30.9 Å	32.4 Å
$\Delta D_{int}$ , buffer change	0.2 Å	$\sim 0.07$ Å	1.4 Å	0.7 Å
$\Delta D_{int}$ pH at condensation	1.1 Å		2.8 Å	

#### 4.3.3 Salt Dependence of R4, R8, G0-PAMAM and G1-PAMAM

Figure 4.6 shows the interhelical spacing change as NaCl salt concentration is increased. In all the curves, the slight excess polycation concentration in the bathing solution was maintained in 10 mM Tris, pH 7.5. As phase transitions may occur with

increasing salt, we plot simply the salt dependence of the Bragg reflection  $D_{Br} = 2\pi/Q_{100}$ . Figure 4.6A plots the Bragg spacing dependence for all four cation condensed DNA systems as a function of added NaCl salt concentration. Figure 4.6B shows the relative change in the Bragg spacing compared to no excess salt ( $D_{Br,salt} - D_{Br,Tris}$ ) for each cation-DNA complex. All four samples show swelling of the DNA array with increasing added NaCl salt concentration; however the swelling behaviour is highly dependent on the condensing cation. With increasing salt, the DNA-cation fiber swells reaching a salt concentration where no Bragg scattering is observed within the sample. At even higher NaCl salt concentrations, the samples completely dissolve. For the linear arginine cations, increasing the cation charge from R4 to R8 resulted in a significantly more salt stable complex. For R4-DNA, a steady increase in  $D_{Br}$  is observed for 0 to 150 mM added NaCl salt. Bragg scattering is no longer observed at 200 mM salt. The larger R8 shows the least dependence of  $D_{Br}$  on NaCl salt concentration. For R8-DNA complex, stable Bragg reflections are observed at 700 mM NaCl. By 800 mM NaCl, the Bragg reflections in R8-DNA are lost. This behaviour is in stark contrast to the PAMAM dendriplexes. For NaCl salt concentrations less than  $\sim 0.1$  M, the changes in spacing for  $G0^{+4}$  and  $R4^{+4}$  are quite similar. By 125 mM NaCl, G0-DNA swells significantly more than R4-DNA to  $D_{Br} \sim 30.0$  Å ( $D_{int} \sim 34.7$  Å). Bragg scattering is lost for G0-DNA by 150 mM NaCl. More pronounced is the difference between the octa-charged R8 and G1 condensed DNA systems. G1-DNA swells to  $D_{Br} \sim 33.2$  Å by 250 mM NaCl and all Bragg scattering is lost by 275 mM NaCl compared to 800 mM for linear R8.

Figure 4.7 shows typical scattering profiles with Bragg reflections for all four cation-DNA systems at low and high salt concentrations. The higher order reflections gradually disappear for all systems with increasing salt concentration. For R4 and R8, the scattering profiles predominantly a simple shifting of the sharp Bragg reflection to lower  $Q$  (i.e. larger DNA-DNA interhelical spacings). The PAMAM-DNA samples however display a significant peak broadening with increased salt concentration. For

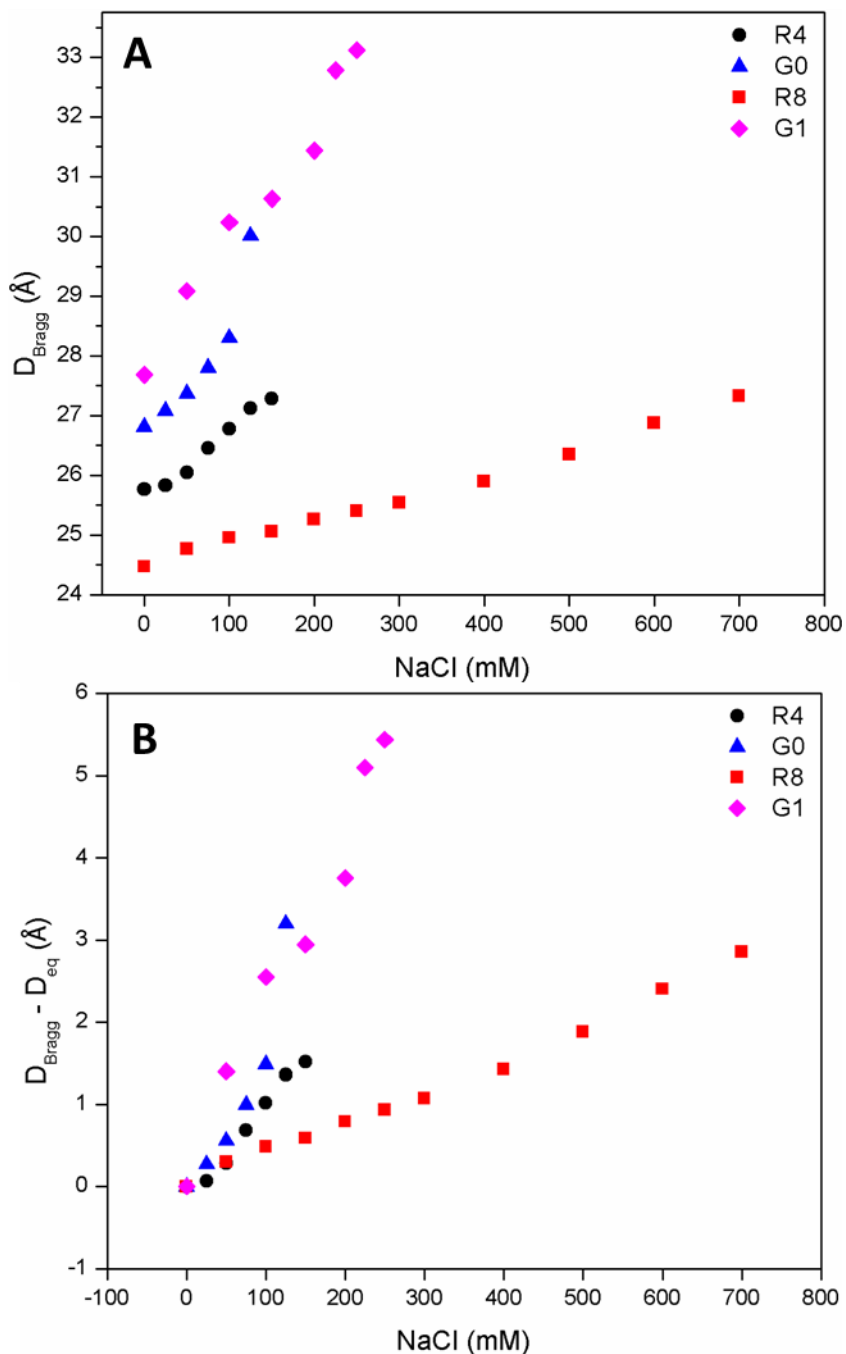


**Figure 4.6** (A) Bragg spacing dependence ( $D_{Br} = 2\pi/Q_{100}$ ) vs added NaCl concentration for R4, R8, G0 and G1-DNA systems. (B) The change in the Bragg spacing relative to  $D_{Br}$  in 10 mM Tris without added salt. The equilibrium solutions show no scattering at the next higher salt concentration in each series. (The uncertainty of the measurement is  $\pm 0.2$  Å)

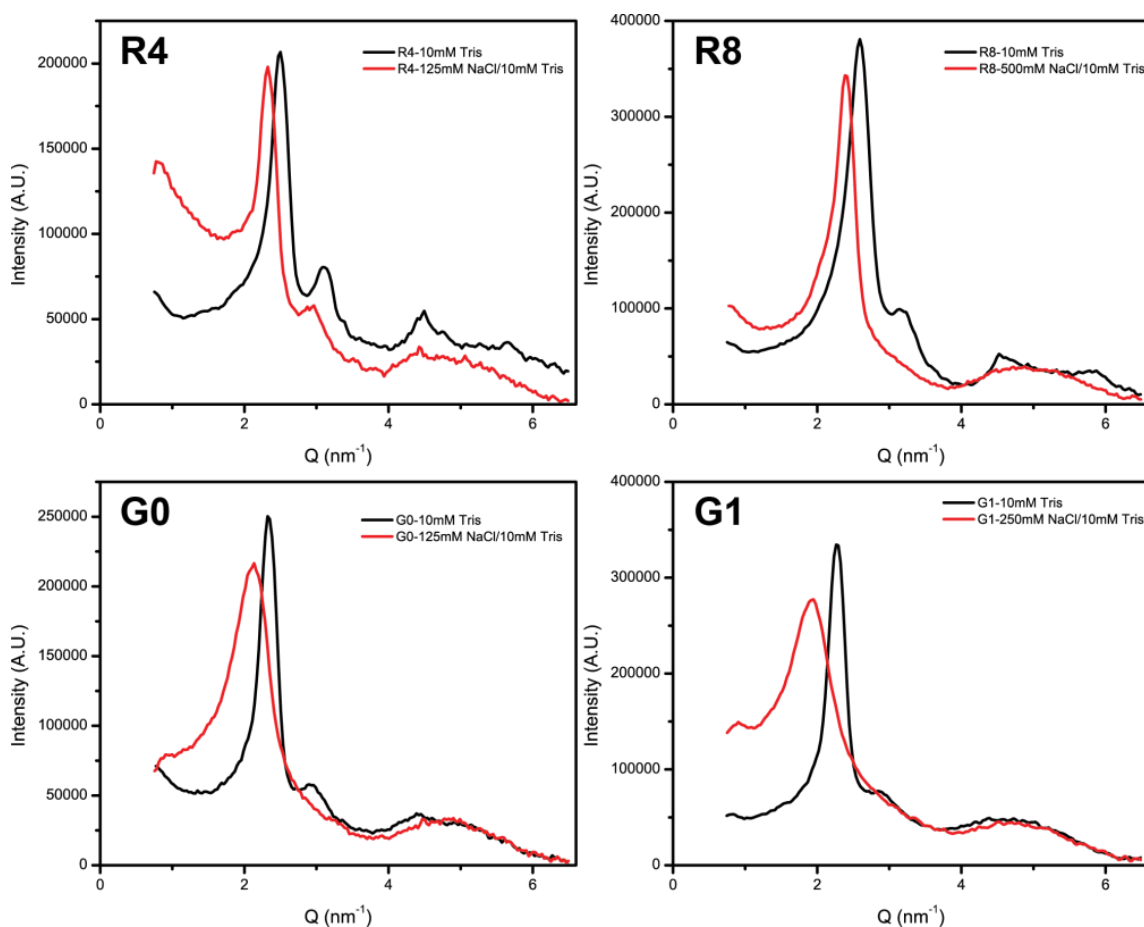


**Figure 4.7** Scattering profiles for DNA assemblies condensed by R4, R8, G0-PAMAM and G1-PAMAM at 10 mM Tris, pH 7.5 and with higher added NaCl concentration. All samples have a clear shift to lower  $Q$  (or equivalently larger  $D_{Br}$ ) with added salt. The arginine-DNA samples maintain a sharp Bragg peak at low and high salt concentrations while the G0- and G1-PAMAM show significant peaking broadening with added salt.

PAMAM condensed DNA, the Bragg peaks at high salt concentrations broaden approximately two times the width of the sharp low salt reflections. Such peak broadening is consistent with a columnar to cholesteric transition.

#### 4.4 Discussion

Much previous work has been done to study DNA condensed in vitro by a variety kinds of multivalent ions. Typically cations of net charge greater than +3 are capable

to condense DNA into hexagonal arrays. Depending on the cation used to condense, the DNA helices within these arrays do not touch and are separated by a  $\sim 7\text{--}15$  Å water layer. This water separation represents a balance of the repulsive and attractive forces within these soft matter phases. To account for the magnitude of attractions driving DNA condensation, most current theoretical models require a correlation of charge or water structuring. Typically, this charge correlation is accomplished by assuming cation binding into the DNA major or minor groves. Such correlations thus allow for the bound positive charges on one DNA to correlate and interact with the negative charged phosphate backbone of an opposing DNA helix. Prior experimental results have also suggested binding of linear cations within DNA grooves for a variety of linear cationic systems.<sup>90,102-105</sup> For dendrimers or spherical polycations, other binding modes such as cation bridging between DNA double helices have been proposed.<sup>95,97,106-108</sup>

Dendrimers are well known to condense DNA and protect nucleic acids from degradation by nucleases. However, the size and the hyperbranched nature of dendrimers are suggested correlation of charge (or water structuring) within DNA grooves is unlikely. Most of the structural studies to date observe hexagonal arrangement of DNA helices when condensing by low generation PAMAM dendrimers (< G4), similar to linear cations. The surface charge of G0 and G1 PAMAM dendrimer at neural pH is +4 and +8, respectively, and they have theoretical diameters of 15 Å and 22 Å. G0 and G1 condensed DNA at pH 7.5 have  $D_{int}$  of  $\sim 31$  and 32 Å. B-DNA has a diameter of 20 Å leaving 11 and 12 Å of water spacing between DNA helices in these PAMAM condensed DNA phases. The resulting spacings are smaller than the theoretical dendrimer diameters. While high generation dendrimers are predicted to be spherical in shape, low generation dendrimers are believed to be more of a disc-like shape which may help the low generation PAMAM within the DNA arrays. It is also important to note that B-DNA has major groove that the dimension is approximately 8.5 Å deep and 11.7 Å wide. Linear multi-valent cations such as metal ions, alkyl amines, and arginine and lysine

peptides are able to fit comfortably into DNA grooves. However, even low generation PAMAM dendrimer molecules are comparable to the major grooves dimensions. So PAMAM are presumably unable to access the DNA grooves. If unable to correlate within DNA grooves, other modes of binding, such as charge bridging across two DNA molecules may dominant the dendrimer-DNA reactions.

To investigate the role of cation architecture on DNA condensation, we have compared the osmotic stress curves for G0- and G1-PAMAM to the comparably charged tetra- and octa-arginine (R4/R8) linear peptides. Despite the simplicity of the double exponential form of eqn(4.2) and (4.3) with fixed 2.5 Å and 5.0 Å decay lengths gives good fits to all the force data shown in Figure 4.2 and 4.3. The equilibrium distances between DNA helices are determined by the balance of attractions and repulsions within the cation-DNA system and are cation specific. We previously showed using linear homologous peptides that the repulsive force is only weakly dependent on the peptide length (or equivalent charge) while the attractive force increases with the number of arginine residues and dominate the interaction at charges  $\geq +3$ . Combined, these attractions and repulsions result in the interaxial spacing between DNA helices decreasing with increasing number of residues in a linear homopeptide such as the arginine data shown in Figure 4.3. The attractive free energy measured for R4 and R8 in my study is consist with the  $\sim 1/N$  dependence for arginine series previously measured<sup>51</sup>. We argue that the  $1/N$  relationship is a result of translational entropy of the bound cation. In other words, there is less loss of entropy to correlate one +4 counterion than four +1 ions. We have shown that oligolysines and simple alkyl amines (putrescine<sup>2+</sup>, spermidine<sup>3+</sup>, and spermine<sup>4+</sup>) show a similar  $1/N$  behavior.<sup>51,52</sup>

DNA condensed by G0- and G1-PAMAM show completely opposite behavior in the force curves. While all four systems are well described by the double exponential formalism given in eqn(4.3), the attraction and repulsive forces show different trends for branched dendrimers compared to their charge equivalent linear arginines. Not

only does the interhelical spacing increase in Figure 4.2 with the increasing charges for PAMAM but the high pressure data do not converge despite the chemical similarity in the terminal primary amine groups for both PAMAM species. The results of the force curve fits in Table 4.1 indicate that the hyperbranched nature of the dendrimer results in a slightly higher repulsions and significantly reduced attractions compared to the linear cations. Increasing the linear arginine peptides from R4 to R8 results in a 66% increased attractions which overcome the ~23% increase in repulsions. These forces result in tighter DNA packaging for R8 compared to R4. In comparison, comparing G0 and G1 we see that the repulsions are increased ~47% while the increased attraction of the octavalent G1 is only ~21% greater than the tetravalent G0. The decrease in the long range attractive force amplitude is greater than the increase in the short range repulsive force. This decreased attraction is consistent with the notion that cationic dendrimers are unable to correlate their charges with phosphates of adjoining DNA in the same manner as the linear cations. Indeed, the attractions measured for G1 are even less than for R4. The corresponding additional repulsive force observed for PAMAM could be due to the compressibility of the branched dendrimer, but warranty further study.

The pH and salt dependencies of the DNA-DNA spacing at equilibrium for the cation-DNA complexes used in this study were determined by SAXS. PAMAM dendrimers have tertiary amine groups at each branching points and primary amine groups at the terminal. The protonation level of the PAMAM can be altered significantly by changing the solution pH. At physiological pH, the primary amines are protonated while at low pH, the tertiary amines can carry charges. G0 PAMAM has 4 primary and 2 tertiary amines. G1 has 8 primary and 6 tertiary amines. The charges on arginine peptides are relative insensitive to pH studied here because the  $pK_a$  value of the guanidyl group of arginine is ~12.5. Figure 4.5 shows the effect of changing pH at which condensation occurs for the arginine and PAMAM condensed DNA system from pH 4 to 8. Prior work showed that DNA condensation occurs when over 90% of its charge neutralized by counterions.<sup>109</sup> The increasing protonation state

of PAMAM at lower pH requires less mass of dendrimer to neutralize the charge of DNA phosphates. Less dendrimer within the condensate would presumably lead to more close packaging of the DNA helices as observed. The pH effect is as follows: tighter packaging of the DNA is observed for both G0 and G1 at low pH; however G1 showed significant larger difference in equilibrium spacing than G0 over the pH range studied. The linear arginine peptides (R4 and R8) also show a slightly decrease in  $D_{int}$  at low pH. This is perhaps because some protonation of the C-terminal carboxyl of these peptides ultimately increasing their overall net charge. If the C-terminal carboxyl of the arginines were partially protonated, we would expect tighter packaging of the DNA due to the previously discussed  $1/N$  dependence of the attractions. The  $1/N$  dependence is also consistent with the observation that the change in the equilibrium spacing ( $\Delta D_{int}$ ) is larger for R<sub>4</sub> than for R<sub>8</sub> as a larger relative change in attractive free energy would be expected upon moving from +4 to +5 than from +8 to +9.

Once condensed, changing the buffer pH does induce a shift in the equilibrium DNA spacing in the direction anticipated from Figure 4.5. However, the magnitude of spacing shift is significantly less as shown in Table 4.2. These results suggest that once bound the  $pK_a$ 's of the tertiary amines in PAMAM are shifted and their ability to protonate or deprotonate is different from PAMAM in free solutions. Interestingly, the ability to respond to pH is asymmetric. Both PAMAM-DNA complexes undergo a larger change in equilibrium spacing when condensed at low pH and then re-equilibrate at high pH than *vice versa*. When returned to their original pH, the  $D_{int}$  spacing did return to their original spacing within  $\pm 0.2$  Å. One explanation for this phenomenon is that the exchange of PAMAM from condensate and bulk solution may be slow and meta-stable.

Lastly, we examined the effect of NaCl salt on our PAMAM and arginine condensed DNA complexes. We have previously studied the salt dependence of protamine-DNA complexes showing that salt has a two-fold action: both anion binding

to the protamine and cation competition with protamine for DNA binding.<sup>54</sup> An increasing ionic strength would also screen possible electrostatic attractive forces. For linear cations, larger spacings at high salt concentrations suggest a decrease in attractive free energy due to a weakened correlation of the cation, or a decreased charge of the bound polycation with anion binding or increased shielding of charges on adjacent helices. If bridging or other binding modes are active in dendrimer-DNA complexes, it is reasonable to assume that the salt sensitivities would be different than the linear cation-DNA complexes. As shown in Figure 4.6, swelling occurs for all four systems. Both PAMAM systems are observed to swell to significant larger spacings and lose Bragg reflections at lower salt concentrations than their equivalently charged linear arginine peptides. The salt concentration at which the Bragg reflections was no longer observed was highly charge dependent for linear arginine shifting from  $\sim 200$  mM to  $\sim 800$  mM for R4 and R8 respectively. Over these NaCl salt concentrations  $D_{Br}$  swelled approximately  $1.5 \text{ \AA}$  and  $3 \text{ \AA}$  in total for R4 and R8 respectively. Interestingly, both arginines reached a  $D_{Br} \sim 31.5 \text{ \AA}$  at highest salt concentration. In contrast, the PAMAM complexes swell to much larger Bragg spacings increasing  $3$  and  $6 \text{ \AA}$  for G0 and G1 respectively with increased NaCl concentration. Despite of the doubling of the charge in G1, the slope of the Bragg spacing with increasing salt concentration was nearly identical to G0. Unlike arginine, the critical salt concentration at which Bragg spacing was lost for PAMAM mildly shifted from  $150$  mM to  $\sim 275$  mM with increasing generation number. Using protamine-DNA arrays, we previously showed that salt sensitivities were very dependent on salt species.<sup>54</sup> Specially, we showed that the attractive forces were weakened by a combination of anion binding and cation screening (competition). If anion binding dominates, such as for chaotropic anions, we observe strong dependence of spacings on salt concentration. Chaotropic anions are anions can disrupt the hydrogen forces between DNA molecules. If cation competition for binding dominates, then weak dependence of DNA spacings was observed. It is true that with anion binding ( $\text{Na}_2\text{SO}_4$  or  $\text{NaSCN}$ ), protamine-DNA spacings got much

larger before the pellets dissolved than for cation competition (NaF or NaOAc) as with R8 vs. G1. Here, however, these differences are likely arising from different binding modes for branched dendrimers and linear arginines.

In addition, while no significant peak broadening was detected for the arginine-DNA systems, PAMAM-DNA displayed significant peak broadening at high salt concentrations suggestive a phase transition from a hexagonal packaging of DNA to a more loosely ordered liquid crystalline phase. Previously, we observed in high molecular polyarginine-DNA complexes that such phase transitions occurred over a narrow range of salt concentrations. For such short polycations as the arginines used in this study, this range may be even narrower and therefore was not observed. PAMAM complexes appear to have this phase transition occur over a broader range of salt concentrations and thus are easily observed. Peak widths are indicative of the average in-plane domain sizes with sharper peaks suggestive of larger domain sizes. Such peak broadening is consistent with a phase transition at high salt concentrations from a columnar hexagonal phase to a more loosely ordered cholesteric liquid-crystal phase. Similar phase transitions were previously observed for larger generation PAMAM-DNA complexes.

#### **4.5 Conclusions**

The current study represents an investigation of the influence of cation topology on the resulting structures and forces within DNA complexes condensed by low generation PAMAM dendrimers. In order to condense DNA, linear cations are believed to bind into DNA grooves and to interact with the phosphate backbone of the opposing DNA helix. We have shown a length dependence of attraction resulting in higher packaging densities with increasing charges for linear cations. Dendrimers, such as PAMAM, due to the relatively large size and hyper-branched structure, are presumably to believe unable to bind into DNA grooves and correlate their charges in the same manner as linear cations. Using osmotic pressure, we have directly probe the DNA – DNA intermolecular forces within PAMAM dendrimer condensed DNA

complexes and compared them to DNA condensed by linear arginine peptides R4 and R8 which carried comparable charges to G0- and G1-PAMAM PAMAM, respectively. All complexes studied here are found to self-assemble into columnar hexagonal phases. The resulting osmotic stress curves for all four systems are well described by a double-exponential equation fitting with fixed 2.5 and 5.0 Å decay lengths. Separation of the attractive and repulsive contributions to the free energy tells us much about the cation-dependence thermodynamic forces in these systems. We show that DNA assemblies condensed by hyper-branched PAMAM dendrimers display significantly different physical behaviors compared to linear cation-DNA assemblies. DNA complexes condensed by PAMAM resulted in increased repulsive forces and greatly reduced attractions compared to linear arginine peptides with comparable charges. These changes in the intermolecular forces result in higher generation dendrimer gives lower DNA packaging densities, the opposite behavior of linear cations. In addition, significant differences in pH and salt dependencies are observed in PAMAM dendriplexes. Our data are highly suggested that other binding modes, such as bridging interactions between DNA double helices, may be necessary to induce condensation with dendrimers. These studies begin to elucidate the role of cation topography in DNA condensation.

## Chapter 5 Role of pH on DNA Condensation by Low Generation Dendrimers

(This chapter is taken from paper “An, M.; Hutchison, J. M.; Parkin, S. R.; DeRouchey, J. E. Role of pH on the Compaction Energies and Phase Behavior of Low Generation PAMAM–DNA Complexes. *Macromolecules* **2014**, *47*, 8768-8776.” with permission from American Chemical Society)

### 5.1 Introduction

Gene delivery is a complicated multistep process with the ultimate goal is to replace a defective gene sequence with a correct version of that gene. Currently gene delivery focuses on using viral or non-viral vectors to delivery nucleic acids into cells in a safe and efficient manner.<sup>17,110</sup> Viral vectors suffer from potential limitations including broad tropism, limited DNA packaging capacity, and the difficulties for large-scale production, thus it motivates the studies on the non-viral alternations.<sup>111</sup> Many non-viral systems rely on cationic polymers for both DNA packaging and facilitating gene delivery *in vivo*.<sup>112</sup> The possible benefits of cationic polymers over the viral vectors include low immunogenicity and the ease for chemical modification.<sup>59,113</sup> In recently years, cationic dendrimers have become attractive alternatives to the traditional linear polymers for gene delivery. Dendrimers are hyper-branched macromolecules with near uniform polydispersity and well-defined surface chemistries. Typically, dendrimers are built from an iterative fashion with concentric branching units stemming from the central core. With each growth step, or generation, doubling the reactive surface groups of the previous generation is achieved. Dendrimers have outstanding advantages compared to the linear cationic polymers which suffer from inherent problems including chain polydispersity and random attachment of the functional domains. DNA condensed by the commercial available cationic dendrimers such as poly(amido amine) (PAMAM) and polypropylenimine (PPI) are most studied dendrimer-DNA, or dendriplex, system for gene delivery. Both these dendrimers are capable condensing DNA and protecting nucleic acids from restriction nuclease.<sup>57,58,60</sup>

Successful gene therapy first requires a tightly packaged DNA through complexation of cationic agent to DNA, and then after delivered the condensed gene into the cells interested, the DNA must be unpackaged. Both packaging and unpackaging depend on the resulting structures and forces within the polycation-DNA complexes. To apply the dendriplexes successfully for therapy, there is a need to characterize the ultimate structure and compaction energies within the dendrimer-DNA complexes. Theoretical studies and simulations on semi-flexible polyelectrolyte interacting with charged spheres have predicted that the polymer chain wrap around the charged spheres and form the so-called “beads on string” (BOS) structures are possible.<sup>61,114</sup> And similar structures also have been predicted for DNA condensed by high generation dendrimers.<sup>115-118</sup> One of the first experimental studies conducted by Evans et al. showed that dendriplexes have a mesomorphic nature forming either 2D hexagonal or square columnar mesophases with G4 and G5 PPI dendrimers.<sup>63</sup> Further experiments with dendrimers of different chemistries and generations have shown highly conflicting results in terms of internal structures of DNA complexes. Dendriplexes with square, tetragonal, hexagonal structures, as well as DNA wrapping and BOS structures, have been reported as observed by small angle X-ray and neutron scattering (SAXS/SANS), atomic force microscopy (AFM), and single molecule experiments.<sup>15,28,64,66-71,119-121</sup>

Using osmotic pressure coupled with SAXS, we are able to measure the packaging and forces within the ordered DNA assemblies directly. In an earlier study, we compared DNA condensed by low generation PAMAM dendrimers (G0 and G1) to the linear poly arginines (R4 and R8), which carried the same amount of positive charges at neutral pH: +4 and +8 respectively.<sup>122</sup> The forces within the low generation PAMAM-DNA complexes are well described by exponential function with fixed 2.5 and 5.0 Å decay length. This form is consistent with the previous work on forces within DNA condensed by  $\text{Co}(\text{NH}_3)_6$  and a wide range of linear poly cations.<sup>51,52,123,124</sup> Using force measurements to quantitate the attractive and repulsive contributions to the overall forces, we have shown that DNA condensed by

hyper-branched PAMAM dendrimers display significantly different physical behaviors compared to the linear cation-DNA assemblies. These differences arise due to the PAMAM both having increased repulsions and significantly weakened attractions compared to the linear cations which carry the same amount of net charge. We argue that these difference arise due to that the hyper-branched dendrimer molecules are unable to bind into DNA grooves, as has suggested for the linear cations, but must use alternative binding modes such as bridging to induce condensation.

In this chapter, we will discuss studies performed to better understand the pH effects on low generation PAMAM dendrimer condensed DNA complexes. We have systematically investigated the package and compaction energies within G0- and G1-PAMAM dendrimer-DNA complexes condensed between pH 4 and pH 8. We have shown that changing pH at condensation has significant effects on the observed structures and phase behavior of the resulting PAMAM/DNA complexes. Due to the present of primary and tertiary amines with different pKa values in PAMAM dendrimers, changing pH will directly change the total net charge carried by PAMAM. At low pH, or higher net dendrimer charge, tighter DNA packaging is achieved. Despite changing with pH, different packaging densities are achieved at equilibrium, or zero applied pressure, we see a convergence of the force stress curves at high osmotic pressure for each dendriplex system. Fits to the force curves indicate that the repulsive contributions for a given PAMAM/DNA system are relatively insensible to pH changes while the attractions vary significantly. And the scaling is linear with the inverse of the net dendrimer charge. At last, we also examined the salt dependence of phase behavior in the PAMAM/DNA complexes as a function of pH at condensation. A universal phase behavior has been observed in both G0- and G1-PAMAM dendriplexes. That is a discontinuous phase transition was observed above a critical salt concentration,  $c^*$ . The critical salt concentration is both sensitive to dendrimer generation and pH at condensation.

## 5.2 Materials and Methods

### 5.2.1 Materials

Low generation PAMAM dendrimers (generation 0 and 1, ethylenediamine core, amine-terminated polyamidoamine) were purchased from Sigma-Aldrich (St Louis, MO). Before use, methanol was removed using a Labconco Centrivap at reduced pressure. Dendrimers were subsequently dissolved in appropriate buffer solution, and the final pH was adjusted with NaOH or HCl to the desired pH value (from pH=4 to 8). Bioultra grade poly (ethylene glycol) (PEG, 8 KDa) was obtained from Fluka Chemical Co. and used without further purification. Highly polymerized calf-thymus (CT) DNA sodium salt (molecular weight  $\sim 10\text{--}15$  million Da) was purchased from Sigma-Aldrich. High-molecular-weight chicken blood (CB) DNA (molecular weight  $> 5 \times 10^6$  Da) was prepared and purified from adult chicken whole blood as described previously.<sup>125</sup> CT and CB DNA were further purified by phenol/chloroform extraction to remove excess proteins followed by ethanol precipitation before use. After purification, both DNAs were dialyzed against 1 mM EDTA solution. The successful removal of protein from CB and CT DNA was verified by measuring the ratio of absorbance at 260 and 280 nm of DNA solutions and found to be satisfactory with values exceeding 1.8.

### 5.2.2 Sample Preparation

DNA was observed to spontaneously precipitate in the presence of both G0- and G1-PAMAM for all pHs used in this study. In preparing samples, both the DNA (CB or CT DNA) and dendrimer (G0 or G1) stock solutions were first separately dissolved in an appropriate 10 mM pH buffer. After dissolution, these stock solutions were further buffered with HCl or NaOH to achieve the desired final pH ( $\text{pH} \pm 0.1$ ). Buffers were used 10mM sodium acetate solution for pH 4, 10 mM MES solution for pH 6, and 10 mM Tris-HCl for pH 8 and pH 7.5. The double-helix structure of DNA is known to be stable over this pH range. Condensed DNA samples for X-ray

scattering were subsequently prepared in one of two ways. Concentrated PAMAM stock solutions were added to 1 mg/mL calf-thymus (CT) or chicken blood (CB) DNA in 10 mM pH buffer in a stepwise fashion. Each addition was mixed thoroughly before adding additional PAMAM, and the process continued until all DNA was precipitated. Alternatively, a single aliquot of condensing cations were added to DNA to an equivalent final concentration. The final cation amine to DNA phosphate ratio was approximately 1.2 at the end point. The resulting fibrous PAMAM-DNA samples were then centrifuged for 10 min and transferred to a 10 mM pH buffered PEG-salt solution and allowed to equilibrate ~2 weeks before X-ray analysis. X-ray scattering profiles did not depend on the type of DNA used or the sample method employed to prepare the DNA precipitate. In all samples, a small excess PAMAM concentration was maintained in the PEG-salt bathing solution to ensure cation concentration was above the critical concentration for these cations as previously determined. The observed spacing between helices does not depend on the excess cation concentration in the bath over an approximate 2–5-fold concentration range. X-ray scattering patterns were not observed to change even after several months of storage.

### **5.2.3 Osmotic Pressure**

The method for direct force measurements by osmotic pressure has been described previously in detail.<sup>123,126</sup> In brief, condensed DNA arrays equilibrate against a bathing PEG polymer solution with a known osmotic pressure. PEG chains are too large to enter into the condensed DNA phase, thus providing a direct osmotic pressure on the DNA condensates. In these samples, small molecules including water and salt are free to exchange between the PEG and condensed DNA phases. After equilibration, the osmotic pressures in both phases are the same. Osmotic pressure of the bathing PEG solutions were measured directly using a Wescor Vapro vapor pressure osmometer (model 5660). In the condensed state with low generation PAMAM, the DNA rods are found to be packaged in a hexagonal array for all pHs at low salt conditions. Using small-angle X-ray scattering (SAXS), the interaxial spacing

between DNA rods ( $D_{int}$ ) can be determined as a function of the osmotic pressure from the Bragg scattering of X-rays to obtain force-separation curves as described below.

#### 5.2.4 X-ray Scattering

X-ray scattering experiments were performed using graded-multilayer focused Cu K $\alpha$  radiation (1.54 Å) from a Nonius FR-591 rotating anode fine-focus X-ray generator operating at 45 kV and 20 mA. Samples were sealed in a sample cell with a bath of equilibrating PEG solution and mounted in a sample holder at room temperature. The flight path from the sample to detector was filled with helium gas to minimize air scattering, and the primary beam was collimated by a fine aperture beam tunnel. Diffraction patterns were recorded by a SMART 6000 CCD detector with phosphor optimized for Cu K $\alpha$  radiation. Fit2D and Origin 8.0 software were used to analyze all images. Calibration of the SAXS sample-to-detector distance was found to be 23.2 cm. Bragg scattering peaks were used to determine interaxial DNA-DNA spacings. Bragg spacings are calculated as  $D_{Br} = 2\pi/Q_{Br}$ , where  $Q_{Br}$  is the scattering vector,  $Q$  (defines as  $Q = (4\pi/\lambda) \sin(\theta)$ , where  $2\theta$  is the scattering angle), which correspond to the maximum in the scattering. For a hexagonal lattice, the relationship between the Bragg spacing and the actual interaxial distance between helices ( $D_{int}$ ) is calculated as  $D_{int} = (2/\sqrt{3})D_{Br}$ . For different samples equilibrated under the same PEG-salt conditions,  $D_{int}$  values were reproducible to within  $\sim 0.1$  Å. X-ray scattering patterns were reproducible over several months of storage, and there was no significant sample degradation due to X-ray exposure. Typical exposure times were 120 s.

#### 5.2.5 Force Analysis

G0- and G1-PAMAM are both able to condense DNA spontaneously *in vitro* into hexagonal DNA arrays with a finite separation at equilibrium between the DNA helices. We use the osmotic stress technique to directly probe the intermolecular

forces between the PAMAM condensed DNA. Previous studies indicate that DNA-DNA forces are well described by two exponentials at close interhelical distances.<sup>51,52,123,124</sup> We fit the osmotic pressure  $\Pi$  versus the interhelical spacing  $D_{int}$  curves to a double-exponential equation with variable attractive and repulsive pre-exponential factors  $A$  and  $R$ :

$$\Pi(D) = \Pi_R(D) + \Pi_A(D) = Re^{-2D/\lambda} + Ae^{-D/\lambda} \quad (5.1)$$

with the long-range decay length  $\lambda$  fixed at 5 Å. This form and decay length constraint are the results of prior experiments that combined with osmotic stress measurements with magnetic tweezing experiments to independently evaluate the attractive and repulsive contributions to the free energies at equilibrium for several common cationic condensing agents.<sup>124</sup>

Equation (5.1) with  $\lambda = 5.0$  Å has been used previously and gives very good fits for a variety of condensing agents including G0- and G1-PAMAM dendrimer.<sup>51,52,122,127</sup> Results are only slightly dependent on the decay length  $\lambda$  over the range of  $\pm 0.5$  Å. For condensed DNA systems, the coefficient  $A$  and  $R$  are connected through the interhelical equilibrium distance,  $D_{eq}$ , since  $\Pi(D_{eq}) = 0$ , resulting in a fitting equation with only a single variable,  $R$ .

$$\log(\Pi(D)) = \log(R) - \frac{2D}{2.303\lambda} + \log(1 - e^{-(D_{eq}-D)/\lambda}) \quad (5.2)$$

With hexagonal packing of DNA, the repulsive and attractive free energy contributions per DNA base pair can be calculated at any spacing  $D$  by integrating  $\Pi dV$  for each exponential from  $\infty$  to  $D$  as

$$\frac{\Delta G_R(D)}{kT} = \frac{\sqrt{3}b(\lambda/2)(D+\lambda/2)}{kT} \Pi_R(D) \quad (5.3)$$

and

$$\frac{\Delta G_A(D)}{kT} = \frac{\sqrt{3}b\lambda(D+\lambda)}{kT} \Pi_A(D) \quad (5.4)$$

where  $b$ , the linear spacing between DNA base pairs, is  $3.4 \text{ \AA}$ .

### 5.3 Results

pH plays an important role for both G0 and G1 PAMAM when they condense DNA. The equilibrium spacings get tighter when DNA was condensed by PAMAM at lower pH. From previously study, we observed that changing pH at condensation has significantly larger effects on equilibrium spacings than changing pH after the PAMAM-DNA complexes formation.<sup>122</sup> For all the samples studied in this project, both PAMAM and DNA stock solutions were separately dissolved into 10 mM buffer solutions with appropriate pH. Then the stock solutions were titrated with

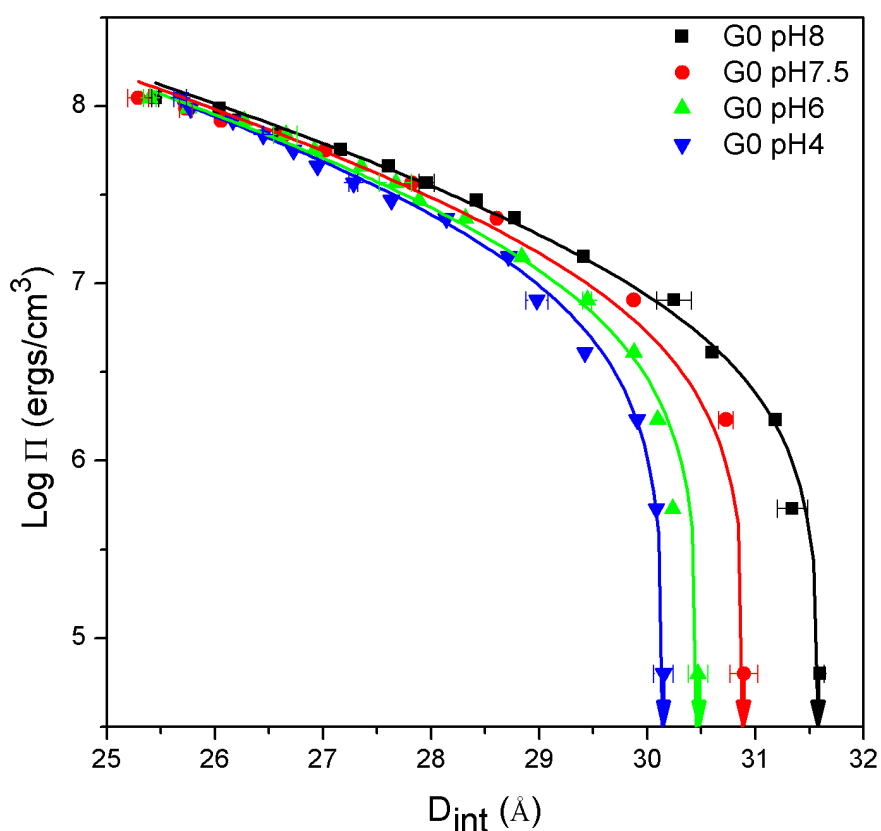


**Figure 5.1** Osmotic stress force curves are shown for G0-PAMAM/DNA as a function of pH at condensation. DNA and dendrimer were mixed and maintained at the pH indicated. Arrows indicate the equilibrium spacing in the absence of applied osmotic pressure. Solid lines are fits of the data to eqn(5.2) with  $\lambda=5 \text{ \AA}$ .

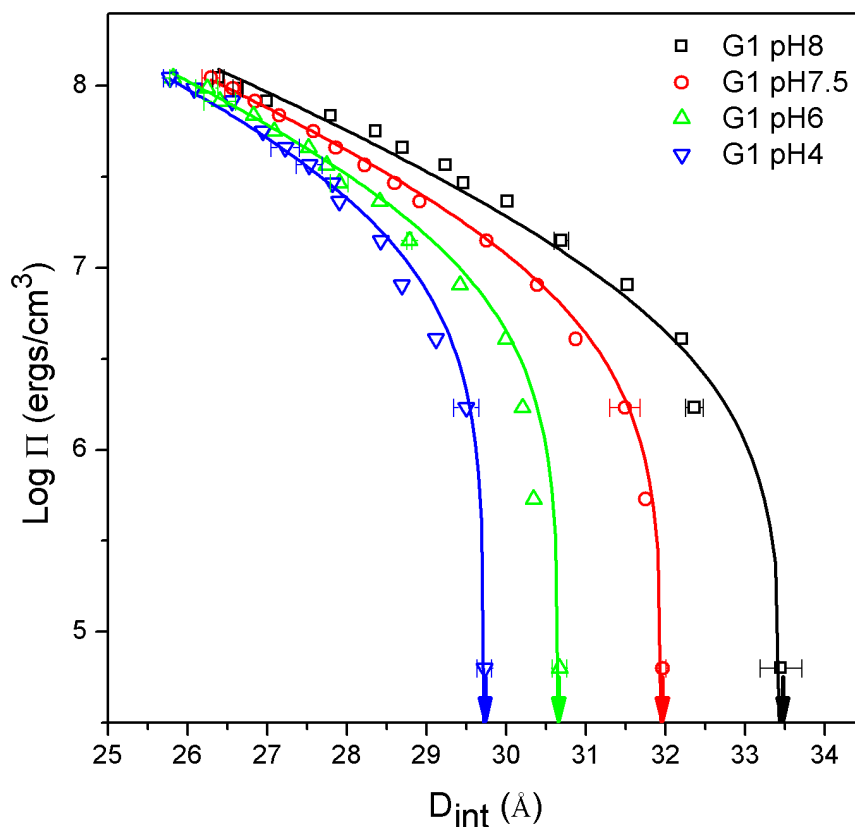


**Figure 5.2** Osmotic stress force curves are shown for G1-PAMAM/DNA as a function of pH at condensation. DNA and dendrimer were mixed and maintained at the pH indicated. Arrows indicate the equilibrium spacing in the absence of applied osmotic pressure. Solid lines are fits of the data to eqn(5.2) with  $\lambda=5$  Å.

concentrated HCl and NaOH solutions to the final desired pH. After that, DNA in desired pH was mixed with PAMAM at the same pH to form PAMAM-DNA complexes. The PAMAM-DNA complexes were stabled in the same pH buffer solution with slightly excess of PAMAM for two weeks before measured by X-rays.

To investigate the pH effects on energies and intermolecular forces which lead DNA condensed by low generation PAMAM, osmotic stress experiments coupled with small angle X-ray scattering (SAXS) were used in this study. Figure 5.1 and Figure 5.2 show osmotic stress curves for G0- and G1-PAMAM as a function of pH at condensation respectively. These figures are plotted log osmotic pressure value ( $\Pi$ ) verse the equilibrium interaxial spacing ( $D_{int}$ ) between DNA helices. The arrows in

the figures indicate the equilibrium spacings for the PAMAM-DNA complexes in the absent of applied osmotic pressure. All the curves were well described by the double exponential formulas described above. The solid lines are fitting lines to Equation (5.2) with a decay length fixed ( $\lambda$ ) at 5 Å. These fitting lines allow us to separate the net energy into repulsive and attractive contributions for free energy.

Cation	pH	$D_{eq}$ (Å)	$\Pi_R(25\text{Å})$ ( $10^8 \text{ erg cm}^{-3}$ )	$\Pi_A(25\text{Å})$ ( $10^8 \text{ erg cm}^{-3}$ )	$\Delta G_R(25\text{Å})$	$-\Delta G_A(25\text{Å})$
					kT per base pair	kT per base pair
<b>G0</b>	4	30.1	2.30	0.82	2.27	1.76
	6	30.5	2.25	0.75	2.22	1.61
<b>PAMAM</b>	7.5	30.9	2.29	0.70	2.26	1.50
	8	31.6	2.32	0.62	2.29	1.33
<b>G1</b>	4	29.7	2.72	1.06	2.69	2.28
	6	30.7	2.61	0.84	2.58	1.81
<b>PAMAM</b>	7.5	32.0	2.67	0.66	2.64	1.42
	8	33.5	2.83	0.52	2.79	1.11

**Table 5.1** The equilibrium interhelical spacings ( $\pm 0.1$  Å) from x-ray measurements and repulsive and attractive force component contributions to osmotic pressures and free energies ( $\pm 5\%$ ) for G0 and G1 PAMAM condensed DNA at different pHs. All values are calculated from fits to force curves and shown for 25 Å separations or 5 Å between DNA helices.

At all pH values studied here, DNA can be condensed by both G0- and G1 PAMAM into a hexagonal packaging spontaneously at equilibrium (i.e.  $\Pi = 0$ ). At equilibrium, we see that the equilibrium interhelical spacings ( $D_{eq}$ ) are pH-dependent for both G0- and G1-PAMAM. And the tightest packaging was observed at low pH. The equilibrium spacing for G0-PAMAM condensed DNA changes from 30.1 to 31.6 Å ( $\pm 0.1$  Å) from pH4 to pH8 as showed in Table 5.1. G1-PAMAM molecules have

more primary and tertiary amines than G0. The net charges for G1 are quite different in the pH range we studied. So there is a larger difference of  $D_{int}$  for G1, from 29.7 to 33.5 Å ( $\pm 0.1$  Å), than for G0 over the same pH range studied here.

In Table 5.1, it also shows the pH-dependent osmotic pressure contributions,  $\Pi_R$  and  $\Pi_A$ , and the repulsive and attractive free energy distribution,  $\Delta G_R$  and  $\Delta G_A$ , which were calculated from the osmotic stress curve fits and evaluated at 25 Å interhelical spacing or equivalently to 5 Å water layer separating DNA helices. From the table, we can continuously see that  $D_{eq}$  decreases as the pH decrease. The smaller  $D_{eq}$  at the absent of applied pressure means the higher the package density. This increase packaging density could be due to the decreasing of repulsive force or/and increasing of attractive force with the pH decreasing at condensation. Free energy contributions for both G0- and G1-PAMAM condensed DNA system shows that the repulsive energy distribution is pH independent while the attractive energy distribution is highly sensitive to the pH change, and the largest values were measured at the low pH. Lastly, we also show the pH dependence of the net  $\Delta G$  per base pair in Table 5.1. The expression for  $\Delta G_{NET}$  is  $\Delta G_{NET} = -(\Delta G_A(D_{eq}) + \Delta G_R(D_{eq}))$ . The calculated  $\Delta G_{NET}$  is quite small ( $< 0.6$  kT/DNA bp), which consists with the experimentally measured results from magnetic tweezing experiment of DNA condensed by multivalent cations.<sup>124</sup>

PAMAM dendrimers have both primary and tertiary amine groups with different pKa values, so this results in a pH-dependent protonation states. For G0-PAMAM there are 4 primary amines and 2 tertiary amines while for G1-PAMAM there are 8 primary amines and 6 tertiary amines. At neutral pH, the tertiary amines almost have no charges at all, but the primary amines are completely protonated. So at neutral pH, the positive charges carried by G0- and G1-PAMAM are +4 and +8 respectively. Lowering the pH value further will increase the charges carried by PAMAM, because of the protonation of tertiary amine groups. Using the protonation degree estimated of Cakara et al.<sup>101</sup>, we calculated to first approximation the nominal net charges carried

by G0-PAMAM is approximately from +3.5 to +5.1, and G1-PAMAM is approximately from +7 to +13 over the range of pH 8 to pH 4. Figure 5.3 shows the measured repulsive and attractive free energy distributions depend on the inverse value of the estimated net charges carried by PAMAM dendrimers,  $N$ . The repulsive free energies for G1-PAMAM/DNA system are measured to be 18% greater than G0-PAMAM/DNA over the pH range studied here. However, for both of the PAMAM/DNA systems, there is only a slight variation ( $< 4\%$ ) for the magnitude of repulsive free energy distribution as a function of the dendrimer net charge,  $N$ . In contrast, the attractive free energy distribution varies greatly with changing of  $N$ . For both G0- and G1-PAMAM condensed DNA systems, the scales of  $\Delta G_A$  has a linear relationship with the inverse of the estimated net charge of dendrimer,  $N$ . This  $1/N$

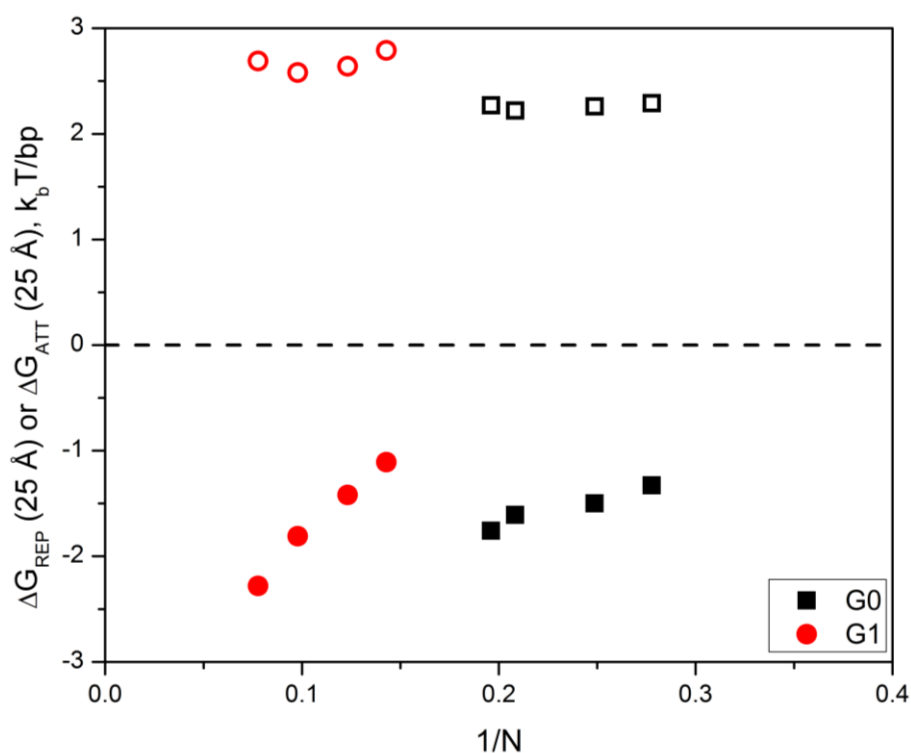


**Figure 5.3** Dependence of the free energy contributions,  $\Delta G_R$  (open) and  $\Delta G_A$  (filled), evaluated at 25 Å for G0- and G1-PAMAM condensed DNA as a function of the inverse net charge,  $N$ , of the PAMAM estimated for the various pH's used in this study.

behavior in attractions is consistent with the attractions measured in homogenous linear cation condensed DNA systems in previously study, such as alkylamines, lysines and arginines.<sup>51,52</sup>

Figure 5.4 is a summary of observed changed of Bragg spacings ( $D_{Br}$ ) for G0- and G1-PAMAM complexes with the increase concentration of added NaCl salt. The complexes were condensed at pH 4-pH 8 respectively. We plotted the dependence of Bragg scattering here in case to avoid the complications which brought by the possible phase transition happened in the DNA complexes with the increasing of salt concentration. Figure 5.4A and 5.4B show the DNA Bragg spacings for G0- and G1-PAMAM/DNA complexes as a function of NaCl salt concentration. Figure 5.4C and 5.4D show the absolute change of Bragg spacings compared to the Bragg spacing ( $D_{Br} - D_{Br,eq}$ ) without addition NaCl for G0- and G1-PAMAM/DNA complexes respectively. From the figures, we can see that at all pHs, for both G0- and G1-PAMAM condensed DNA systems, the Bragg spacings swell up with the increasing of NaCl concentration. The swelling behavior of Bragg spacings is not only highly depended on the dendrimer used but also the pH at condensation. Where the Bragg scattering is observed, the observed changing of Bragg spacings have two regimes with two different slopes, or rates of swelling, with added salt. We define a critical concentration,  $c^*$ , as the salt concentration where the two slopes cross together. For G0-PAMAM/DNA systems, the  $c^*$  was observed changing from  $\sim 75$  mM NaCl when DNA condensed at pH 8 to 150 mM NaCl when condensed at pH 4. Similarly, for G1 PAMAM/DNA complexes,  $c^*$  changed from 200 mM NaCl to nearly 460 mM over the same pH range. At higher salt concentration, the Bragg scatterings are completely lost for the samples and no reflections are observed.

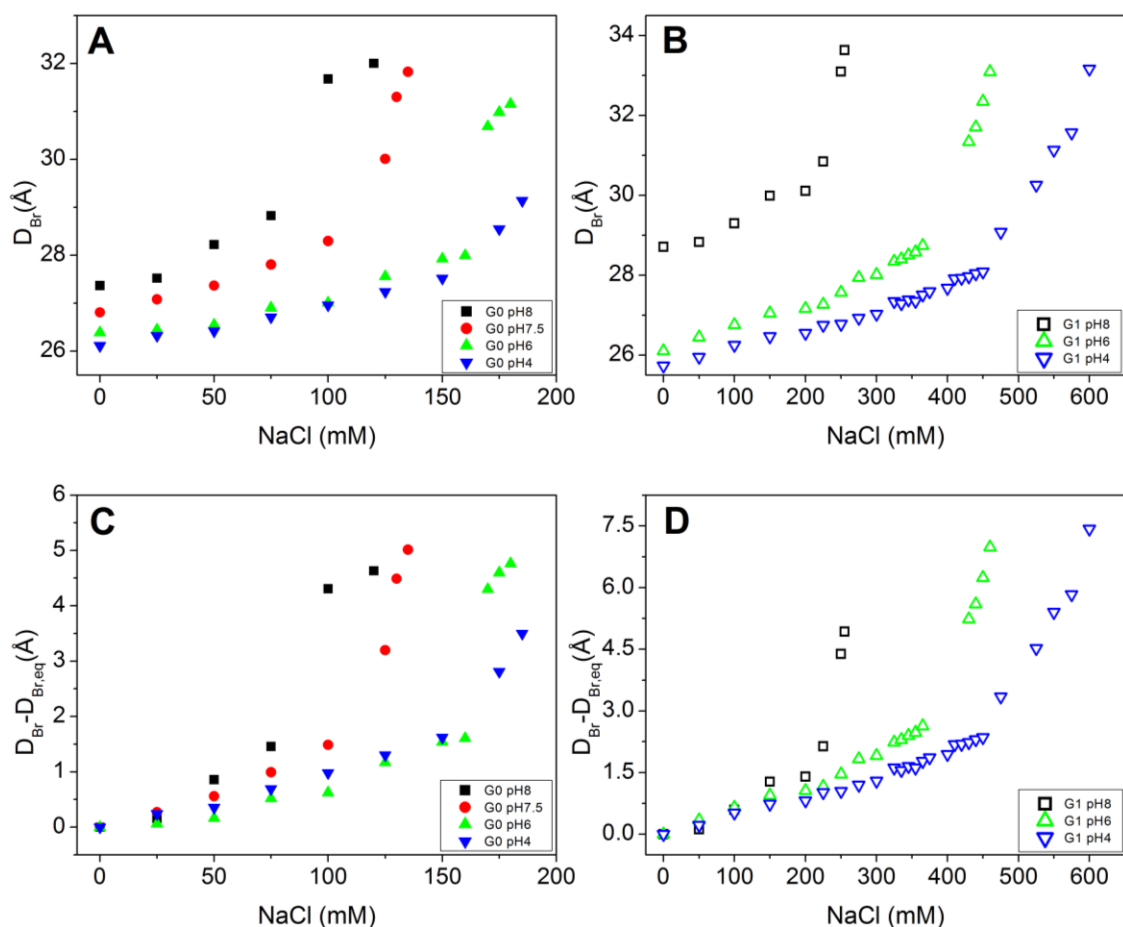


**Figure 5.4** (A) Bragg spacing dependence as a function of added NaCl concentration for G0-DNA and (B) G1-DNA condensed systems at different pHs. (C) and (D) plot the change in the Bragg spacing relative to  $D_{Br}$  in 10 mM monovalent buffer without added salt ( $D_{Br,eq}$ ). The equilibrium solutions show no Bragg scattering at the next higher salt concentration in each series.

At salt concentration below  $c^*$ , the Bragg reflection for G1-PAMAM/DNA complexes is observed to shift to lower  $Q$ , or equivalent to a larger DNA-DNA spacing, but the peak shape was maintained with added salt. In contrast, we observe significant peak broadening at salt concentration at  $c^*$  or higher than  $c^*$ . In Figure 5.5, we show this peak broadening behavior for G1-PAMAM/DNA complexes condensed at two different pHs under high salt concentration. Here we plotted normalized SAXS scattering density ( $I/I_{max}$ ) as a function of the scattering vector  $Q$  for G1-PAMAM/DNA complexes condensed at pH 4 and pH 8 under both low and high

added salt concentrations. For G1-PAMAM/DNA condensed at pH 4, we plot 0 and 525 mM added NaCl salt. For G1 complexes condensed at pH8, we plot 0 and 250 mM added NaCl, where 250 mM NaCl is already above the  $c^*$ . When above  $c^*$ , the Bragg reflection peak simultaneously shifts to a lower  $Q$  and broadened with added salt as we observed here. Equivalent results are also seen for the G0-PAMAM/DNA complexes. (Not shown here.)

Figure 5.6 shows that we can manipulate the salt dependent phase behavior for G1-PAMAM/DNA complexes, which are condensed at different pHs studied here, into one single line. Here plotted the relative change of the Bragg spacing ( $D_{Br}/D_{Br,eq}$ ) as a function of the added salt concentration normalized by the critical salt concentration,  $c^*$ , for each pH/cation system ( $c/c^*$ ). Here,  $D_{Br,eq}$  is the equilibrium Bragg spacing for dendriplexes without added NaCl salt. The slopes at all pHs for G1-PAMAM/DNA complexes are quite similar in both regimes, above or below  $c^*$ . As we discussed above, the scattering profile shows significant peak width broaden when the added salt concentration at or above  $c^*$ . To quantify the peak broadening, in Figure 5.6B we plotted the average in-plane correlation lengths,  $\xi$ , as a function of  $c/c^*$ .  $\xi$  was calculated from the full width at half-maximum of the observed Bragg scattering peak, as  $\xi = 2\pi/\Delta Q_{Br}$ .

This correlation length reflected the in-plane, long range ordering of DNA helices in the system. Below  $c^*$ , though there is a little variations of  $\xi$  between samples, the correlation length remains fairly consistent and independent of pH. The typical value for  $\xi$  is a number between 220-300 Å when the salt concentration below  $c^*$  and there is no significant variations of  $\xi$  with the added salt concentration increasing. However, at or above critical concentration, we see a dramatic decrease of the correlation length for G1-PAMAM/DNA complexes at all three pHs, and the correlation length decreases continuously with the increasing of added salt concentration. Eventually, sufficient salt is added that no further Bragg scattering was

observed. The last regime was reflected that there was an isotropic web formed by DNA and PAMAM or the sample was totally dissolved.

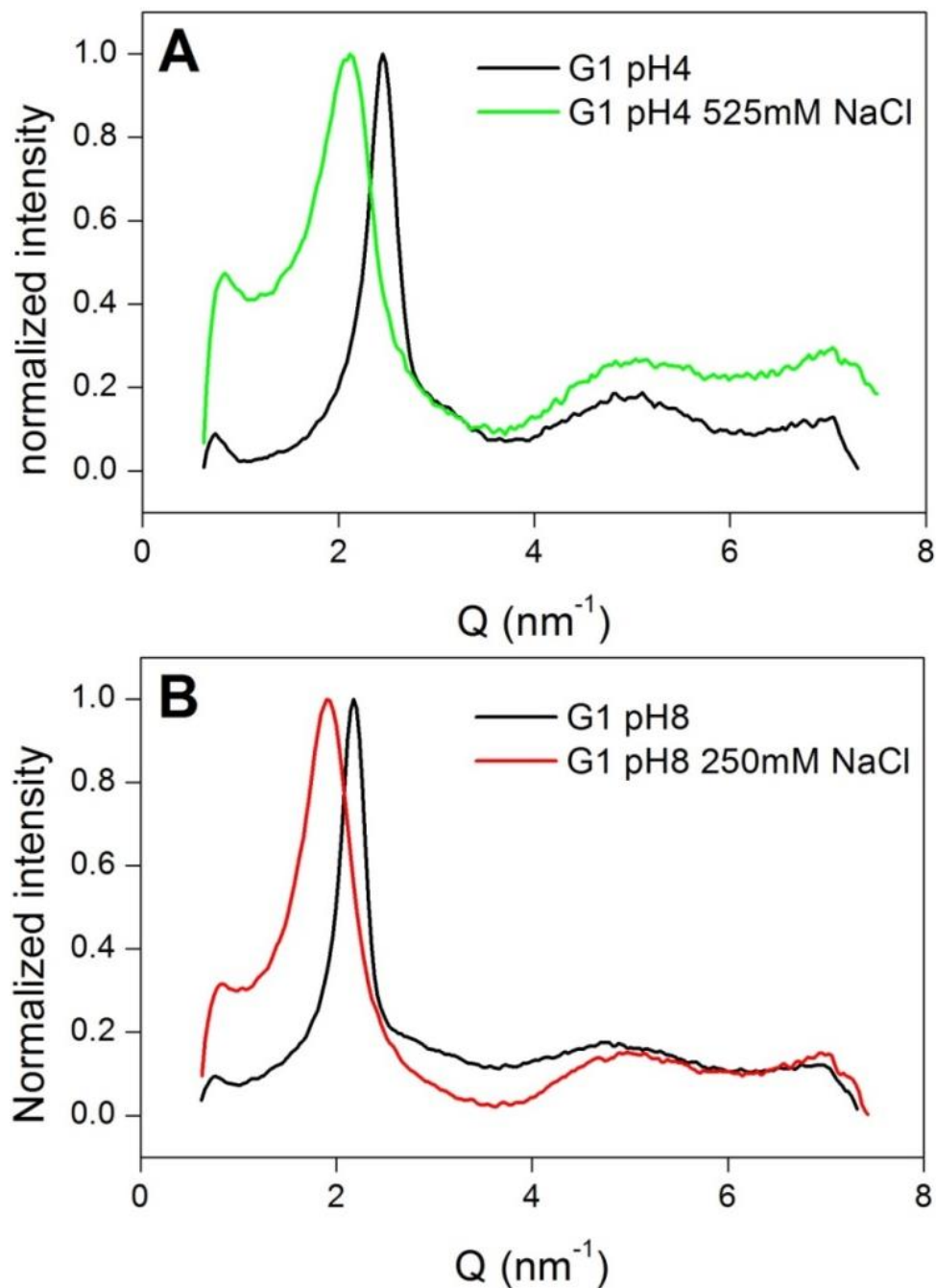


**Figure 5.5** Scattering profiles for G1-DNA assemblies at (A) pH 4 and (B) pH 8 for both low salt and high salt conditions. Shown is the normalized intensity ( $I/I_{max}$ ) as a function of scattering vector  $Q$ .

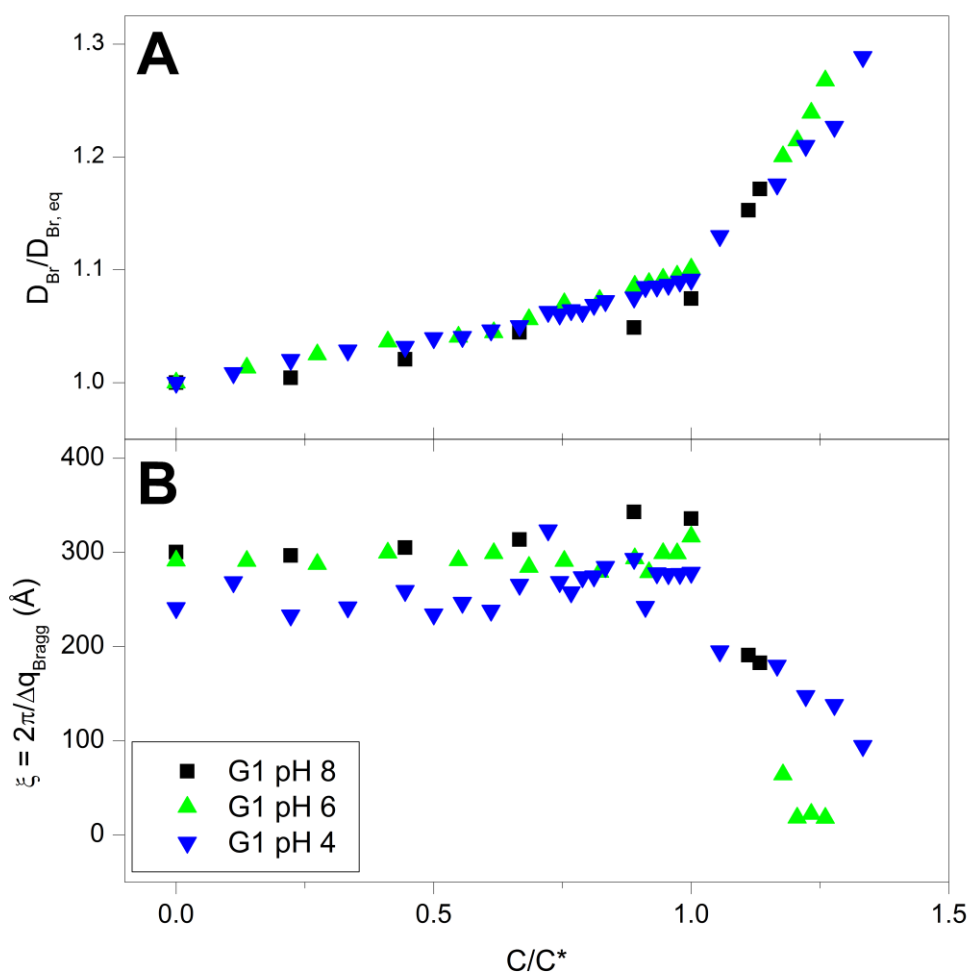


**Figure 5.6** (A) Normalized  $D_{Br}$  spacing and (B) in-plane correlation lengths,  $\xi = 2\pi/\Delta Q_{Br}$ , for DNA condensed with G1-PAMAM at different pH as a function of the salt concentration normalized by the critical salt concentration for each system ( $c/c^*$ ). A discontinuous phase transition occurs at  $c^*$  where both the salt sensitivity and the long-range order of the PAMAM/DNA condensed phase are significantly altered.

#### 5.4 Discussion

In vitro condensation of high molecular weight DNA by a variety of multivalent cations has been studied extensively. Spontaneous packaging of DNA into hexagonal arrays typically occurs in the presence of cations with net charge of +3 or higher.<sup>20,21</sup> DNA helices in these packaged arrays do not touch but are separated by  $\sim 5\text{--}15$  Å of

water, equivalent to a few monolayers of water.<sup>128</sup> This water present is indicative of a balancing of attractive and repulsive thermodynamic forces within the condensed cation/DNA phase. In the presence of condensing cations, there is a substantial reduction of the repulsive electrostatic interaction between DNA helices. This reduction, however, does not by itself account for the attractive interaction measured, indicating DNA condensation requires more than just counterion condensation.<sup>20</sup> Most current theoretical models therefore require correlation of charges or water structures between DNA helices to account for the magnitude of the experimentally determined attractions stabilizing condensed DNA.<sup>23,24,107,128,129</sup> A convenient means to accomplish such correlations is to presume that cation binding occurs in one of the grooves of the DNA helix, thus coordinating charges, or restructuring the water molecules, along these interfaces. In this model, cations bind in grooves and allow the bound positive charges on one DNA to correlate to negative phosphate backbones on an apposing DNA molecule. Some experimental results suggest that linear cations do indeed bind in the grooves of DNA though it is not clear if this binding is in the major, minor, or both grooves.<sup>90,102-105</sup>

Hyperbranched molecules, such as dendrimers, present a significant problem for such groove binding models. Even for low generations, the size of the dendrimer already approach or exceed the dimensions of even the major groove of DNA. The major groove in B-DNA is approximately 8.5 Å deep and 12 Å wide. In comparison, the diameter of G0-PAMAM molecule has a diameter of ~15 Å, while the G1-PAMAM has a diameter of 22 Å. We would anticipate therefore that PAMAM is not likely capable of coordinating in DNA grooves in the same manner as has been proposed for linear cations. Recently, using osmotic force measurements, we showed that low generation PAMAM dendrimers condense DNA in hexagonally packaged arrays, but their dependence on cation charge at near neutral pH is completely different than comparably charged linear cations.<sup>122</sup> We proposed the differences are likely due to that PAMAM using other binding modes, such as cation bridging

between DNA double helices, to condense DNA as has been proposed by others theoretically and experimentally.<sup>63,70,97</sup>

In this chapter, we are interested in understanding the effect of pH on the intermolecular forces in DNA condensed by low generation PAMAM and the resulting phase behavior and salt stabilities of the complexes. Our earlier experiments showed that condensing DNA with PAMAM at a specific pH alters DNA packaging more strongly than changing the pH after dendriplex formation.<sup>122</sup> These results most likely suggest that the  $pK_a$ s of the PAMAM amines, once bound, are shifted and their ability to protonate or deprotonate are different than unbound PAMAM in solution. To keep samples as uniform as possible, we have made all the samples here by first pH buffering the DNA and the dendrimer separately and then mixing the solutions to condense at the desired pH. After condensation, samples were maintained at the same pH with 10mM buffer solutions.

The ability for G0- and G1-PAMAM to spontaneously condense DNA at all pHs in our experiments is consistent with the net valency exceeding +3 in all the samples. As discussed in the Result section, G0 is estimated to be +3.5 to +5.1 and G1 is estimated to be +7 to +13 over the pH range of 8 to 4. At equilibrium (i.e.  $\Pi = 0$ ), we see a pH-dependent interaxial spacing ( $D_{eq}$ ) for both PAMAM/DNA systems. As DNA has a 2 nm diameter, these interaxial spacings indicate  $\sim 10.1\text{--}11.6$  Å of water for G0-PAMAM/DNA system, and  $\sim 9.7\text{--}13.5$  Å of water between helices in G1-PAMAM/DNA depending on pH. All these spacings are smaller than the G0- and G1-PAMAM molecule diameters in solution. While larger generation dendrimers are thought have spherical shapes, low generation dendrimers are believed to be more disk-like in shape.<sup>130</sup> This molecule shape may allow G0 and G1 to condense DNA to spacings smaller than the PAMAM diameters.

We previously showed that homologous linear cations, such as alkylamines, arginines, or lysines, converge at high osmotic pressure to the same repulsive limit regardless of cation length or charge for a given cation species.<sup>51,52</sup> The magnitude of

the repulsions however changed with the cation chemistry. The attractions in all these linear cation systems are shown to have a very similar  $\sim 1/N$  dependence, where  $N$  is the charge of polycations. We argued the  $1/N$  dependence likely arises from translational entropy of the bound cations where, for example, there is less loss of entropy in correlating one +3 counterion than three +1 ions. Although the chemistries of G0- and G1-PAMAM are essentially identical, we observe here by force measurements that at near neutral pH the different PAMAM/DNA complexes do not converge to the same repulsive limit. If we compare the data for pH 7.5 given in Table 5.1, the measured attractions for the two PAMAM generations are nearly identical despite G1-PAMAM being +8 and G0-PAMAM is being +4 at this pH. Repulsions, however, are larger for G1-PAMAM/DNA. Combined, these forces result in G1-PAMAM/DNA being more loosely packaged than G0-PAMAM/DNA at neutral pH despite being more highly charged—directly opposite to what is observed for homologous linear cations.

Focusing on the effect of pH on the forces, we see that for a given dendriplex system, despite starting at very different interaxial spacings at equilibrium, both G0- and G1-PAMAM condensed DNA converge to the same high pressure limit for all pHs studied as shown in Figures 5.1 and 5.2. This convergence is better in G0-PAMAM/DNA than in G1-PAMAM/DNA complexes, perhaps reflecting increased steric effects in the larger generation dendrimer. Using the estimates of residual net charge, we can also determine the dependence of the attractive and repulsive free energy contributions for the PAMAM dendriplexes as a function of the inverse dendrimer charge  $N$  (Figure 5.3). For both dendriplex systems, the respective  $\Delta G_R$  are relatively insensitive to pH and show little dependence (<4%) on dendrimer charge. The magnitude of the short-range repulsive force in DNA condensed by G1-PAMAM is seen to be  $\sim 15\%$  higher than G0-PAMAM at all pHs. In contrast, the attractions vary significantly with the inverse charge of the dendrimer, comparable to attractions observed for linear DNA condensing agents. Over the pH range of 8 to 4,  $\Delta G_A$  values are seen to increase  $\sim 24\%$  for G0-PAMAM and  $\sim 50\%$  for G1-PAMAM.

Surprisingly, the magnitudes of the attractions are quite similar for G0 and G1 over pH 6 to 8 despite large differences in the net charge of the two dendrimers. Ultimately, G1-PAMAM does have a greater change in the attractions, and we observe that at pH 4 the increased attractions allow G1-PAMAM for the first time to condense DNA more tightly than G0-PAMAM at the same pH. It is interesting to note that extrapolating the force data suggests that, while trivalent or higher is typically sufficient to condense DNA, an approximately +5 G1-PAMAM would not be able to condense DNA primarily due to the weak attractions of the hyperbranched dendrimer compared to similarly charged linear or inorganic cations. How exactly the dendrimer molecules are arranged within the condensed phase still remains to be determined.

The salt dependence of the DNA–DNA spacings without applied pressure was also determined for G0- and G1-PAMAM dendriplexes condensed at different pHs (Figure 5.4). For all systems, added NaCl salt causes the DNA packaging to swell, resulting in larger spacings. We previously observed that salt dependencies in protamine–DNA are highly dependent on the salt species, not just charge.<sup>54</sup> Added salt does not simply screen electrostatic attractions in the cation condensed DNA phase but acts through some complicated combination of electrostatic screening, anion binding to the bound cation, and/or cation competition with the bound cation for DNA binding. Here, for PAMAM condensed DNA, we see large changes in the DNA–DNA spacings increasing as much as 7.5 Å for G1-PAMAM/DNA with added NaCl salt (Figure 5.4 D). There are also two unique salt regimes observed for both PAMAM/DNA systems. At low salt, with DNA packaged tightly in a hexagonal array, we observe a slow swelling regime. Then at a specific critical salt concentration,  $c^*$ , a phase transition occurs, and a much faster rate of swelling is observed with additional added salt. Both the rate of swelling and  $c^*$  magnitude depend on the PAMAM generation number and the pH at condensation. Significantly higher NaCl concentration is needed to induce the discontinuous phase transition with PAMAM/DNA condensed at low pH compared to high pH. Also, the more highly

charged G1-PAMAM/DNA results in higher  $c^*$  for all pHs compared to G0-PAMAM/DNA.

Scattering profiles before and after  $c^*$  are consistent with the salt-induced melting transition (Figure 5.5). Below  $c^*$ , sharp Bragg reflections are observed to maintain their sharpness but shift to lower  $Q$ , or equivalently larger DNA–DNA spacings, with added salt. At  $c^*$ , the observed Bragg reflections are significantly broader. Above  $c^*$ , these broad reflections simultaneously shift to lower  $Q$  and broaden with further added salt. These results suggest a discontinuous phase transition occurring at  $c^*$  from a tightly packaged hexagonal DNA array at low salt to a more loosely organized, fluctuation dominated phase above  $c^*$ —most likely a cholesteric liquid crystalline phase. The cholesteric phase of DNA observed at high salt is characterized by increased positional disorder and greater sensitivity to configuration fluctuations with added salt. Eventually, enough salt is added to disrupt DNA order sufficiently that all Bragg scattering is lost. Because of the relatively high concentration of DNA and cation in our X-ray samples, this likely is an isotropic network phase of PAMAM and DNA chains forming at high salt. Similar salt-dependent phase transitions were observed for linear cation/DNA complexes including polylysine, polyarginine, and spermidine.<sup>76,131</sup> For the linear cations, the critical salt concentrations were highly dependent on the nature of the cation used to condense DNA. In our study, the chemical makeup of our two PAMAM systems are nearly identical; thus, the observed differences in  $c^*$  are most likely resulting from differences in the net charge of the dendrimer and the ability of the monovalent salt to compete with the polyvalent PAMAM molecules. The hexagonal–cholesteric transition, however, is likely a complicated combination of chain configurational entropy and ion binding competition that is not easily understood. Recently, similar phase transitions between a square, a hexagonal, and a “bead on a string” phase were reported for G4-PAMAM/DNA as a function of the charge ratio of amines to phosphates and the degree of protonation (dp).<sup>28</sup> In these samples, dp was adjusted after complex formation by addition of concentrated acid or base.

Lastly, we show that we can collapse all of the G1-PAMAM/ DNA salt data to a single curve by plotting the relative increase in Bragg spacing ( $D_{Br}/D_{Br,eq}$ ) as a function of the salt concentration normalized by the critical salt concentration ( $c/c^*$ ) for each pH/salt system. Similar results are seen with G0-PAMAM/DNA (not shown). This universal behavior suggests that there is a common physical origin for the observed discontinuous phase transition that is independent of pH for a given PAMAM/DNA system. Despite each G1-PAMAM/DNA starting from its own unique pH-dependent packaging state without added salt, we unexpectedly see all three pH samples swell  $\sim 10\%$  from their original Bragg spacing before reaching the salt-induced melting transition at  $c^*$  to a more loosely ordered array. Once above  $c^*$ , G1-PAMAM condensed at pH8 swells an additional 20%, while G1-PAMAM dendriplexes condensed at pH 4 and 6 swell approximately 30% more before Bragg reflections are lost. The average in-plane correlation lengths,  $\xi$ , also change dramatically at  $c^*$ . Below  $c^*$ , G1-PAMAM has correlation lengths  $\xi$  of  $\sim 220\text{--}300 \text{ \AA}$  (or approximately 7–10 DNA repeats) for all three pHs. Near  $c^*$  we observed  $\xi$  quickly drops to just a few DNA repeats for all the samples. Once in the fluctuation dominated cholesteric phase, the PAMAM/DNA is increasingly sensitive to monovalent salt and the complex opens up quickly, becoming highly disordered until all Bragg scattering is lost.

## 5.5 Conclusion

In this paper, we describe the role of pH on the packaging, compaction energies, and phase behavior for DNA condensed by low generation PAMAM dendrimers. At equilibrium, in low salt conditions, all samples are consistent with DNA being locally hexagonally packaged by the PAMAM dendrimers. Using osmotic pressure, we directly measured the intermolecular forces in G0- and G1-PAMAM/DNA condensate as a function of pH at condensation. By separating the repulsive and quantifying the attractive and repulsive free energy contributions, we show that repulsions for a given PAMAM generation are nearly unaffected by pH while the

observed attractions scale approximately linearly with the inverse of the dendrimer charge. Changes in pH at condensation also greatly influence the resulting phase behavior for PAMAM dendriplexes. For all systems, a hexagonal to cholesteric phase transition is observed with the addition of monovalent salt. The critical salt concentration,  $c^*$ , required to induce this melting transition is observed to be dependent on both PAMAM generation number and the pH at condensation. Together, our results suggest that pH and salt play a central role in tuning the intermolecular forces and packaging within the PAMAM/DNA condensed phase. The ability to manipulate these forces is essential for therapeutic uses of PAMAM, such as successful gene delivery.

## Chapter 6 Packaging of DNA by G4 PAMAM and Zwitterionic G4 PAMAM

### 6.1 Introduction

Poly(amidoamine) (PAMAM) dendrimers are highly symmetrical branched molecules with precisely defined size and molecular weight.<sup>2,132,133</sup> Due to its ability to condense DNA and protect it from damage by nuclease enzymes, PAMAM has been studied for its potential as a non-viral gene vector.<sup>60,134,135</sup> PAMAM was one of the first commercially available dendrimers and is thus one of the most widely studied vectors for the delivery of drugs and genes.<sup>136-140</sup> However, the development of PAMAM, and most polycations, for gene delivery is hindered by cytotoxicity in many cell lines and tissues.

For efficient transfection, PAMAM-DNA dendriplexes are usually mixed at high nitrogen-to-phosphate (N/P) charge ratios resulting in effective colloidal particles (typically < 150 nm in diameter). Excess PAMAM is also required for the formation of sufficiently small, stable nanoparticles for efficient cellular uptake. PAMAM-DNA nanoparticles have a highly positive surface charge limiting their use for *in vivo* applications because of undesired, unspecific interactions with blood components, proteins, or non-target cells. To reduce these unspecific interactions, most studies have tried two methods with various degrees of success: (i) the incorporation of uncharged hydrophilic polymers, typically poly(ethylene glycol) (PEG),<sup>141-143</sup> to shield polyplexes or (ii) incorporation of a polyanion to form a ternary complex of nucleic acid, polycation and polyanion.<sup>144-146</sup> These methods have proven effective to lower particle surface charge, increase stability in the presence of salt, and reduce interactions with blood components, thus increasing the particle suitability for *in vivo* application. Incorporation of polyanions has also been proposed to loosen the complex and facilitate unpackaging thus improving transfection efficiency over PAMAM/DNA alone.

The large excess of unbound PAMAM is also problematic as free polycations are also known to be toxic to cells.<sup>147,148</sup> Recent work has suggested that cell interactions with the polycation play a critical role in controlling transfection efficiency.<sup>149,150</sup> Using fluorescence correlation spectroscopy, DeRouchey has previously shown that in at least one PEGylated ternary system that only a small fraction of the polyanion is actually binding to the polyplex.<sup>151</sup> A significant fraction of the polyanion is involved in making “ghost particles” by binding up the loose polycations. The reduction in free polycations leads to significantly reduced toxicities, which plays an important role in increased transfection. More recently, approaches that reduce the net charge of PEI-DNA polyplexes, such as acetylation of polyethylenimine (PEI) primary amines or incorporation of charge-shifting side chains, have been explored by Dr. Dan Pack and others to control packaging/release from complexes while minimizing cytotoxicity.<sup>152-154</sup> This approach was recently extended to acetylated PAMAM also showing improved transfection over unmodified PAMAM/DNA.<sup>144,146,155</sup>

In an attempt to improve PAMAM transfections, we proposed the synthesis of modified PAMAM dendrimers by reaction with succinic anhydride, which will reduce the number of primary amines and introduce negatively charged carboxylate moieties. In this manner, we generate a series of these zwitterionic PAMAMs (zPAMAM) that will allow for a systematic tuning of polymer-DNA interactions. Previous work by the DeRouchey lab has shown that zwitterionic linear polymers (phosphorylated protamines) are surprisingly capable of condensing DNA. Our hypothesis is that zwitterionic PAMAM will provide the ability to tune polymer-DNA interactions leading to polyplexes with enhanced intracellular unpackaging and more efficient gene delivery. We also hypothesize zPAMAM will result in polymer carriers with reduced cellular toxicity. As a first step to this study, zPAMAM with varying degrees of modification were synthesized by the group of Dr. Vincent Rotello of the University of Massachusetts Amherst and kindly provided to us. In our study, we will focus on 15%, 24%, 40% and 100% modified z-PAMAM all synthesized from commercially available G4-PAMAM. The goals of this chapter are to investigate

DNA condensation by zPAMAM and compare the resulting structures and phase behavior to unmodified PAMAM/DNA.

## **6.2 Material and Methods**

### **6.2.1 Material**

NaN<sub>3</sub>, HCl, NaOH were purchased from Sigma. 1 M Tris pH 7.5 buffer was purchased from Mediatech Inc. 50× TAE buffer was purchased from Omega Bio-tek (Norcross, GA). Heparin sodium salt from porcine intestinal mucosa was purchased from Sigma-Aldrich. PUC18 plasmid DNA was amplified by transformation and purified by plasmid extraction in our lab. High molecular weight DNA(>5×10<sup>6</sup>) was prepared and purified from adult chicken whole blood as described previously.<sup>98</sup> Deionized water was prepared with Millipore water purification system. All chemicals were used without further purification.

PAMAM dendrimers (generations 4, ethylenediamine core, and amine-terminated polyamidoamine, in 10% methanol) were purchased from Sigma-Aldrich (St Louis, MO). Modified G4-PAMAMs were synthesized in the laboratory of our collaborator (Dr. Vincent Rotello, University Massachusetts). Reactions of PAMAM with succinic anhydride were performed in 50 mM sodium bicarbonate buffer (pH 9). The anhydride reacts with the primary amines of the surface groups on PAMAM dendrimer to form carboxylic acid surface groups. Percent modification was controlled by PAMAM: Anhydride feed ratios in the reaction. NMR was used to quantify the amine/carboxylate ratios to determine the percent modification. Five zPAMAMs were used in this study: 0%, 15%, 24%, 40% and 100 % modification.

### **6.2.2 pUC18 Plasmid Transformation into E. coli**

The LB broth petri dish with penicillin (1:1000) was prepared ahead of transformation. Competent cells stored at -80 °C were removed and placed in an ice bath until required. Approximately 1 ng pUC18 plasmid DNA was added to 20 μL of

competent cells then incubated on ice for 30 min. After incubation, hot shock the cells at 42 °C for 90 seconds. After heat shock, cells were cooled down on ice for 5 min. The competent cells were then placed in 900 µL SOC broth in a Fallon tube. The cells were then incubated at 37 °C with continuous shaking for 2 hours. 100 µL of this solution was then plated onto the LB petri dish loaded with ampicillin and spread until there was no extra solution observed on the plate. We found that to increase the success of transformation it was best to always warm up the plate at 37 °C before putting the cells on it. Plates were then incubated upside down overnight at 37 °C. Only cells successfully transformed with pUC18 plasmid will grow on the plate. One colony was picked using a sterilized tip and placed into 1 mL BL broth with penicillin and incubated for ~ 8 hours. 500 mL of this cultivated bacterial solution was then added to 400 mL LB broth with penicillin and incubated with shaking overnight.

### **6.2.3 Plasmid Extraction**

pUC18 Plasmid DNA was extracted using a EZNA Plasmid DNA max kit from OMEGA bio-tek following manufacturer's protocol. In brief, cells were collected by centrifuging at 4000 g for 10 min and discarding the supernatant. Care must be taken to discard all the supernatant or the plasmid DNA quality will be low. Collected cells were resuspended in 12 mL of solution A with RNase A. 12 mL of solution B was then added and incubated for 2 min at room temperature with gentle mixing to lyse the cells. After incubation, 16 mL of solution C was added with gentle mixing to neutralize the basic solution B. The mixture was then centrifuged at maximum speed for 10 min. During this process, the plasmid of interest remains in solution while the other cell components precipitate into a white pellet. After centrifugation, the supernatant was transferred to a HiBind DNA Maxi column. Plasmid DNA binds to the column. The column was centrifuged at 4000 g for 5 min and the supernatant discarded. Wash the other cell components bonded on the column twice with 10 mL HBC buffer at maximum centrifuge speed (HBC buffer must diluted with isopropanol before use). Then the column was centrifuged at maximum speed for 10 min, and

DNA was eluted using 3 mL of deionized water. The quality and concentration of the plasmid was verified by UV-Vis.

#### **6.2.4 Gel Retardation Assay**

To determine DNA condensation efficiency by G4-PAMAM and zPAMAM, PAMAM/plasmid complexes were prepared at various amine to phosphate (N/P) charge ratios ranging from  $\sim N/P = 0$  to  $N/P = 4$ . 1  $\mu\text{g}$  of pUC18 plasmid DNA was used per sample with varying zPAMAM amounts. By mass, the cation added ranged from 0 to 2.7  $\mu\text{g}$  PAMAM, respectively. After 10 min of incubation at room temperature for complex formation, each sample was brought to the same total volume of 10  $\mu\text{L}$  by addition of DI water. 1  $\mu\text{L}$  of 10X loading buffer was then added to each sample before loading on the agarose gel for electrophoresis. The samples were electrophoresed on a 1% (w/v) agarose gel using 1X TAE buffer (40 mM Tris pH 8, 20 mM acetic acid and 1 mM EDTA) at 120 V for approximately 2 hours. After electrophoresis, the gel was stained with ethidium bromide solution (0.5  $\mu\text{g}/\text{mL}$ ) for 1 hour followed by a 30 min destaining with 1X TAE buffer. Gels were analyzed on a UV illuminator to show the location of the DNA.

#### **6.2.5 Dissociation of DNA from Complexes**

DNA stability in the PAMAM complexes was assessed using gel electrophoresis to visualize DNA release from the dendriplexes. 1  $\mu\text{g}$  pUC18 plasmid DNA was first condensed by 4  $\mu\text{g}$  PAMAM or following the protocol described in 6.2.4. 4  $\mu\text{g}$  was found to be sufficient for complete DNA condensation for all percent modifications of PAMAM except 100%. After addition of PAMAM to the DNA solution, the total volume for each sample was brought up to 10  $\mu\text{L}$  by addition of DI water and samples were incubated at room temperature for 10 min. Then varying amounts of dextran sulfate were added to the dendriplexes followed by the addition of DI water to bring all samples to final total volume of 15  $\mu\text{L}$ . The dendriplex/heparin samples were

incubated for 20 min at room temperature to allow for dissociation before loading on the agarose gel for electrophoresis.

### **6.2.6 Dynamic Light Scattering (DLS) Measurements**

The size and the size distribution of PAMAM/DNA dendriplexes was characterized by means of dynamic light scattering measurements using a Malvern Zetasizer Nano S90 instrument employing a 4 mW He–Ne laser operating at a wavelength of 532 nm and Refractive index detector. Approximately 3.75  $\mu\text{g}$  of DNA was used per sample and condensed with  $\sim 10$   $\mu\text{g}$  of G4-PAMAM or zPAMAM. This corresponds to an N/P ratio of 6 with unmodified PAMAM. After mixing the polymer with DNA in a cuvette, samples were equilibrated for 10 min to allow for equilibration before recording the spectrum. Before DLS measurement, each sample was brought to the same total sample volume of 500  $\mu\text{L}$ . Autocorrelation functions were convoluted using Zetasizer Nano software.

### **6.2.7 Sample Preparation for X-ray Analysis**

DNA dendriplexes were prepared from mixtures of purified chicken blood DNA with the desired cationic polymer. DNA-DNA spacings are generally independent of DNA molecular weight over a broad range; for example the equilibrium DNA-DNA interhelical spacing for spermine condensed DNA are in very good agreement for high molecular weight DNA,<sup>76</sup> 150 bp DNA,<sup>156</sup> and 25 bp oligonucleotides.<sup>157</sup> In addition, we previously showed DNA-DNA spacings were also equivalent for polyplexes formed by various cations condensing either linear or plasmid DNA.<sup>55</sup> In this work, we used two different methods for the preparation of PAMAM/DNA samples for analysis by X-rays: which we will refer to as ‘low’ and ‘high’ salt preparation. The low salt preparation is the same sample preparation discussed in Chapters 4 and 5. Approximately 250  $\mu\text{g}$  chicken blood (CB) DNA were used per x-ray sample. Concentrated PAMAM stock solutions were added to 1 mg/mL CB DNA in 10 mM pH buffer in a stepwise fashion. Each addition was mixed thoroughly before adding additional PAMAM, and the

process continued until all DNA was precipitated. Alternatively, in the high salt preparation, DNA and PAMAM solutions were dissolved separately in a 2 M NaCl salt solution with Tris buffer. Again ~250  $\mu\text{g}$  of DNA was used per x-ray sample. Based upon the required PAMAM to condense all the DNA observed in the low salt preparation, a sufficient amount of PAMAM or zPAMAM was added to the DNA to ensure complete condensation. The high salt concentration prevents condensation from occurring and allows thorough mixing of the dendrimer and DNA in the solution. Precipitation was subsequently induced by dilution with additional Tris buffer solution resulting in a solid fibrous condensate. This condensate was collected by centrifugation (10000 g / 10 min) and washed repeatedly with buffer to extract as much salt as possible. This high salt sample preparation was found to make stable dendriplexes that do not show significant internal structure rearrangements over several months as discussed in the results section.

Dendriplex samples used in SAXS experiments for the study of phase behavior as a function of pH and salt, were prepared as described in Chapter 5.2.2 using both the low and high salt methods. Unless otherwise stated all fibrous PAMAM–DNA samples were transferred to the desired buffered solution and allowed to equilibrate 2 weeks before X-ray analysis.

### **6.2.8 Small Angle X-ray Scattering**

Graded-multilayer focused  $\text{CuK}\alpha$  radiation from a Nonius FR-591 rotating anode fine-focus X-ray generator operating at 45 kV and 20 mA was used for the small-angle X-ray scattering experiments. The primary beam was collimated using a fine rear aperture beam tunnel. Samples were sealed with a bath of equilibrating solution in the sample cell and then mounted into a sample holder at room temperature (25  $^{\circ}\text{C}$ ). The flight path between the sample and the detector was filled with helium to minimize background scattering. Diffraction patterns were recorded with a SMART 6000 CCD detector, with phosphor optimized for  $\text{Cu K}\alpha$  radiation. The images were analyzed with Fit2d and Origin 8.0 software. The distance from the

sample to detector, calibrated using silver behenate, was found to be ~23.2 cm. In the scattering, we can get the information about the Bragg spacing. Typical exposure times were of the order of 2 min.

## **6.3 Results**

### **6.3.1 Complex Formation Detected by Agarose Gel Retardation Assay**

To assess the formation of dendrimer/DNA complexes, agarose gel electrophoresis of the complex was performed at different weight ratios (Figure 6.1). Weight ratios were chosen over the more preferred N/P charge ratio due to the varying N/P with degree of modification in the zPAMAM samples. All samples were made using 1  $\mu\text{g}$  plasmid DNA. The results showed that the pUC18 plasmid DNA was complexed fully, showing complete retardation, by 2.7  $\mu\text{g}$  PAMAM for all PAMAMs studied except the 100% modified zPAMAM. For unmodified PAMAM, 2.7  $\mu\text{g}$  PAMAM is equivalent to an N/P charge ratio of 4. As anticipated, the fully anionic zPAMAM (100% modified) was unable to condense the negatively charged DNA.

### **6.3.2 Stability of zPAMAM/DNA Complexes**

In order to assess the stability of the different dendriplexes studied, we used agarose gel electrophoresis to visualize DNA release from the PAMAM polyplexes after exposure to the anionic polymer dextran sulfate (DS). All samples were made using 1  $\mu\text{g}$  plasmid DNA condensed by 4  $\mu\text{g}$  of unmodified or modified PAMAM. As discussed above, 2.7  $\mu\text{g}$  of PAMAM was observed to be sufficient for condensing all zPAMAM/DNA systems ranging from 0 to 40% modification. After incubating the dendriplexes for 10 min, varying amounts of dextran sulfate was added to each sample and allowed to incubate for another 20 min. The negatively charged DS competes for the PAMAM molecules against the DNA ultimately leading to plasmid release from the polyplexes if sufficient DS is added to the system. The results of this competition assay are shown in Figure 6.2. For all systems studied DS

induces DNA release. Stability was checked as a measure of the achieved by PAMAM: DNA weight ratios of 2.7 g: 1 g. For unmodified PAMAM this weight ratio is equivalent to an N/P charge ratio = 4. DNA released by agarose gel electrophoresis

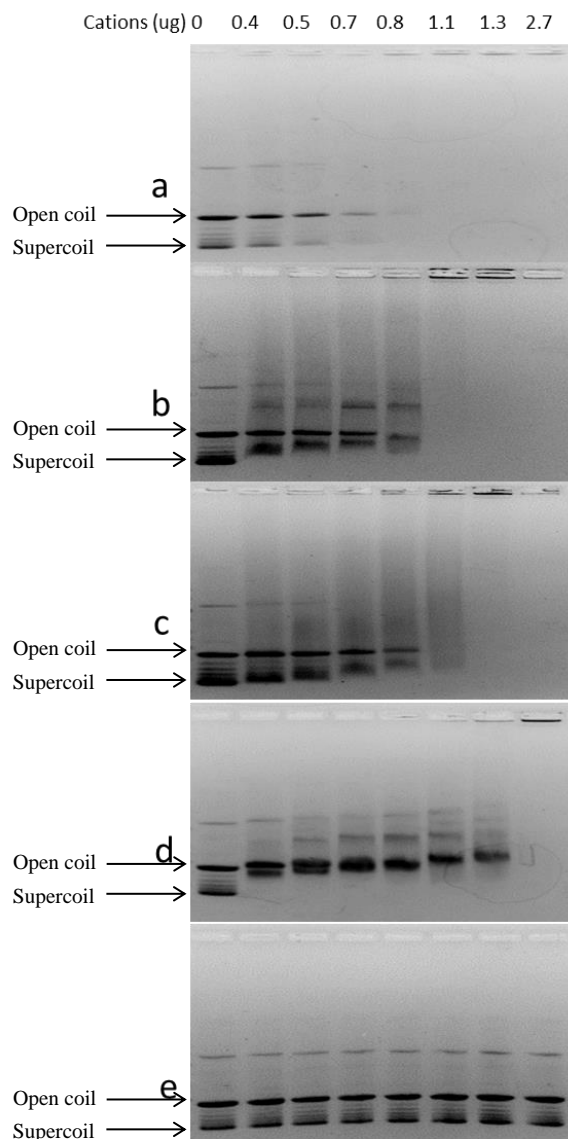


**Figure 6.1** Agarose gel electrophoresis retardation of pUC18 plasmid DNA by zwitterionic PAMAM polyplexes. Shown are pDNA condensed by a: G4 PAMAM; b: 15% modified G4 PAMAM; c: 24% modified G4 PAMAM; d: 40% PAMAM; e: 100% PAMAM. (The condensed DNA travels slower than free plasmid DNA, and fully condensed DNA trapped inside the wells.)

was compared to uncomplexed plasmid DNA. Higher percent modifications of the zPAMAM resulted in a decrease in the amount of DS required for complete DNA release.

### **6.3.3 Effect of Percent Modification on Particle Size of zPAMAM Dendriplexes**

Having shown that zPAMAM is capable of condensing DNA, we set out to examine how the colloidal properties of zPAMAM/DNA compare to unmodified G4 PAMAM/DNA dendriplexes. For efficient nucleic acid delivery *in vitro* and *in vivo*, polyplexes are required to form small, compact nanoparticles (typically < 150 nm). In order to evaluate the colloidal properties of zPAMAM/DNA, we used DLS to determine the hydrodynamic radius of the zPAMAM/DNA complexes with 0 to 40% modification. Here, our nanoparticle system was not optimized to achieve the smallest possible particles. Instead, we are more interested in comparing zPAMAM/DNA to PAMAM/DNA at the same dendrimer to DNA ratio weight ratio. Weight ratios rather than charge ratios were used due to the variation in charge for the different modified zPAMAMs. For DLS, ~3.75 µg of pUC18 was used per sample and condensed with 10 µg of PAMAM consistent with the 2.7:1 weight ratio shown by gel electrophoresis to be sufficient for complete DNA complexation for zPAMAM with 0 to 40% modification. Dendriplexes were incubated for 10 min at room temperature, brought up to a final volume of 500 µL with DI water and the particle size distributions and the hydrodynamic diameter (Dh) were measured by DLS. All samples gave rise to one population of nanoparticles with fairly small distributions in size. As shown in Table 6.1, the sizes of the PAMAM dendriplexes showed no dependence on the percent modification for zPAMAM/DNA complexes. The sizes of all dendriplexes were ~173 nm ± 17 nm. The independence of the physicochemical properties of zPAMAM dendriplexes on percent modification is of particular importance for potential future transfection experiments. Transfection is known to depend on particle size. Similar particle size for all zPAMAM/DNA formulations helps to reduce, although not

eliminate, potential confounding effects not directly related to the presence of zwitterionic charge in the zPAMAM.

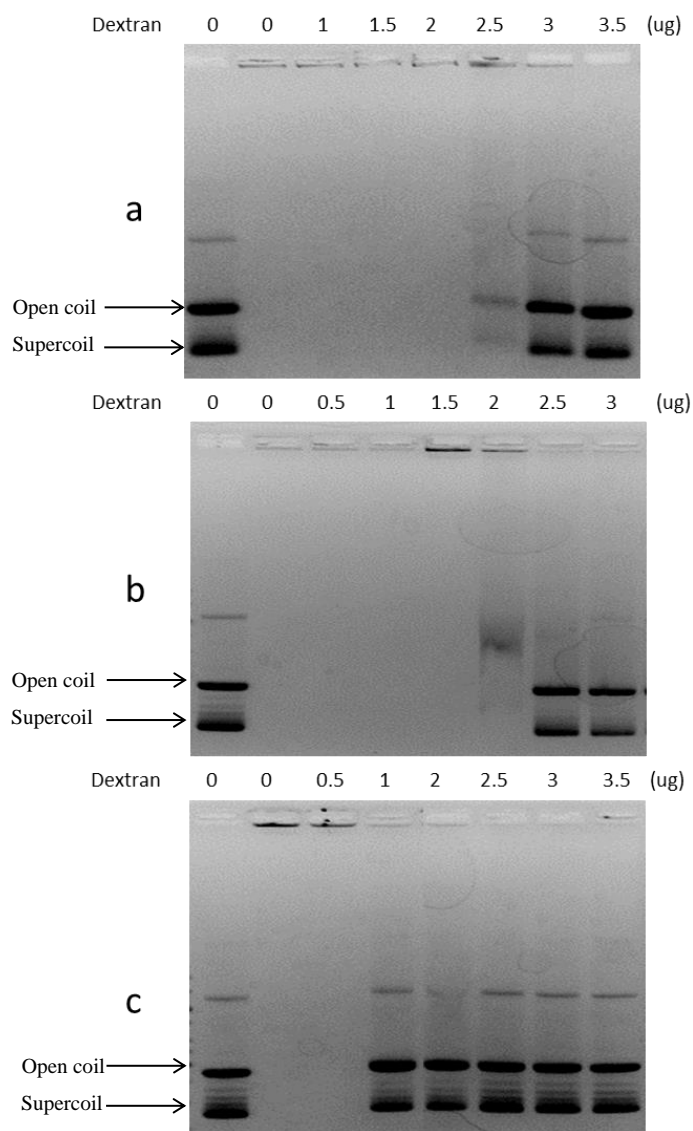


**Figure 6.2** Stability of zwitterionic G4 PAMAM polyplexes to competition with anionic dextran sulfate (DS). Shown is pUC18 DNA complexed with (a) G4 PAMAM, (b) 24% modified G4 PAMAM and (c) 40% modified G4 PAMAM. Here all polyplexes were initially formed at Dendrimer: DNA weight ratios of 4  $\mu\text{g}/1 \mu\text{g}$  then treated with increasing amounts of DS. Stability was checked as a measure of the DNA released by agarose gel electrophoresis compared to uncomplexed plasmid DNA. (The condensed DNA travels slower than free plasmid DNA, and fully condensed DNA trapped inside the wells.)

**Table 6.1** DLS table of hydrodynamic diameter of dendrimer/DNA complexes vs zwitterionic modification percent

G4 modified percent (%)	Hydrodynamic diameter, $D_h$ (nm)
0	$169 \pm 5$
15	$178 \pm 14$
24	$173 \pm 6$
40	$171 \pm 5$

### 6.3.4 Structural Studies of G4 PAMAM/DNA

#### 6.3.4.1 Stability of G4 PAMAM/DNA with Time

Before examining the structure of zPAMAM/DNA, we needed to examine in detail the resulting structure of DNA complexed by unmodified G4 PAMAM. First we examined the packaging of DNA prepared using the low salt preparation method, i.e. DNA and PAMAM mixed in 10 mM Tris, pH 7.5. After preparation, the resulting fibrous samples were maintained in a bath of 10  $\mu$ M Tris and 0.1  $\mu$ M excess G4-PAMAM to prevent concerns of possible leeching of dendrimer into the bathing solution from the fibrous precipitate. A  $\sim 10$  fold increase or decrease in the excess PAMAM concentration of the bath did not have an effect on the observed spacing between DNA helices in our samples. SAXS scattering profiles are given in Figure 6.3 for G4 PAMAM/DNA assemblies measured 1 hour, 2 weeks and 6 months after mixing. Initially, two peaks are observed. With limited scattering, we cannot easily discern a lattice from these structures so we will instead focus on a discussion of the Bragg spacings which are independent of the specific DNA lattice. The low  $Q$

reflection, corresponding to a larger spacing between DNA helices is observed at  $Q \sim 1.5 \text{ nm}^{-1}$  corresponding to a  $D_{Br} \sim 42 \text{ \AA}$ . The higher  $Q$  reflection is seen at  $Q \sim 2.1\text{-}2.2 \text{ nm}^{-1}$  corresponding to a  $D_{Br} \sim 29 \text{ \AA}$ ; more consistent with the Bragg spacings observed for the hexagonal packaging observed in G0/G1 PAMAM as well as linear polycation/DNA complexes. As a function of time, however, there is significant rearrangement within the G4 PAMAM/DNA samples suggesting these samples are not at equilibrium but are found to be kinetically trapped in non-equilibrium structures. Such rearrangements were not observed for the low generation PAMAM/DNA assemblies discussed in Chapters 4 and 5. At long times, the samples appear to shift primarily to the high  $Q$  state with shifts of  $>30\%$  in the observed Bragg reflection.

In an effort to overcome these non-equilibrium states, we also examined the stability of the G4 PAMAM/DNA assemblies prepared through a high salt preparation method. This high salt preparation was previously used by DeRouchey and found to help circumvent certain kinetic barriers in polyplex structures formed from DNA condensed by high molecular weight linear polycations.<sup>55</sup> We hypothesize that the low salt preparation may trap precipitates in non-equilibrium states brought about by rapid interaction of the polycation and DNA. Once formed, equilibration in these precipitates occurs extremely slowly. We believe the high salt method allows for the polycation and DNA to more thoroughly mix before precipitation occurs thus circumventing these kinetic barriers. Scattering profiles for the high salt preparation are given in Figure 6.4 for G4 PAMAM/DNA. The stability of these particles was checked after six months and no internal spacing rearrangements ( $<1\%$ ) was observed suggesting a more kinetically stable state has been achieved.

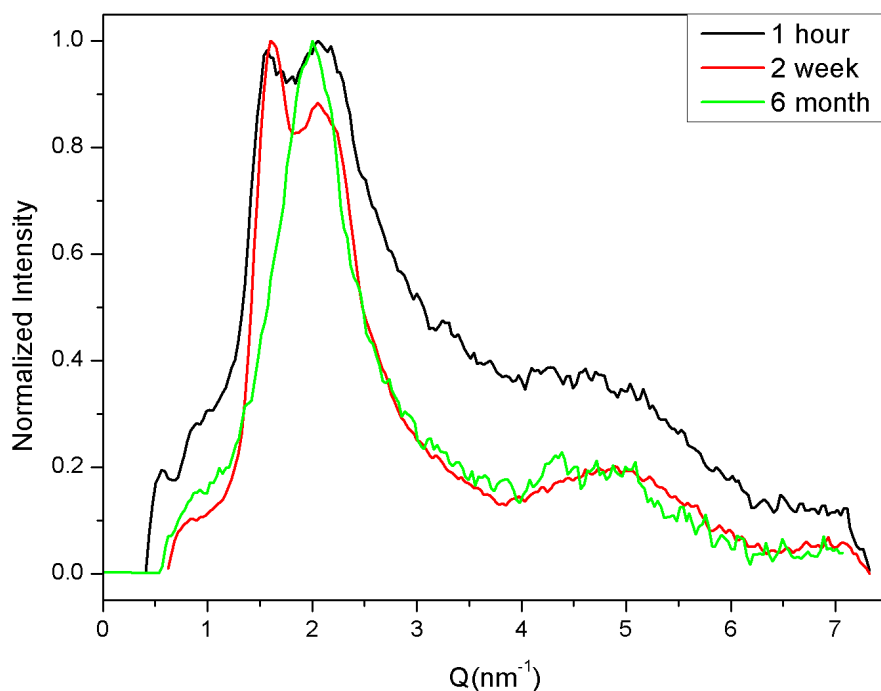


**Figure 6.3** Evolution of G4 PAMAM/DNA assembly structure with time made by the low salt preparation method. Scattering profiles shown are for  $N/P = 4$  and pH 7.5 recorded at various time intervals after dendriplex preparation

#### 6.3.4.2 Comparison of G4 PAMAM/DNA Condensed by High and Low Salt Preparations

Figure 6.5 shows the X-ray scattering intensity profiles for G4-PAMAM polyplexes prepared by both high and low salt preparation methods measured 2 weeks after condensation. It is clear from the figure that the DNA packaging resulting from the high salt preparation (red line) corresponds to the same Bragg reflection observed at high  $Q$  in the low salt preparation method (black line). These results are also consistent with Figure 6.3 which suggests at much longer time points (6 months), the low salt preparation samples are rearranging themselves preferentially to this same state.

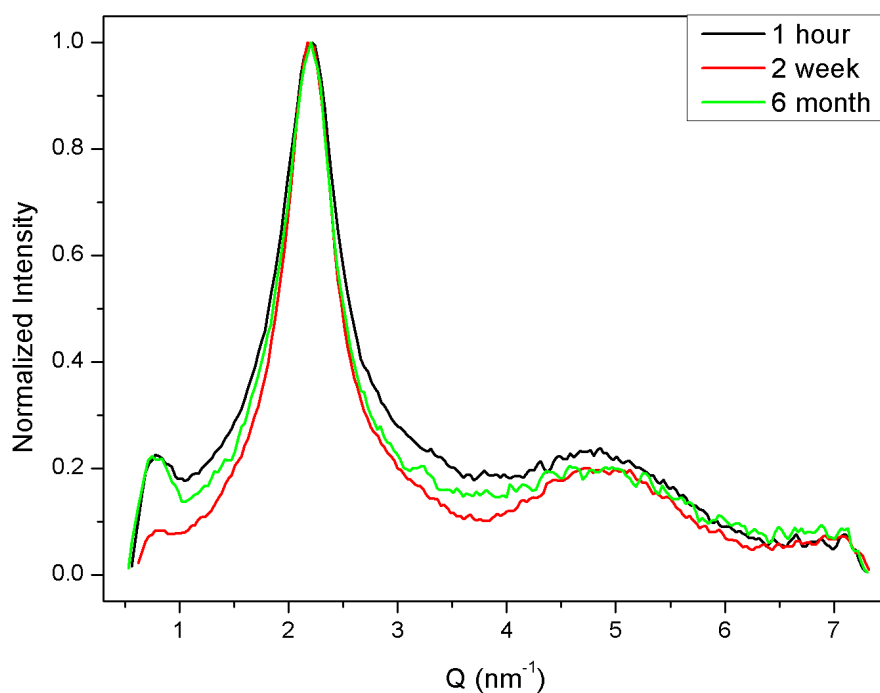


**Figure 6.4** The X-ray scattering profiles of DNA condensed by G4-PAMAM dendrimer by high salt preparation at different time points. The Bragg peaks stay at the same place during the equilibrated time for 6 months.

Next, we examined if DNA complexes formed by low salt preparation could be converted to the more kinetically stable state by dissolving at high salt then re-precipitating. These results are shown in Figure 6.6. Scattering intensity profiles for G4 PAMAM/DNA assemblies formed by high and low salt are shown equilibrated after 2 weeks. After examination by SAXS, the low salt preparation sample was subsequently dissolved in 2 M NaCl and incubated for 30min. This salt concentration was sufficiently high as to screen the interactions of the PAMAM with DNA preventing precipitation. The dissolved sample was then re-precipitated by the addition of DI water to drop the overall salt concentration and allow the PAMAM to interact with DNA thus inducing condensation. The reformed sample was washed thoroughly to remove excess salt then allowed to equilibrate for a couple days in the standard pH buffer solution (10 mM Tris, pH7.5, 0.1  $\mu$ M G4). As shown in Figure 6.6, the reformed sample is identical to the sample made directly by the high salt

preparation. High and low salt preparations will also be used to examine resulting structures formed in zPAMAM/DNA assemblies.

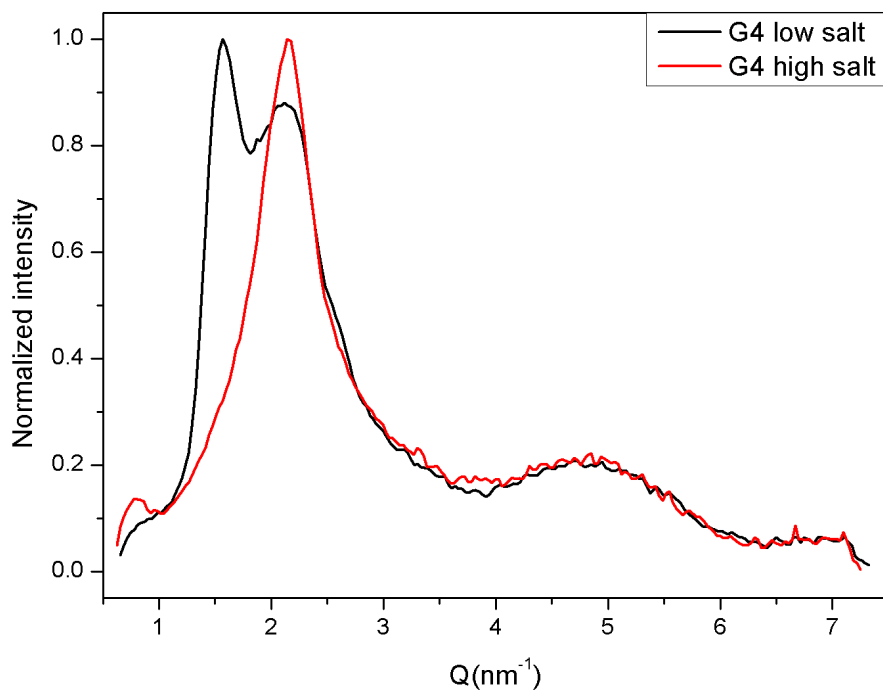


**Figure 6.5** X-ray scattering intensity profiles for G4-PAMAM polyplexes after 2 weeks. Under normal low salt preparation conditions, two peaks are observed in the PAMAM-DNA complexes indicating two different kinetically trapped phases are present. Using a high salt preparation, we are able to form only one phase which is kinetically stable.

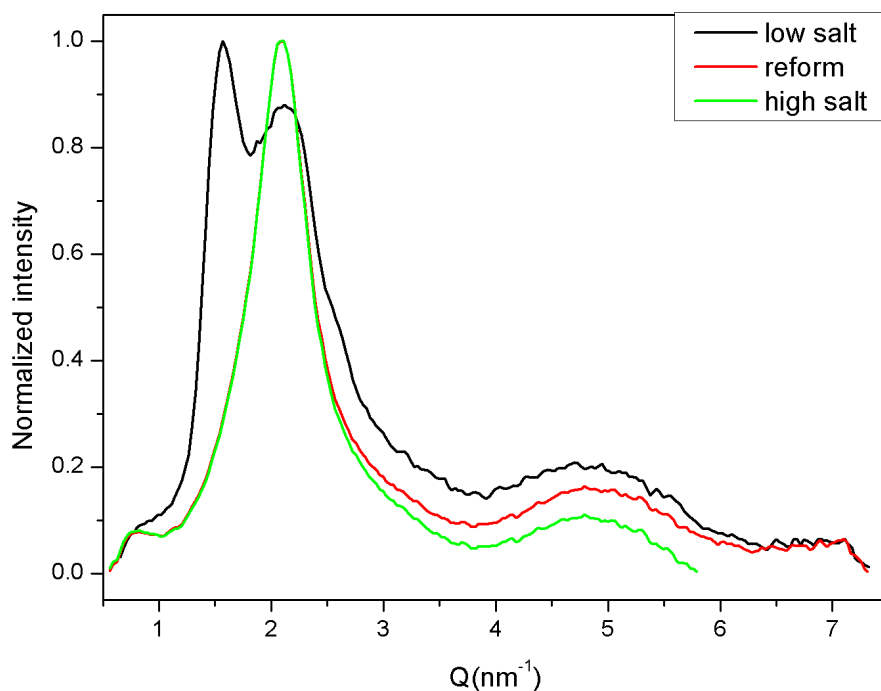


**Figure 6.6** The X-ray scattering profiles of reformed G4-PAMAM complexes by high salt preparation. We dissolved samples made by low salt preparation into 2 M NaCl solution, and then we can see that the Bragg peak of the reformed sample is the same as the Bragg peak of sample made by high salt preparation. And the position of the Bragg peak is at the higher  $Q$  value of the sample made by low salt preparation.

#### 6.3.4.3 Effect of Varying N/P Ratios on PAMAM/DNA Structure

Due to its potential as a gene delivery candidate, some previous X-ray studies of G4 and G6 PAMAM/DNA have been reported. In many cases, the sample preparation was different than the method used here and we note that the scattering observed by us is not the same as these published works. However, previous studies suggested that the DNA packaging was sensitive to the N/P ratio used to prepare the samples. In these works, dendriplexes were formed under low salt conditions. We examined G4 PAMAM/DNA mixed at  $N/P = 1.5$  to  $N/P = 6$  condensed using both the low and high salt preparation methods. All samples therefore had an excess of PAMAM amines relative to the concentration of phosphates from the DNA. After forming the fibrous precipitates as previously described, all the samples were transferred to the same 10

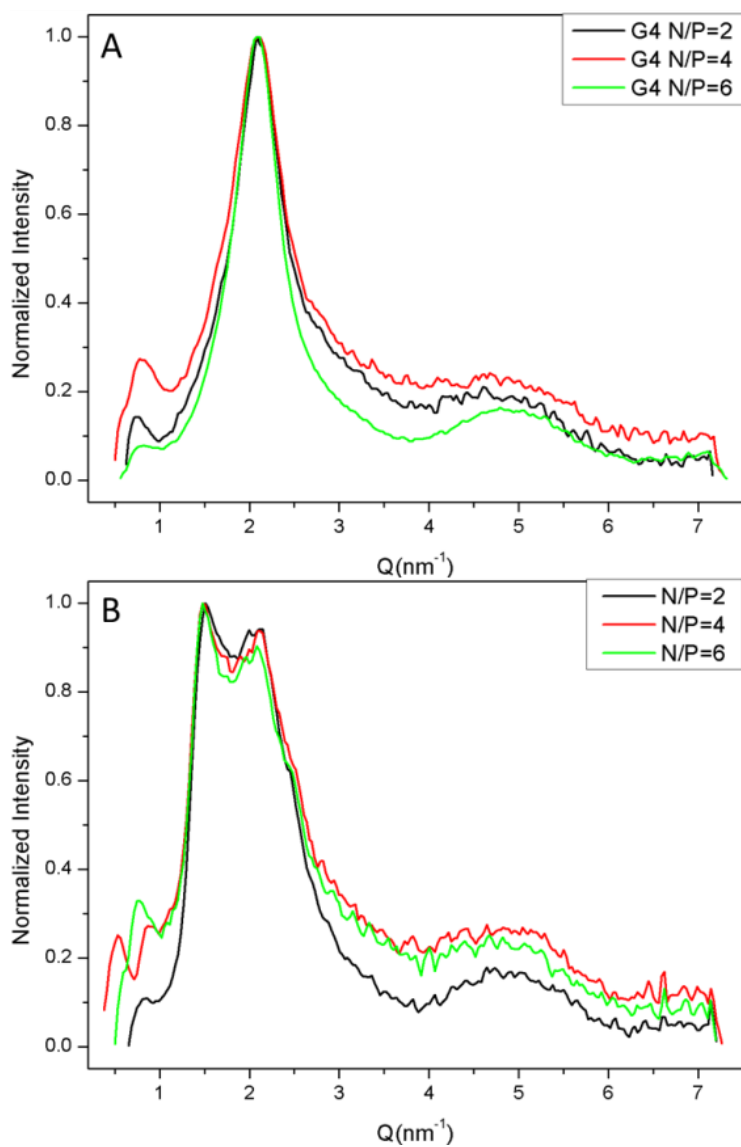
mM Tris (pH 7.5), 10  $\mu$ M G4 PAMAM bath and equilibrated for 2 weeks. These results are given in Figure 6.7.

Figure 6.7A shows the scattering profiles measured using the high salt preparation for PAMAM/DNA mixed at N/P 2, 4, and 6. Only one sharp peak is observed that does not show any significant shift in  $Q$  as a function of the N/P ratio. Similarly the low salt prepared PAMAM/DNA samples, shown in Figure 6.7B, also show no significant change in the peak positions as a function of the N/P ratio at mixing.

#### **6.3.4.4 pH Dependence on G4-PAMAM DNA Structure by High Salt**

##### **Preparation**

It is known that PAMAM will carry different amounts of charges at different pH due to the pKa's of the primary and tertiary amines inside the molecule.<sup>122,158</sup> As discussed in Chapters 4 and 5, we used pH to examine the phase behavior in low generation PAMAM/DNA complexes. Previous structural studies on high generation PAMAM/DNA also reported changes in structure at different dp conditions where dp means the degree of protonation or the ratio between protonated amine groups and total amine groups.<sup>36,37</sup> Under pH 7.5, it is thought that only the primary amines at the PAMAM structure are charged while the interior tertiary amines are uncharged resulting in a  $dp = 0.5$ . Here, we examined G4 PAMAM/DNA made by the high salt preparation as a function of the pH at mixing. For our samples, both DNA and PAMAM were dissolved in the appropriate pH buffer. Buffers used include: 10 mM NaOAc for pH 4, 10 mM MES for pH 6, 10 mM Tris for pH 7.5 and pH 8. For all pHs, mixing at 2 M NaCl prevented interaction of the PAMAM with DNA due to charge screening. Condensation was induced by the addition of DI water to reduce the solution salt concentration and allow PAMAM to interact with DNA. Condensates were subsequently washed and equilibrated for two weeks in 10 mM pH buffer before being examined by SAXS. Figure 6.8 shows the scattering profiles and calculated Bragg spacings of the G4-PAMAM/DNA complexes condensed at different pH. All the samples showed a single Bragg reflection that moved to smaller  $Q$  values with



**Figure 6.7** Scattering profiles of DNA condensed by G4-PAMAM at different N/P ratios using (A) the high salt preparation and (B) the low salt preparation method described in methods. After condensation, all samples were equilibrated in the same bath solution [10 mM Tris, pH 7.5, 0.1  $\mu$  M G4-PAMAM]. No significant shift in the peak position is observed as a function of the N/P ratio at mixing in either method.

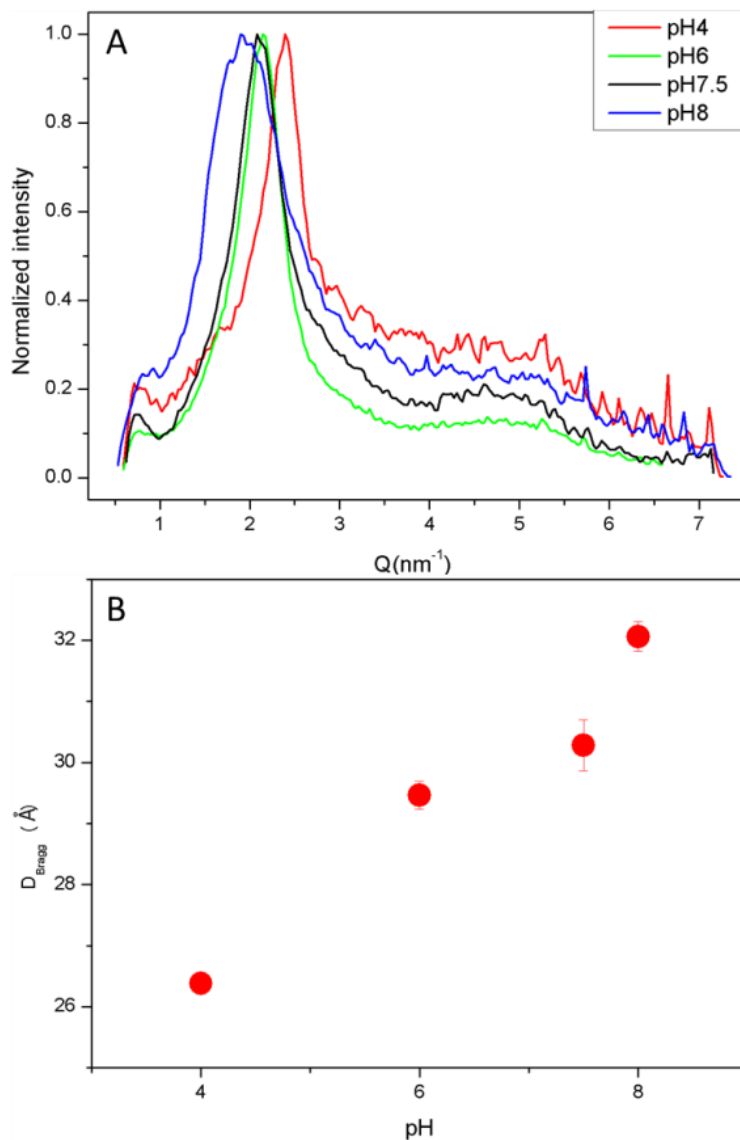


**Figure 6.8** High salt prepared G4-PAMAM/DNA complexes condensed at different pH. (A) Scattering profiles for PAMAM/DNA condensed at pH 4 to pH 8. (B) Calculated Bragg d spacing for the different pHs. Decreasing the pH is observed to decreasing the observed Bragg spacing.

increasing pH. Due to the inverse relationship between reciprocal space ( $Q$ ) and real space ( $D$ ), this indicates tighter DNA packaging, smaller d spacings, occurred at the lowest pH. We do note that complexes condensed at pH 8 did show significantly broader scattering than the other pH values suggesting a structural transition may occur at higher pH.<sup>158</sup>

#### **6.3.4.5 pH Dependence on G4-PAMAM DNA Structure by Low Salt Preparation**

We also examined the pH dependence of the PAMAM/DNA structure when prepared using the low salt preparation method. Samples were prepared in the same manner as in 4.2.4: stock solutions of both DNA and PAMAM were maintained at the desired pH, and then the solutions were allowed to mix in 10 mM of pH appropriate buffer to induce condensation. After precipitation, the fibrous condensate was then transferred to a fresh 10 mM pH appropriate buffer and equilibrated for 2 weeks before examination by SAXS. Figure 6.9 shows the results of these experiments. In Figure 6.9A, we see that at pH 7.5 we observe the two distinct Bragg reflections discussed previously. pH 8 shows a single but significantly broader than normal peak that nearly lies on top of the pH 7.5 scattering profile. This may indicate that this sample is still showing the same two states but the definition between states was not resolved in this particular sample. Interestingly, at low pH (pH 6 and 4), the scattering profiles show only a single sharp peak, suggesting uniform structure, which then continues to shift to higher  $Q$  with decreasing pH similar to the high salt preparation samples. Indeed, the calculated  $D_{Br}$  peaks for these samples are the same comparable to those prepared by the high salt method at the same pH. This may suggest lowering the pH at condensation is another means to overcome these kinetically trapped non-equilibrium states observed at ambient pH. It does appear that lowering pH still does shift the DNA spacings somewhat as well.

#### **6.3.5 Structural Studies of zPAMAM/DNA**

##### **6.3.5.1 Effect of Percent Modification on zPAMAM/DNA Structure**

In order to see the effect of zwitterionic dendrimers on dendriplex internal structure, we used SAXS to examine the internal structure of zPAMAM/DNA complexes with different degrees of modification of their surface groups. Due to the studies on G4 PAMAM/DNA discussed in Section 6.3.4, we chose to focus on zPAMAM/DNA prepared by the high salt preparation method resulting in more

equilibrium structures. Here all samples were prepared at pH 7.5 and equilibrated for 2 weeks before analysis by SAXS. Figure 6.10 shows the resulting scattering profiles for zPAMAM/DNA prepared by high salt method with surface group modification ranging from 0 to 40%. While unmodified PAMAM/DNA made at high salt resulted in a well defined single Bragg reflection, increasing the zwitterionic nature of the PAMAM appeared to induce a phase transition to a two state system again. While it is hard to discern the exact nature of this phase transition it is clear that increased modification of the PAMAM primary surface amines resulted in a significant shift to lower  $Q$ ; or equivalently larger spacings between the DNA helices. Figure 6.10B gives approximate Bragg spacings for the dominant peak. While not conclusive, it would appear that 15% modification resulted in a shift of the primary Bragg reflection to smaller  $Q$  but also the appearance of a smaller peak at even lower  $Q$ . By 24% modification, only a single broad peak is resolved but the width of which may suggest this is an approximate 50/50 distribution of these two reflections observed at 15%. By 40%, two structures are again resolved but this time with the low  $Q$  peak apparently dominate within the structure. The position of this peak also suggests a further shift to larger DNA-DNA spacings with increasing percent modification. While the exact structure is not evident, it is clear that as predicted the incorporation of negative charges into a zwitterionic PAMAM molecule does allow for the tuning of the dendrimer-DNA interactions. As hypothesized, more negative character results in less tight packaging.

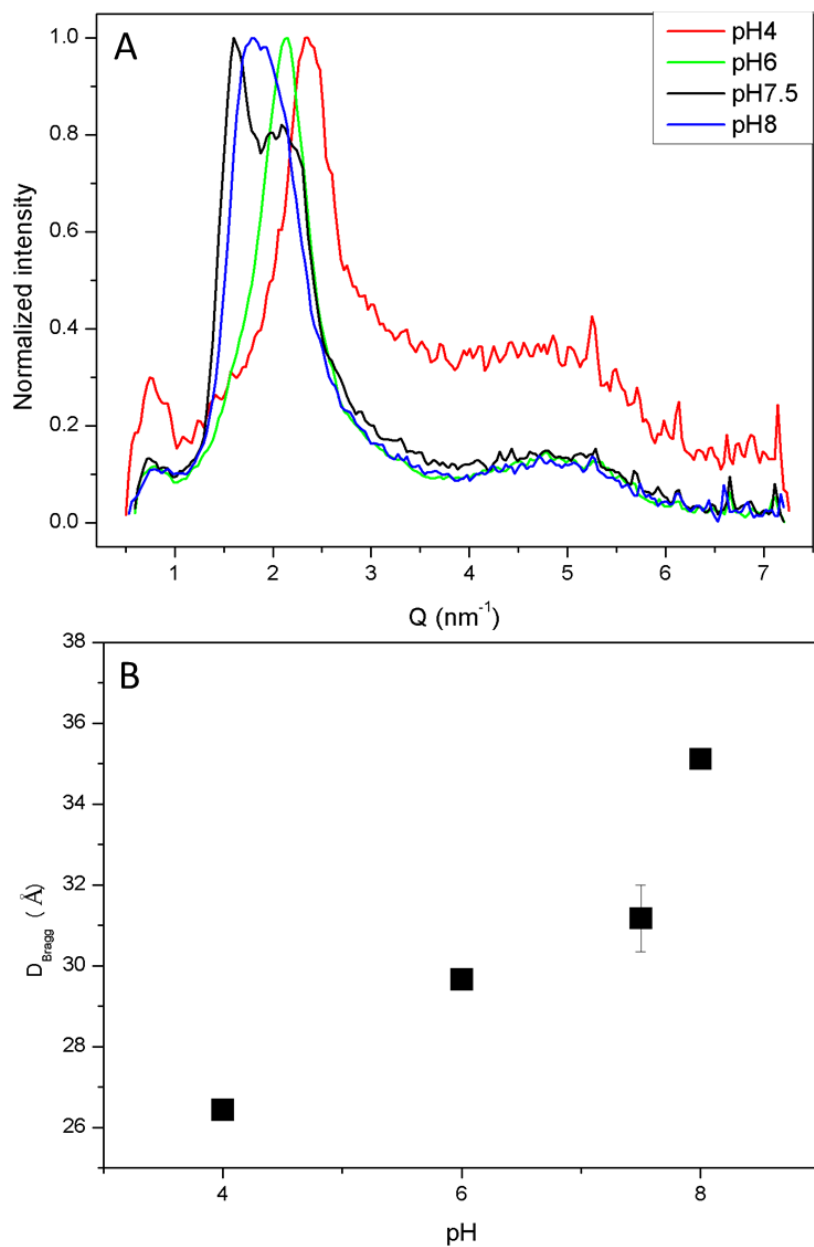


**Figure 6.9** Low salt prepared G4-PAMAM/DNA complexes condensed at different pH. (A) Scattering profiles for PAMAM/DNA condensed at pH 4 to pH 8. (B) Calculated Bragg d spacing for the different pHs. Decreasing the pH is observed to decreasing the observed Bragg spacing as well as potentially overcome the kinetically trapped state observed at pH 7.5.

### 6.3.5.2 Comparison of zPAMAM/DNA to PAMAM/DNA Made by High and Low Salt Preparations

All the zPAMAMs complexes discussed in 6.3.5.1 were prepared by the high salt method only. The resulting scattering peaks were significantly broader than observed for unmodified PAMAM/DNA. Comparing the scattering profiles for the different zPAMAM complexes, made only by the high salt method, to unmodified PAMAM/DNA made by both high and low salt preparations is instructive. This comparison is shown in Figure 6.11. Unmodified PAMAM (0%) made by the high salt preparation is shown in black and by low salt preparation by the pink line. The zPAMAM/DNA scattering profiles overlay these two curves well. It appears that with increasing percent modification, or increasing zwitterionic character, induces a phase transition between the two phases observed in PAMAM/DNA. Higher percent modification, even under high salt preparation, appears to transform the zPAMAM DNA complex internal structure from the kinetically stable phase observed in unmodified PAMAM dendriplexes made at high salt to the same phase observed to be kinetically unstable for PAMAM/DNA made at low salt. Comparing 40% modified zPAMAM, to low salt prepared PAMAM/DNA, the highly modified zPAMAM appears to show the same two phases but with an even higher ratio of low  $Q$  ( $Q \sim 1.7 \text{ nm}^{-1}$ ) compared to the higher  $Q$  phase ( $Q \sim 2.1 \text{ nm}^{-1}$ ).

Next, we examined zPAMAM/DNA complexation when condensed under low salt conditions. Figure 6.11 shows the scattering profiles of zPAMAM/DNA complexes. Surprisingly, here there is no observed change in the Bragg reflection for 0, 15 and 24% modification. The resolution is low but we believe all three of these samples are showing two Bragg reflections with structures comparable to the low salt prepared unmodified PAMAM/DNA sample. 40% modified zPAMAM/DNA did form a precipitate however there was no observed Bragg scattering peak in the  $Q$  range available to us on our instrument. This may suggest a Bragg spacing too large

for us to resolve in house. Such scattering might be observed on a true SAXS instrument, where the sample to detector distance is  $\sim 1$  meter.

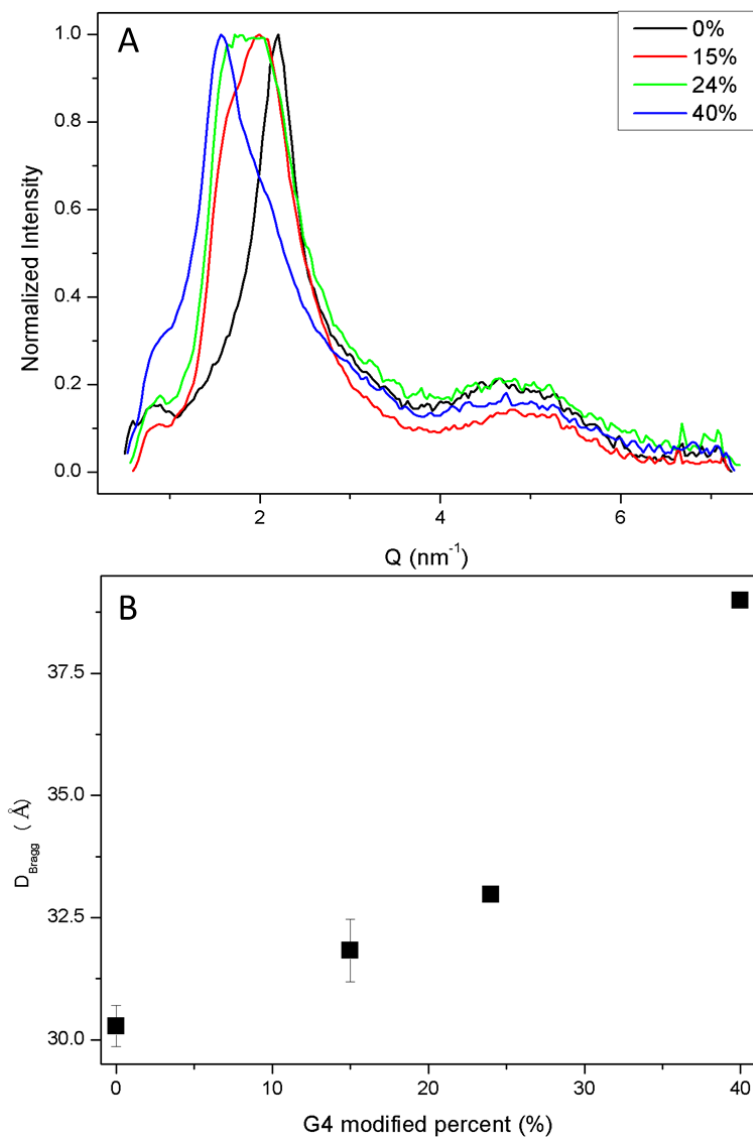


**Figure 6.10** High salt prepared zPAMAM/DNA complexes as a function of the percent modification of the G4 PAMAM surface (A) Scattering profiles for PAMAM/DNA condensed at pH 7.5 after two weeks equilibration. (B) Calculated Bragg spacing. Packaging within the zPAMAM/DNA scales with the percent zwitterionic nature of the dendrimer.

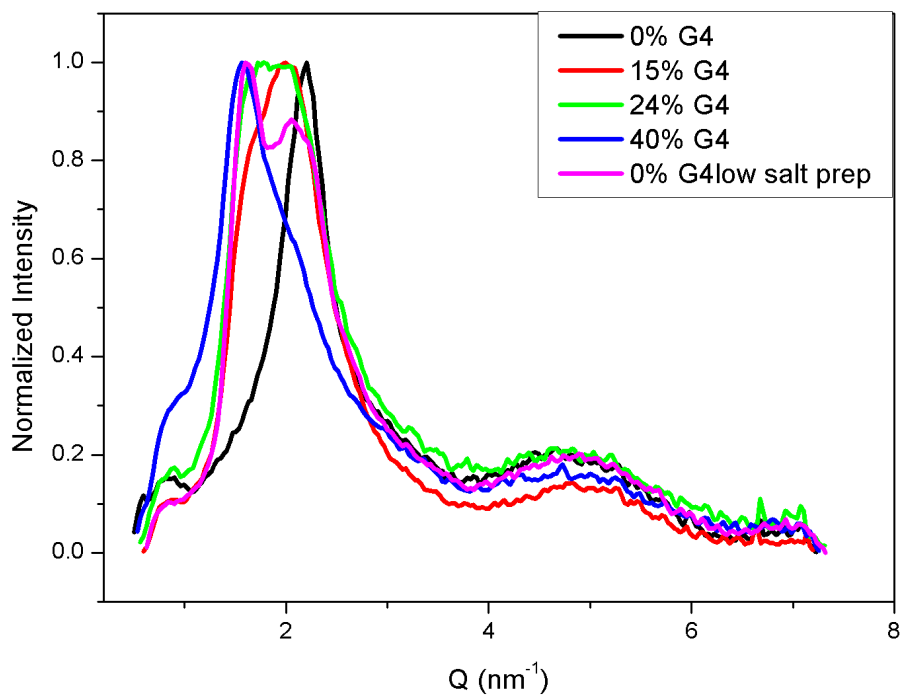


**Figure 6.11** Scattering profiles of zPAMAM/DNA condensed using the high salt method compared to unmodified G4 PAMAM/DNA complexes formed by low (pink line) and high salt preparation (black line).

### 6.3.5.3 Stability of zPAMAM/DNA with Time

Next, we examined the evolution of zPAMAM/DNA assembly structure with time for both high and low salt preparations. These results are shown in Figure 6.12 for DNA condensed by 15 and 24% modified zPAMAM. Similar to PAMAM/DNA, the low salt preparation shows clear rearrangements with time over the scale of months. The high salt preparation does not appear to undergo significant rearrangements though some rearrangement may be happening for the higher 24% modified zPAMAM sample.

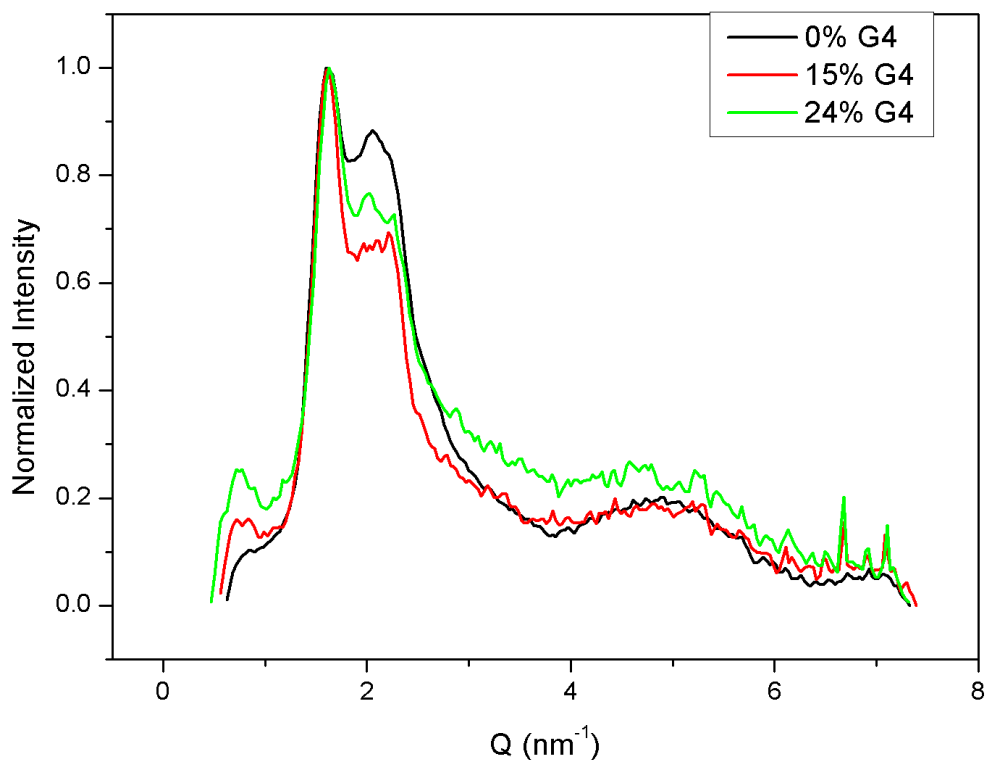


**Figure 6.12** Scattering profiles of z-PAMAM/DNA complexes made by low salt preparation. All samples appear to show two Bragg reflections that do not shift peak position significantly for percent modifications between 0 and 24%. 40% modified zPAMAM/DNA did form a precipitate but no scattering peak was observed in the  $Q$  range of our in house SAXS instrument.

### 6.3.6 Phase Behavior of PAMAM/DNA and zPAMAM/DNA as a Function of Added Salt Concentration

#### 6.3.6.1 Salt Effects on DNA Condensed by G4 PAMAM

We hypothesized that the incorporation of carbonyls into the cationic PAMAM will result in a tuning of polymer-DNA interactions. We have shown this is the case for zPAMAM/DNA where changing the percent modification has been shown to alter the condensation and decondensation as well as the resulting internal structure. From our previous studies, we know that with addition of NaCl, the packaging and phase behavior of low generation PAMAM/DNA is greatly perturbed. We hypothesize that the incorporation of negative moieties into the PAMAM will affect the sensitivity of

zPAMAM to salt. Before examining the phase behavior of zPAMAM/DNA, we must first look at unmodified G4 PAMAM/DNA.

For these studies, all PAMAM/DNA samples were prepared by either the high or low salt method then equilibrated in 10 mM Tris (pH 7.5), 0.1 $\mu$ M G4 PAMAM solution for two weeks. Following equilibration, these samples were transferred to the desired NaCl salt/10 mM Tris buffer solution and equilibrated for another 3 days before examination by SAXS. Figure 6.13 shows the  $D_{Br}$  of G4-PAMAM/DNA as a function of added NaCl concentration. Here we show both low and high salt preparation are shown. For the low salt PAMAM/DNA samples, two Bragg reflections are observed and both peaks are plotted. With increasing salt concentration, the observed Bragg spacings increase. As shown in Figure 6.12, the higher  $Q$  (or lower  $D$ ) peak in the low salt preparation samples matches the high salt preparation samples at all salt concentrations suggesting they are the same structure; most likely hexagonal packaging.  $D_{Br}$  increases with increasing added NaCl concentration. For the low salt preparation, the low  $Q$  phase reaches to  $\sim 45$  Å before the peak is lost at 450 mM NaCl. For both preparations, the higher  $Q$  phase maintains structure to higher added salt concentrations resulting in a  $\sim 42.2$  Å Bragg spacing observed at 600 mM NaCl before scattering is lost at 650 mM.

#### 6.3.6.2 Salt Effects on DNA Condensed by zPAMAM

We next examined the effect of zPAMAM on the salt sensitivities of the resulting dendriplexes. zPAMAM/DNA was prepared using the high salt preparation followed by equilibration in 10mM Tris, pH7.5, 0.1 $\mu$ M G4-PAMAM for two weeks. After equilibration, samples were moved to the appropriate salt: buffer solution for three days before SAXS measurements. Figure 6.14 and Figure 6.15 shows the salt sensitivities of zPAMAM dendriplexes compared to unmodified PAMAM/DNA. In Figure 6.15 A, we plot the Bragg spacing as a function of added salt concentration. Surprisingly, 15 and 24% modified samples look nearly identical to the high  $Q$  peak of unmodified PAMAM/DNA. These similar phases do not appear to have a rate of

swelling that varies significantly with the percent zwitterionic nature of the zPAMAM.

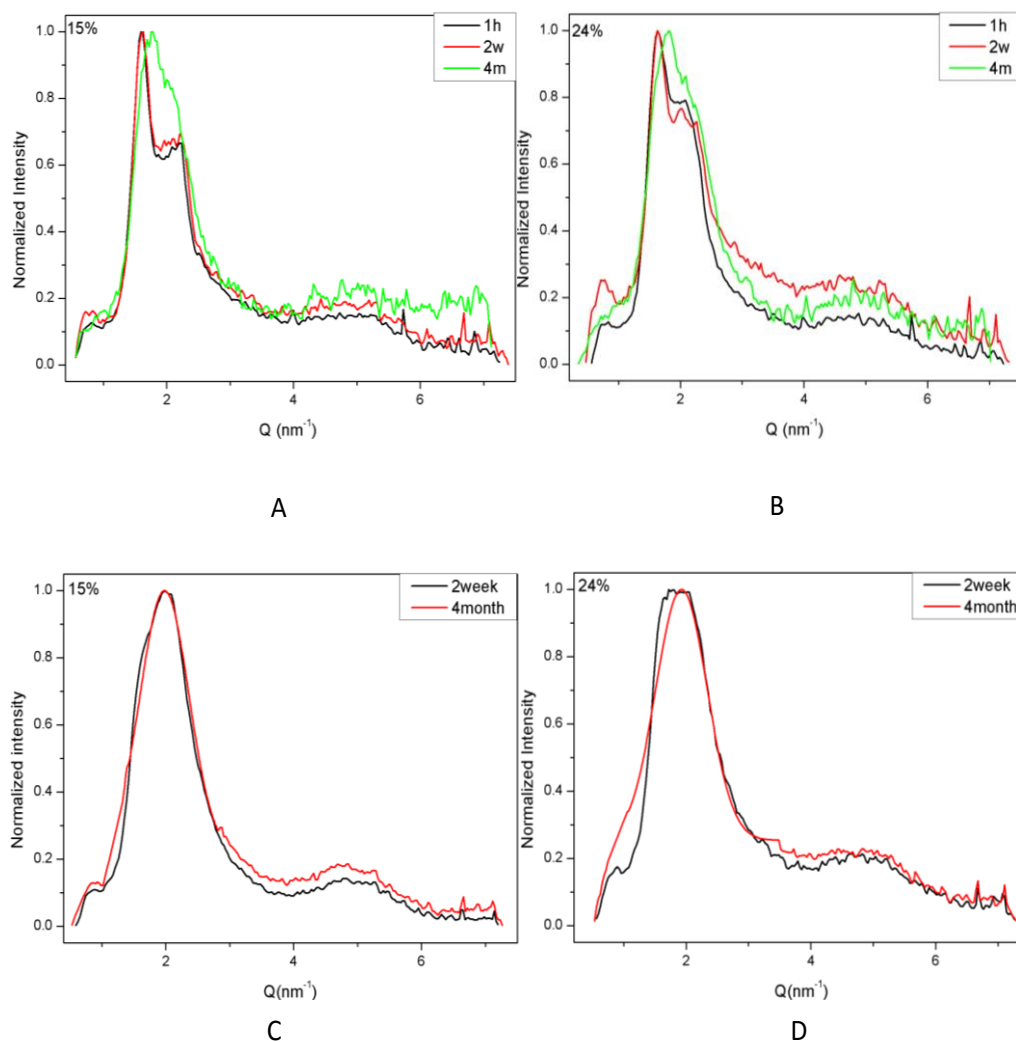


**Figure 6.13** Time evolution of X-ray scattering profiles of zPAMAM/DNA complexes. (A) and (B) show zPAMAM/DNA prepared by the low salt method at 15% and 24% modification; respectively. (C) and (D) show zPAMAM/DNA prepared by the high salt method at 15% and 24% modification; respectively. zPAMAM dendriplexes prepared by low salt show significant rearrangement with time. zPAMAM/DNA made by high salt do not show rearrangement with time.

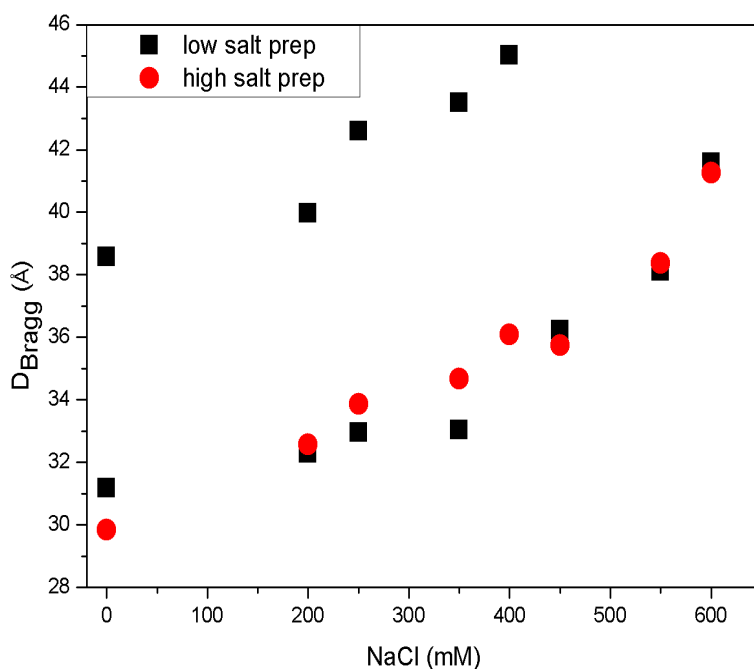


**Figure 6.14** Bragg spacings for G4 PAMAM/DNA as a function of increasing added NaCl concentration.

40% modified zPAMAM, is nearly identical to the low  $Q$  phase seen in unmodified PAMAM/DNA and swells in a very similar manner to low salt prepared PAMAM/DNA. These peaks are plotted in Figure 6.13 but removed here for clarity. As there are some variations in the equilibrium spacing ( $D_{Br,eq}$ ), in 6.13B we plot the relative change in Bragg spacing as well. Again the percent zwitterionic nature does not play a significant role in the amount of observed swelling however while G4 PAMAM/DNA swells approximately 12 Å from equilibrium, the zPAMAM all swell approximately 6 Å before dissolution. Also the higher percent modified zPAMAM systems do appear to completely fall apart at a lower added salt concentration. Lastly, this data was normalized in Figure 6.15 to show the relative change in the Bragg spacings with added salt concentration.

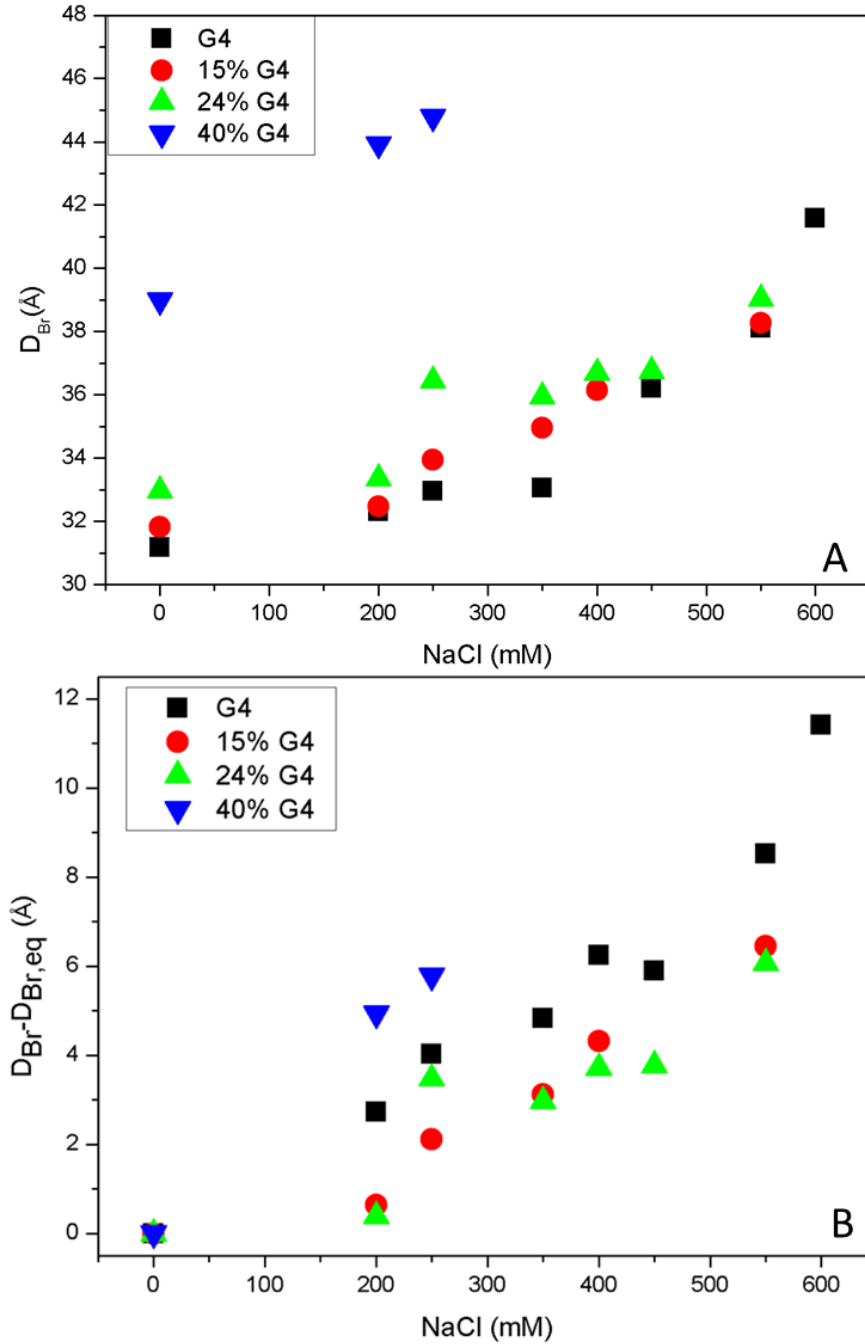


**Figure 6.15** Salt effects on z-PAMAM/DNA complexes. Figure A shows the  $D_{Br}$  values of z-PAMAM/DNA as a function of increasing NaCl concentration. Figure B shows the change in Bragg spacing,  $D_{Br} - D_{Br,eq}$ , for each zPAMAM/DNA system as a function of added salt concentration.

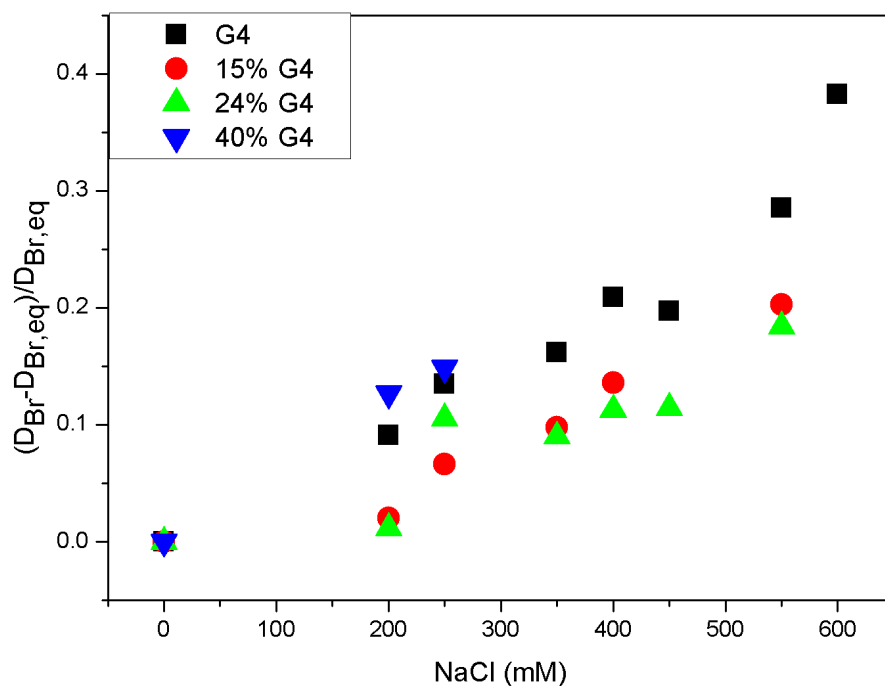


**Figure 6.16** The relative changes of  $D_{Br}$  for different z-PAMAM complexes as a function of NaCl concentration. With the NaCl concentration increasing, the relative change of  $D_{Br}$  increases for all complexes. The interesting thing here is that the slopes of the change are almost the same for all the complexes as a function of NaCl concentration.

## 6.4 Discussion

Dendrimers, such as PAMAM, have been widely studied for their ability to delivery drugs and genes into cells due to their well-defined structures, molecular weights and surface properties.<sup>159-172</sup> As with most polycations, PAMAM development has been hindered in vivo due to both their formation of highly charged nanoparticles that can interact unspecifically with blood components, proteins, or non-target cells, as well as, their inherent cellular toxicity in the free, unbound state. For example, studies have shown high generation PAMAM can break cell membranes when they penetrate into cells<sup>15</sup> and even induce apoptosis in cells.<sup>173</sup> We proposed to use zwitterionic macromolecules (zPAMAM) to simultaneously tune polymer-DNA interactions, to optimize DNA condensation and release, as well as reduce cytotoxicity. In collaboration, with the laboratory of Dr. Vincent Rotello (UMass), a

series of zPAMAM polymers were synthesized from commercially available G4 PAMAM with varying degrees of modification of the surface primary amines to carboxylic acid groups. The purpose of this work was to assess zPAMAM's ability to condense and release DNA as well as determine the resulting internal structure and compare it to unmodified G4 PAMAM/DNA assemblies.

Using gel electrophoresis, we first established that unmodified G4 PAMAM and zPAMAM were capable of fully condensing plasmid DNA (Figure 6.1). Only 100% modification of PAMAM was unable to condense DNA at any weight ratio of dendrimer:DNA. Increasing the percent zwitterionic nature of the PAMAM reduced the overall charge and so more material was required to fully condense DNA with zPAMAM. Similarly gel electrophoresis allowed us to ascertain that the stability of these complexes, and their ability to release DNA from the dendriplex, was dependent on the percent modification of the PAMAM molecules (Figure 6.2). Higher percent modified zPAMAM, released DNA fully at lower competitor (dextran sulfate, DS) to DNA ratios. This is presumably due to the reduced overall charge on the zPAMAM allowing DS to more effectively compete for binding to the DNA against zPAMAM. Lastly, we also used DLS to measure the colloidal properties of zPAMAM: pUC18 complexes. Surprisingly, the hydrodynamic radii,  $D_h$ , for zPAMAM:DNA were observed to be independent of the percent modification and nearly identical to the  $D_h$  for PAMAM:DNA (Table 6.1).

We next turned our attention to the internal structures of the PAMAM/DNA and zPAMAM/DNA systems. Our focus was to examine the effect of the percent zwitterionic nature of the polycation on the DNA packaging within the dendriplexes. For this work, we used high MW linear DNA (chicken blood). Previously, we have observed little to no difference in the DNA spacings resulting from polyplexes using linear DNA or plasmid DNA. Before examining zPAMAM/DNA, we began by examining the structure of G4 PAMAM/DNA. Condensation of CB DNA with G4 PAMAM in typical "low salt" conditions resulted in the observation of two different

phases characterized by two different Bragg reflections at  $Q \sim 1.58 \text{ nm}^{-1}$  and  $2.10 \text{ nm}^{-1}$ . Time evolution of these structures showed that the low  $Q$  phase was non-equilibrium state that changed at the time scale of months. We show that using a high salt preparation method allows us to circumvent this non-equilibrium state resulting in a one-phase system characterized only by the high  $Q$  peak ( $Q \sim 2.10 \text{ nm}^{-1}$ ) as shown in Figures 6.4 and 6.5.

Previous work with dendrimer: DNA have proposed many potential structures including hexagonal, square planar, and bead on a string structures based on the idea that the high generation dendrimers act as hard spheres, similar to histones, resulting in DNA wrapping around them. Comparing our work on fibrous dendrimer: DNA samples to previously published SAXS studies of G4 PAMAM: DNA complexes in solution, we see our samples do not agree with previous published results. For example, many studies claim a change in the internal structure as a function of the N/P ratio in PAMAM: DNA that we did not observe (Figure 6.7). We do however see the pH at condensation is capable of inducing internal structure change (Figure 6.8). One limitation for more precise structure determination is our in house X-ray instrument has a much smaller sample to detector distance than traditional SAXS thus limiting our accessible  $Q$  range.  $Q$  less than  $\sim 1.3 \text{ nm}^{-1}$  cannot be easily resolved equivalent to  $D_{Br}$  spacings larger than  $\sim 50 \text{ \AA}$ . For most work on condensed DNA phases such large spacings do not exist. Some previous reports on dendrimer:DNA complexes, with larger generation number, however have shown Bragg reflections corresponding to spacings larger than  $50 \text{ \AA}$ .

One of the most comparable studies to our work was done by Shu-Fen Peng et al.<sup>174</sup> They reported a series of scattering profiles G4 PAMAM: DNA at a degree of protonation (dp) of 0.5-0.6 as shown in Figure 6.16. This dp is comparable to our near neutral pH work (pH 7.5) where only the primary amines on the surface are protonated representing approximately half of the total amines in the PAMAM molecule (the other half being non-protonated tertiary amines inside the dendrimer

cavities). As a function of  $dp$  and N/P ratio Peng and coworkers have proposed a transition from bead on a string (BOS) structures to hexagonal packaging. Some of these peaks are similar in  $Q$  to what we observe in our fibrous DNA samples but do not exactly match. Also, comparison of comparable  $dp$  samples, our scattering profiles look quite different and show no dependence on N/P ratio as they have suggested. Our data is consistent with the concept of a phase transition occurring between a low  $Q$  (large  $D$  structure) and a high  $Q$  (small  $D$ ) structure within the PAMAM and zPAMAM dendriplexes. Our work shows a number of ways to transition between these structures including the percent zwitterionic nature of the PAMAM which even under high salt conditions appears to shift the internal structure from the kinetically stable, more tightly packed state (presumably hexagonal) to a structure nearly identical to the more open, non-equilibrium state observed in G4 PAMAM dendriplexes condensed at low salt. Further studies including synchrotron X-ray scattering and small angle neutron scattering (SANS) are needed to better characterize the exact structures existing in zPAMAM: DNA.

Finally, we examined the phase behavior of PAMAM: DNA and zPAMAM:DNA to added NaCl concentration. We had hypothesized that the incorporation of zwitterionic nature into PAMAM would result in a destabilization of the dendriplexes which was consistent with the competition studies using dextran sulfate to induce DNA release. We anticipated that this would also mean that zPAMAM would be more sensitive to the presence of added salt and the resulting phase behavior would also be dependent on the percent modification of the polymer. However, our salt studies are not consistent with this. We focused on zPAMAM: DNA condensed using the high salt method. Instead 15% and 24% zPAMAM looks nearly identical to unmodified G4 PAMAM as a function of added salt. 40% zPAMAM is nearly identical to the non-equilibrium, low  $q$  phase observed in PAMAM: DNA condensed at low salt. Looking at the relative changes (Figure 6.15), they also have similar slopes to G4 PAMAM: DNA suggesting the zwitterionic response to salt is similar to the purely cationic dendrimer. The only observed difference is the percent

modification does lead to the dendriplexes falling apart at lower added salt concentrations when compared to unmodified PAMAM. So the internal structures are similar but the zwitterionic nature does lead to destabilization of the PAMAM: DNA interactions. 40% zPAMAM especially is only stable to ~300 mM added salt approximately  $\frac{1}{2}$  the salt stability of unmodified PAMAM: DNA.

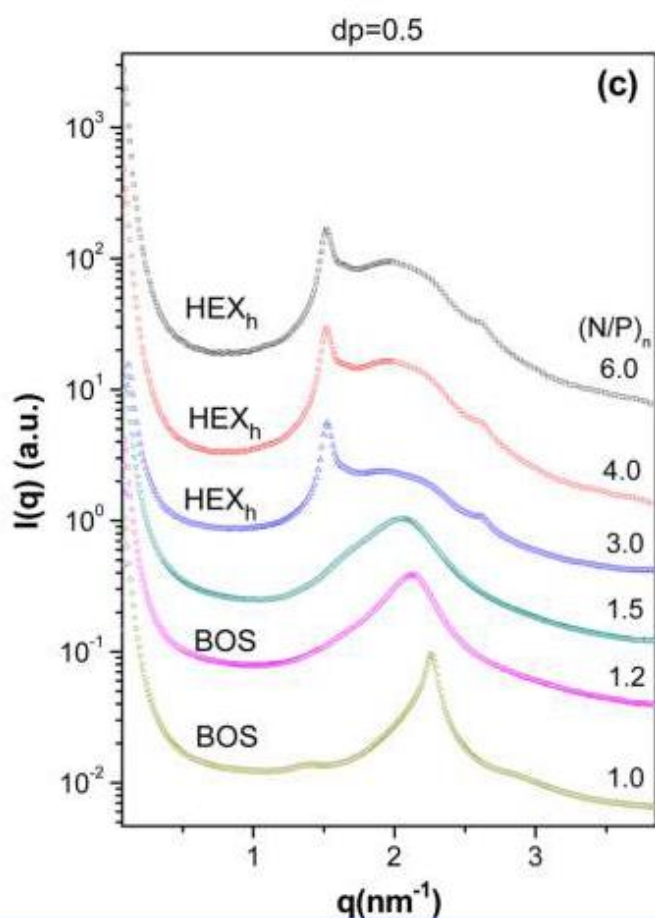


**Figure 6.15** The SAXS profiles of dendriplexes as  $dp=0.5$  at different N/P ratios. (Reprint from reference: Yang, Cheng-Che et al. *Macromolecules* **2014** 47 page: 3123)

## 6.5 Conclusions

In this chapter, we have discussed a detailed study of the colloidal and structural studies of DNA complexes made with G4 PAMAM and zwitterionically modified G4

PAMAM (zPAMAM). We show that the percent modification can tune the dendrimer: DNA interactions systematically resulting in more zPAMAM required to fully condense DNA. As well, the addition of surface carboxylic acids, results in dendriplexes which fall apart more rapidly in the presence of a competitor. Promisingly for potential in vivo applications, the colloidal properties of the PAMAM: DNA and zPAMAM: DNA are nearly identical.

The internal packaging of the PAMAM and zPAMAM dendriplexes are complex and consistent primarily with two possible phases being observed dependent on the system conditions. A high  $Q$  phase with tight DNA packaging that is kinetically stable is observed. The DNA-DNA spacings are comparable to many hexagonally packaged DNA condensed by linear cations ( $D_{Br} \sim 30 \text{ \AA}$ ). Under some conditions, a low  $Q$  phase consistent with a much more open packaging ( $D_{Br} \sim 42 \text{ \AA}$ ) is also observed. We show a number of means to tune the packaging between these phases including different condensation preparation methods and pH. Interestingly, the zPAMAM appears to favor the tighter packaging form for low percent modification but shifts to the more open structure at high percent modification. The resulting phase behavior of these complexes at a given salt concentration do not show a significant dependence on percent modification, however, large substitution of the primary surface amines of PAMAM to carboxylic acids does result in the zPAMAM complexes dissolving at lower total salt concentration.

## Chapter 7 Summary and Future Perspective

Dendrimers are synthetic macromolecules with highly branched and symmetric architecture. Their specific properties including their molecular chain architecture, monodisperse molecular weight, tunable shape and high number of functional surface groups has made dendrimers appealing for potential use in a wide array of application in the biomedical and therapeutic fields. Cationic dendrimers, such as polyamidoamine (PAMAM), have been investigated for their potential as gene delivery vectors due to their ability to condense DNA and protect it from nuclease enzymes.

Almost any cation of charge +3 and higher can induce DNA compaction. The physical mechanisms responsible for DNA condensation are still not fully understood. While electrostatics are known to be involved, a mean-field theory does not explain the observed attractions in DNA condensation. To account for the attractions driving DNA condensation that are experimentally observed, more recent theoretical treatments require a correlation of charges or water structuring between apposing DNA helices. A convenient model for discussing correlations is the electrostatic zipper model which postulates that cationic charges bind in the grooves of DNA leading to attractive interhelical correlations between the bound positive charges and the apposing helices. Experimental studies have suggested such groove binding is present in a variety of linear polycations; although there is some disagreement between which grooves the cations sit. Hyperbranched polycations, such as polycationic dendrimers, presumably would not be able to bind to DNA and correlate their charges in the same manner as linear cations.

In Chapter 4, using osmotic stress combined with SAXS, we have examined the DNA–DNA intermolecular forces in low generation (G0/G1) PAMAM dendrimer condensed DNA assemblies. These PAMAM/DNA assemblies were compared to comparably charge (+4/+8) linear arginine peptides and we display significantly different physical behavior than linear cation–DNA assemblies. In homologous linear

cation systems, DNA-DNA repulsions are independent of length and the attractions scale inversely with the charge. For PAMAM, however, we see that the attractions are increase with generation number and the attractions only slightly increase in going from +4 to +8. Combined, these forces result in tighter binding for linear cations with increased charge but more loose binding in the dendrimer systems.

In Chapter 5, we examine the role of pH on G0/G1 PAMAM/DNA assemblies. The primary amines at the surface of PAMA only accounts for some of the total amines in the molecule. In the interior of the dendrimer, there are a number of secondary and tertiary amines with unique  $pK_a$ 's. Therefore, altering the pH changes the total net charge of the PAMAM. Focusing on the effect of pH on the forces, we show that for a given dendriplex system, despite starting at very different interaxial spacings at equilibrium, both G0- and G1-PAMAM condensed DNA converge to the same high pressure limit for all pHs studied. By separating and quantifying the attractive and repulsive free energy contributions, we show that repulsions for a given PAMAM generation are nearly unaffected by pH while the observed attractions scale approximately linearly with the inverse of the dendrimer charge. This is comparable to the charge dependence of the attractive force in homologous linear cations. Changes in the pH at condensation also greatly influence the resulting phase behavior for G0/G1 PAMAM dendriplexes. Together, our results suggest that pH and salt play a central role in tuning the intermolecular forces and packaging within the PAMAM/DNA condensed phase.

In chapter 6, we changed our focus to addressing potential applications of PAMAM for gene delivery. Gene delivery polymers must be designed to perform numerous functions. In particular, the materials must bind and condense DNA to protect it from extra- and intracellular nucleases and to facilitate cellular internalization. Yet, such materials must also release their DNA cargo to allow transcription. In addition excess free polycation is essential to forming sufficiently small stable nanoparticles for cellular uptake yet the presence of free polycation itself

has toxic effects on the cells. With this in mind, we proposed the synthesis of zwitterionic PAMAM (zPAMAM) to potential create dendriplexes with tunable dendrimer-DNA interactions to control compaction and release. In addition, zPAMAM is anticipated to have reduced cellular toxicities. Our focus here is to examine the condensation and release of zPAMAM and compare the DNA packaging that occurs in zPAMAM compared to condensation by unmodified PAMAM. It is known that middle to high generation PAMAM is required for efficient nucleic acid transport, so we focused on G4 PAMAM either unmodified or modified with succinic anhydride to replace some of the primary surface amines with carboxyl moieties. We show that zPAMAM as high as 40% modified has no problem fully condensing DNA and that DNA release is dependent on the percent modification of the polymer. DLS studies show the zPAMAM can form comparably sized DNA nanoparticles to the unmodified PAMAM at the same weight ratio.

The internal structures of the G4 PAMAM/DNA assemblies is complex but mostly shows the presence of two different structures represented by a low and high  $Q$  Bragg reflection as described in Chapter 6. While our scattering studies do not allow for exact lattice determination, we see that the low  $Q$ , or more loosely packaged DNA phase, is similar to previously reported bead on a string (BOS) or possibly square columnar phases. The higher  $Q$ , more tightly packaged phase is comparable in DNA-DNA spacings to suggest hexagonal packaging of the DNA helices. We show using sample preparation methods and pH that the ratio of these two phases can be tuned. In addition, the presence of negatively charged moieties in the zPAMAM appears to shift the DNA packaging from the hexagonal phase to a structure like BOS. zPAMAM also affects the resulting salt sensitivities of the dendriplexes principally by changing the critical salt concentration required for dissolution.

Although we have shown some studies in the structures of these zPAMAM/DNA complexes by SAXS, there are still some questions remain to be solved. The limited  $Q$  range and intensity do not allow for a more detailed understanding of the exact

lattice for G4-PAMAM/DNA and zPAMAM/DNA complexes. Previously published studies have reported different phases and scattering profiles, which differ from each other as well as from our own studies. Future work using synchrotron SAXS or small-angle neutron scattering (SANS) could shed more light on the exact nature of these phases. In X-ray work the scattering is almost exclusively dominated by the DNA due to the electron density in the phosphates. SANS may allow for the visualization of both the DNA and the dendrimers inside the complex through phase contrast matching using D<sub>2</sub>O or H<sub>2</sub>O/D<sub>2</sub>O mixtures. Such approaches have been done for DNA-protein complexes and dendrimers would presumably have scattering densities comparable to protein. A drawback to SANS is the need for significantly larger sample volumes for sufficient scattering counts.

As discussed in the introduction of Chapter 6, we hypothesized that zPAMAM may have promise as a new type of gene delivery system due to its potential to simultaneously modulate dendrimer-DNA interactions as well as decrease inherent cytotoxicity of the polycation. Future work should focus on the examination of zPAMAM as a nucleic acid delivery system. Preliminary results have already suggested that zPAMAM does indeed show a significant reduction in the cell cytotoxicity compared to unmodified PAMAM (data not shown), but the actual transfection efficiency or DNA uptake from zPAMAM dendriplexes is unknown and should be optimized and studied. One of the advantages of the dendrimers is its high number of surface groups and ease in changing the molecular chemistry. It would be straight forward to examine how changing the chemistry of the anion would affect the zPAMAMs ability to condense DNA. Structural studies and cell studies could be performed to assess how variations in the chemistry of the anionic moieties affect structure as well as cell toxicity and transfection efficacy. Some studies have shown that PAMAM condensed DNA is time-limited in its ability to protect DNA from nuclease digestion.<sup>14,175-179</sup> Presumably the more loosely packaging resulting in zPAMAM will also affect the ability of zPAMAM to protect its cargo. It will be important for applications of zPAMAM for gene uptake by cells, to examine the

ability of zPAMAM to protect nucleic acids from nuclease attack and its time course. Lastly, the zwitterionic approach could easily be adapted for other commercial transfection systems such as polyethyleneimine (PEI) to form zPEI. Structural studies in conjunction with cell transfection for zPEI/DNA could be very instructive for determining structure-function activities in polyplexes. zPEI may not suffer from some of the non-equilibrium states observed in the high generation PAMAM studies described here.

## Reference

- (1) Klajnert, B.; Bryszewska, M. Dendrimers: properties and applications. *Acta Biochim Pol* **2001**, *48*, 199-208.
- (2) Abbasi, E.; Aval, S. F.; Akbarzadeh, A.; Milani, M.; Nasrabadi, H. T.; Joo, S. W.; Hanifehpour, Y.; Nejati-Koshki, K.; Pashaei-Asl, R. Dendrimers: synthesis, applications, and properties. *Nanoscale Research Letters* **2014**, *9*.
- (3) Tomalia, D. A.; Baker, H.; Dewald, J.; Hall, M.; Kallos, G.; Martin, S.; Roeck, J.; Ryder, J.; Smith, P. A New Class of Polymers: Starburst-Dendritic Macromolecules. *Polym J* **1985**, *17*, 117-132.
- (4) Esfand, R.; Tomalia, D. A. Poly(amidoamine) (PAMAM) dendrimers: from biomimicry to drug delivery and biomedical applications. *Drug Discovery Today* **2001**, *6*, 427-436.
- (5) Stojanovic, N.; Murphy, L. D.; Wagner, B. D. Fluorescence-Based Comparative Binding Studies of the Supramolecular Host Properties of PAMAM Dendrimers Using Anilinonaphthalene Sulfonates: Unusual Host-Dependent Fluorescence Titration Behavior. *Sensors* **2010**, *10*, 4053-4070.
- (6) Kobayashi, H.; Kawamoto, S.; Jo, S.-K.; Bryant, H. L.; Brechbiel, M. W.; Star, R. A. Macromolecular MRI Contrast Agents with Small Dendrimers: Pharmacokinetic Differences between Sizes and Cores. *Bioconjugate Chemistry* **2003**, *14*, 388-394.
- (7) Kalish, H.; Arbab, A. S.; Miller, B. R.; Lewis, B. K.; Zywicke, H. A.; Bulte, J. W. M.; Bryant, L. H.; Frank, J. A. Combination of transfection agents and magnetic resonance contrast agents for cellular imaging: Relationship between relaxivities, electrostatic forces, and chemical composition. *Magnetic Resonance in Medicine* **2003**, *50*, 275-282.
- (8) Barth, R. F.; Adams, D. M.; Soloway, A. H.; Alam, F.; Darby, M. V. Boronated starburst dendrimer-monoclonal antibody immunoconjugates: Evaluation as a potential delivery system for neutron capture therapy. *Bioconjugate Chemistry* **1994**, *5*, 58-66.
- (9) Solassol, J.; Crozet, C.; Perrier, V.; Leclaire, J.; Beranger, F.; Caminade, A. M.; Meunier, B.; Dormont, D.; Majoral, J. P.; Lehmann, S. Cationic phosphorus-containing dendrimers reduce prion replication both in cell culture and in mice infected with scrapie. *The Journal of general virology* **2004**, *85*, 1791-1799.
- (10) Abderrezak, A.; Bourassa, P.; Mandeville, J.-S.; Sedaghat-Herati, R.; Tajmir-Riahi, H.-A. Dendrimers Bind Antioxidant Polyphenols and cisPlatin Drug. *Plos One* **2012**, *7*.
- (11) Agrawal, P.; Gupta, U.; Jain, N. K. Glycoconjugated peptide dendrimers-based nanoparticulate system for the delivery of chloroquine phosphate. *Biomaterials* **2007**, *28*, 3349-3359.
- (12) Shukla, R.; Hill, E.; Shi, X.; Kim, J.; Muniz, M. C.; Sun, K.; Baker, J. R., Jr. Tumor microvasculature targeting with dendrimer-entrapped gold nanoparticles. *Soft Matter* **2008**, *4*, 2160-2163.

- (13) Fant, K.; Esbjorner, E. K.; Lincoln, P.; Norden, B. DNA condensation by PAMAM dendrimers: Self-assembly characteristics and effect on transcription. *Biochemistry* **2008**, *47*, 1732-1740.
- (14) Ainalem, M.-L.; Bartles, A.; Muck, J.; Dias, R. S.; Carnerup, A. M.; Zink, D.; Nylander, T. DNA Compaction Induced by a Cationic Polymer or Surfactant Impact Gene Expression and DNA Degradation. *Plos One* **2014**, *9*.
- (15) Ainalem, M.-L.; Nylander, T. DNA condensation using cationic dendrimers-morphology and supramolecular structure of formed aggregates. *Soft Matter* **2011**, *7*, 4577-4594.
- (16) Pack, D. W.; Hoffman, A. S.; Pun, S.; Stayton, P. S. Design and development of polymers for gene delivery. *Nature reviews. Drug discovery* **2005**, *4*, 581-593.
- (17) Kay, M. A.; Glorioso, J. C.; Naldini, L. Viral vectors for gene therapy: the art of turning infectious agents into vehicles of therapeutics. *Nat Med* **2001**, *7*, 33-40.
- (18) Abdelhady, H. G.; Lin, Y.-L.; Sun, H.; ElSayed, M. E. H. Visualizing the Attack of RNase Enzymes on Dendriplexes and Naked RNA Using Atomic Force Microscopy. *Plos One* **2013**, *8*.
- (19) Tian, W. D.; Ma, Y. Q. Theoretical and computational studies of dendrimers as delivery vectors. *Chem Soc Rev* **2013**, *42*, 705-727.
- (20) Bloomfield, V. A. DNA condensation by multivalent cations. *Biopolymers* **1997**, *44*, 269-282.
- (21) Bloomfield, V. A. DNA condensation. *Current Opinion in Structural Biology* **1996**, *6*, 334-341.
- (22) Mills, M.; Orr, B. G.; Holl, M. M. B.; Andricioaei, I. Attractive Hydration Forces in DNA-Dendrimer Interactions on the Nanometer Scale. *Journal of Physical Chemistry B* **2013**, *117*, 973-981.
- (23) Kornyshev, A. A.; Leikin, S. Electrostatic zipper motif for DNA aggregation. *Physical Review Letters* **1999**, *82*, 4138-4141.
- (24) Kornyshev, A. A.; Lee, D. J.; Leikin, S.; Wynveen, A. Structure and interactions of biological helices. *Reviews of Modern Physics* **2007**, *79*, 943-996.
- (25) Rau, D. C.; Parsegian, V. A. DIRECT MEASUREMENT OF THE INTERMOLECULAR FORCES BETWEEN COUNTERION-CONDENSED DNA DOUBLE HELICES - EVIDENCE FOR LONG-RANGE ATTRACTIVE HYDRATION FORCES. *Biophysical Journal* **1992**, *61*, 246-259.
- (26) Chen, C.-Y.; Su, C.-J.; Peng, S.-F.; Chen, H.-L.; Sung, H.-W. Dendrimer-induced DNA bending. *Soft Matter* **2011**, *7*, 61-63.
- (27) Chun-Jen, S.; Chun-Yu, C.; Hsin-Lung, C.; Viktor, A. I. Beads-on-String Structure of the Electrostatic Complex of DNA with a High-Generation PAMAM Dendrimer. *Journal of Physics: Conference Series* **2011**, *272*, 012002.
- (28) Yang, C.-C.; Huang, Y.-C.; Chen, C.-Y.; Su, C.-J.; Chen, H.-L.; Ivanov, V. A. Structure of the Electrostatic Complex of DNA with Cationic Dendrimer of Intermediate Generation: The Role of Counterion Entropy. *Macromolecules* **2014**, *47*, 3117-3127.

- (29) Hikal, W. M.; Harmon, H. J. Crystal-growth inhibition of solid porphyrin micro-crystals by G4 PAMAM dendrimer. *Journal of Materials Science* **2011**, *46*, 2273-2280.
- (30) Jimena Prieto, M.; Facundo Temprana, C.; del Rio Zabala, N. E.; Hernan Marotta, C.; del Valle Alonso, S. Optimization and in vitro toxicity evaluation of G4 PAMAM dendrimer-risperidone complexes. *European Journal of Medicinal Chemistry* **2011**, *46*, 845-850.
- (31) Bienert, R.; Emmerling, F.; Thunemann, A. F. The size distribution of 'gold standard' nanoparticles. *Analytical and bioanalytical chemistry* **2009**, *395*, 1651-1660.
- (32) Chaudhary, G. R.; Singh, P.; Kaur, G.; Mehta, S. K.; Kumar, S.; Dilbaghi, N. Multifaceted approach for the fabrication of metallomicelles and metallic nanoparticles using solvophobic bisdodecylaminepalladium (II) chloride as precursor. *Inorganic chemistry* **2015**, *54*, 9002-9012.
- (33) Caracciolo, G.; Pozzi, D.; Amenitsch, H.; Caminiti, R. Multicomponent cationic lipid-DNA complex formation: role of lipid mixing. *Langmuir : the ACS journal of surfaces and colloids* **2005**, *21*, 11582-11587.
- (34) Balakrishnan, S.; Javid, N.; Weingartner, H.; Winter, R. Small-angle X-ray scattering and near-infrared vibrational spectroscopy of water confined in aerosol-OT reverse micelles. *Chemphyschem : a European journal of chemical physics and physical chemistry* **2008**, *9*, 2794-2801.
- (35) Bota, A.; Varga, Z.; Goerigk, G. Biological systems as nanoreactors: anomalous small-angle scattering study of the CdS nanoparticle formation in multilamellar vesicles. *The journal of physical chemistry. B* **2007**, *111*, 1911-1915.
- (36) Schneidman-Duhovny, D.; Kim, S. J.; Sali, A. Integrative structural modeling with small angle X-ray scattering profiles. *Bmc Struct Biol* **2012**, *12*.
- (37) Parsegian, V. A.; Rand, R. P.; Fuller, N. L.; Rau, D. C. OSMOTIC-STRESS FOR THE DIRECT MEASUREMENT OF INTERMOLECULAR FORCES. *Methods in Enzymology* **1986**, *127*, 400-416.
- (38) Tristram-Nagle, S. Use of X-Ray and Neutron Scattering Methods with Volume Measurements to Determine Lipid Bilayer Structure and Number of Water Molecules/Lipid. *Sub-cellular biochemistry* **2015**, *71*, 17-43.
- (39) Roe, R.-J.: *Basics of X-ray and Neutron Scattering*; 1 ed.; Oxford University Press: New York, 2000. pp. 1.
- (40) Massa, W.: *Crystal structure determination*; Springer New York, 2004. pp. 13-23.
- (41) Roe, R.-J.: *Methods of X-ray and Neutron Scattering in Polymer Science*; Oxford University Press: New York 2000. pp. 82-139.
- (42) Lee, B.; Lo, C.-T.; Seifert, S.; Winans, R. E. Silver behenate as a calibration standard of grazing-incidence small-angle X-ray scattering. *Journal of applied crystallography* **2006**, *39*, 749-751.
- (43) Knaapila, M.; Svensson, C.; Barauskas, J.; Zackrisson, M.; Nielsen, S. S.; Toft, K. N.; Vestergaard, B.; Arleth, L.; Olsson, U.; Pedersen, J. S.; Cerenius, Y. A

new small-angle X-ray scattering set-up on the crystallography beamline I711 at MAX-lab. *Journal of synchrotron radiation* **2009**, *16*, 498-504.

(44) McIntosh, T. J.; Magid, A. D.; Simon, S. A. Repulsive interactions between uncharged bilayers. Hydration and fluctuation pressures for monoglycerides. *Biophysical journal* **1989**, *55*, 897-904.

(45) Millman, B. M.; Racey, T. J.; Matsubara, I. Effects of hyperosmotic solutions on the filament lattice of intact frog skeletal muscle. *Biophysical journal* **1981**, *33*, 189-202.

(46) Pratt, D. V. J. G. V. C. W.: *Fundamentals of Biochemistry: Life at the Molecular Level*; 4 ed.; John Wiley & Sons. Inc., 2015. pp. 30-38.

(47) Borg, F. What is osmosis? Explanation and understanding of a physical phenomenon. **2003**.

(48) Atkins, P. W.: *Physical Chemistry*; Oxford University Press, 2010. pp. 150-156.

(49) ELiTechGroup: VAPOR PRESSURE OSMOMETER Model 5600 user's manual. 2010.

(50) Stanley, C. B.; Strey, H. H. Measuring Osmotic Pressure of Poly(ethylene glycol) Solutions by Sedimentation Equilibrium Ultracentrifugation. *Macromolecules* **2003**, *36*, 6888-6893.

(51) DeRouchey, J.; Parsegian, V. A.; Rau, D. C. Cation Charge Dependence of the Forces Driving DNA Assembly. *Biophysical Journal* **2010**, *99*, 2608-2615.

(52) DeRouchey, J.; Hoover, B.; Rau, D. C. A Comparison of DNA Compaction by Arginine and Lysine Peptides: A Physical Basis for Arginine Rich Protamines. *Biochemistry* **2013**, *52*, 3000-3009.

(53) DeRouchey, J. E.; Rau, D. C. Role of amino acid insertions on intermolecular forces between arginine peptide condensed DNA helices: implications for protamine-DNA packaging in sperm. *The Journal of biological chemistry* **2011**, *286*, 41985-41992.

(54) DeRouchey, J. E.; Rau, D. C. Salt Effects on Condensed Protamine–DNA Assemblies: Anion Binding and Weakening of Attraction. *The Journal of Physical Chemistry B* **2011**, *115*, 11888-11894.

(55) DeRouchey, J.; Netz, R. R.; Radler, J. O. Structural investigations of DNA-polycation complexes. *European Physical Journal E* **2005**, *16*, 17-28.

(56) DeRouchey, J.; Parsegian, V. A.; Rau, D. C. Cation charge dependence of the forces driving DNA assembly. *Biophysical journal* **2010**, *99*, 2608-2615.

(57) Bielinska, A. U.; Chen, C.; Johnson, J.; Baker, J. R. DNA Complexing with Polyamidoamine Dendrimers: Implications for Transfection. *Bioconjugate Chemistry* **1999**, *10*, 843-850.

(58) Eichman, J. D.; Bielinska, A. U.; Kukowska-Latallo, J. F.; Baker Jr, J. R. The use of PAMAM dendrimers in the efficient transfer of genetic material into cells. *Pharmaceutical Science & Technology Today* **2000**, *3*, 232-245.

(59) Pack, D. W.; Hoffman, A. S.; Pun, S.; Stayton, P. S. Design and development of polymers for gene delivery. *Nat Rev Drug Discov* **2005**, *4*, 581-593.

- (60) Dufes, C.; Uchegbu, I. F.; Schatzlein, A. G. Dendrimers in gene delivery. *Advanced Drug Delivery Reviews* **2005**, *57*, 2177-2202.
- (61) Kunze, K. K.; Netz, R. R. Salt-induced DNA-histone complexation. *Phys Rev Lett* **2000**, *85*, 4389-4392.
- (62) Jonsson, M.; Linse, P. Polyelectrolyte–macroion complexation. II. Effect of chain flexibility. *The Journal of Chemical Physics* **2001**, *115*, 10975-10985.
- (63) Evans, H. M.; Ahmad, A.; Ewert, K.; Pfohl, T.; Martin-Herranz, A.; Bruinsma, R. F.; Safinya, C. R. Structural polymorphism of DNA-dendrimer complexes. *Physical Review Letters* **2003**, *91*, 075501.
- (64) Liu, Y.-C.; Chen, H.-L.; Su, C.-J.; Lin, H.-K.; Liu, W.-L.; Jeng, U. S. Mesomorphic Complexes of Poly(amidoamine) Dendrimer with DNA. *Macromolecules* **2005**, *38*, 9434-9440.
- (65) Dootz, R.; Otten, A.; Koster, S.; Struth, B.; Pfohl, T. Evolution of DNA compaction in microchannels. *Journal of Physics-Condensed Matter* **2006**, *18*, S639-S652.
- (66) Pfohl, T.; Otten, A.; Köster, S.; Dootz, R.; Struth, B.; Evans, H. M. Highly Packed and Oriented DNA Mesophases Identified Using in Situ Microfluidic X-ray Microdiffraction. *Biomacromolecules* **2007**, *8*, 2167-2172.
- (67) Carnerup, A. M.; Ainalem, M.-L.; Alfredsson, V.; Nylander, T. Condensation of DNA using poly(amido amine) dendrimers: effect of salt concentration on aggregate morphology. *Soft Matter* **2011**, *7*, 760-768.
- (68) Dootz, R.; Toma, A. C.; Pfohl, T. PAMAM6 dendrimers and DNA: pH dependent "beads-on-a-string" behavior revealed by small angle X-ray scattering. *Soft Matter* **2011**, *7*, 8343-8351.
- (69) Froehlich, E.; Mandeville, J. S.; Weinert, C. M.; Kreplak, L.; Tajmir-Riahi, H. A. Bundling and Aggregation of DNA by Cationic Dendrimers. *Biomacromolecules* **2011**, *12*, 511-517.
- (70) Ritort, F.; Mihardja, S.; Smith, S. B.; Bustamante, C. Condensation Transition in DNA-Polyaminoamide Dendrimer Fibers Studied Using Optical Tweezers. *Physical Review Letters* **2006**, *96*, 118301.
- (71) Fant, K.; Esbjörner, E. K.; Lincoln, P.; Nordén, B. DNA Condensation by PAMAM Dendrimers: Self-Assembly Characteristics and Effect on Transcription†. *Biochemistry* **2008**, *47*, 1732-1740.
- (72) Lee, I.; Athey, B. D.; Wetzal, A. W.; Meixner, W.; Baker, J. R. Structural molecular dynamics studies on polyamidoamine dendrimers for a therapeutic application: Effects of pH and generation. *Macromolecules* **2002**, *35*, 4510-4520.
- (73) Rau, D. C.; Parsegian, V. A. Direct measurement of the intermolecular forces between counterion-condensed DNA double helices - Evidence for long-range attractive hydration forces. *Biophys. J.* **1992**, *61*, 246-259.
- (74) Raspaud, E.; Olvera de la Cruz, M.; Sikorav, J. L.; Livolant, F. Precipitation of DNA by Polyamines: A Polyelectrolyte Behavior. *Biophysical Journal* **1998**, *74*, 381-393.

- (75) Conwell, C. C.; Vilfan, I. D.; Hud, N. V. Controlling the size of nanoscale toroidal DNA condensates with static curvature and ionic strength. *Proceedings of the National Academy of Sciences* **2003**, *100*, 9296-9301.
- (76) Yang, J.; Rau, D. C. Incomplete Ion Dissociation Underlies the Weakened Attraction between DNA Helices at High Spermidine Concentrations. *Biophysical Journal* **2005**, *89*, 1932-1940.
- (77) Todd, B. A.; Parsegian, V. A.; Shirahata, A.; Thomas, T. J.; Rau, D. C. Attractive forces between cation condensed DNA double helices. *Biophysical Journal* **2008**, *94*, 4775-4782.
- (78) DeRouchey, J. E.; Parsegian, V. A.; Rau, D. C. Cation Charge Dependence of the Forces Driving DNA Assembly. *Biophysical Journal* **2010**, *99*, 2608-2615.
- (79) DeRouchey, J. E.; Rau, D. C. Salt effects on condensed protamine-DNA assemblies: anion binding and weakening of attraction. *J Phys Chem B* **2011**, *115*, 11888-11894.
- (80) DeRouchey, J. E.; Hoover, B.; Rau, D. C. A comparison of DNA compaction by arginine and lysine peptides: a physical basis for arginine rich protamines. *Biochemistry* **2013**, *52*, 3000-3009.
- (81) Wilson, R. W.; Bloomfield, V. A. Counterion-induced condensation of deoxyribonucleic acid. a light-scattering study. *Biochemistry* **1979**, *18*, 2192-2196.
- (82) Pelta, J.; Livolant, F.; Sikorav, J. L. DNA aggregation induced by polyamines and cobalthexammine. *J. Biol. Chem.* **1996**, *271*, 5656-5662.
- (83) Gelbart, W. M.; Bruinsma, R. F.; Pincus, P. A.; Parsegian, V. A. DNA-Inspired Electrostatics. *Phys. Today* **2000**, *53*, 38-44.
- (84) Rouzina, I.; Bloomfield, V. A. Macroion Attraction Due to Electrostatic Correlation between Screening Counterions. 1. Mobile Surface-Adsorbed Ions and Diffuse Ion Cloud. *The Journal of Physical Chemistry* **1996**, *100*, 9977-9989.
- (85) Ha, B. Y.; Liu, A. J. Counterion-Mediated Attraction between Two Like-Charged Rods. *Physical Review Letters* **1997**, *79*, 1289-1292.
- (86) Shklovskii, B. I. Wigner crystal model of counterion induced bundle formation of rodlike polyelectrolytes. *Phys Rev Lett* **1999**, *82*, 3268-3271.
- (87) Kornyshev, A. A.; Leikin, S. Electrostatic interaction between helical macromolecules in dense aggregates: An impetus for DNA poly- and mesomorphism. *Proceedings of the National Academy of Sciences of the United States of America* **1998**, *95*, 13579-13584.
- (88) Kornyshev, A. A.; Lee, D. J.; Leikin, S.; Wynveen, A. Structure and interactions of biological helices. *Reviews of Modern Physics* **2007**, *79*, 943-996.
- (89) Fita, I.; Campos, J. L.; Puigjaner, L. C.; Subirana, J. A. X-Ray-Diffraction Study of DNA Complexes with Arginine Peptides and Their Relation to Nucleoprotamine Structure. *Journal of Molecular Biology* **1983**, *167*, 157-177.
- (90) Feuerstein, B. G.; Pattabiraman, N.; Marton, L. J. Molecular mechanics of the interactions of spermine with DNA: DNA bending as a result of ligand binding. *Nucleic Acids Research* **1990**, *18*, 1271-1282.

- (91) Hud, N. V.; Milanovich, F. P.; Balhorn, R. EVIDENCE OF NOVEL SECONDARY STRUCTURE IN DNA-BOUND PROTAMINE IS REVEALED BY RAMAN-SPECTROSCOPY. *Biochemistry* **1994**, *33*, 7528-7535.
- (92) Ruiz-Chica, J.; Medina, M. A.; Sanchez-Jimenez, F.; Ramirez, F. J. Fourier transform Raman study of the structural specificities on the interaction between DNA and biogenic polyamines. *Biophys J* **2001**, *80*, 443-454.
- (93) Ouameur, A. A.; Tajmir-Riahi, H. A. Structural analysis of DNA interactions with biogenic polyamines and cobalt(III) hexamine studied by Fourier transform infrared and capillary electrophoresis. *The Journal of biological chemistry* **2004**, *279*, 42041-42054.
- (94) Boroudjerdi, H.; Netz, R. R. Interactions between polyelectrolyte-macroion complexes. *EPL (Europhysics Letters)* **2003**, *64*, 413.
- (95) Netz, R. R.; Joanny, J.-F. Adsorption of Semiflexible Polyelectrolytes on Charged Planar Surfaces: Charge Compensation, Charge Reversal, and Multilayer Formation. *Macromolecules* **1999**, *32*, 9013-9025.
- (96) Mills, M.; Orr, B.; Holl, M. M. B.; Andricioaei, I. Microscopic Basis for the Mesoscopic Extensibility of Dendrimer-Compacted DNA. *Biophysical Journal* **2010**, *98*, 834-842.
- (97) Podgornik, R.; Licer, M. Polyelectrolyte bridging interactions between charged macromolecules. *Current Opinion in Colloid & Interface Science* **2006**, *11*, 273-279.
- (98) McGhee, J. D.; Wood, W. I.; Dolan, M.; Engel, J. D.; Felsenfeld, G. A 200-BASE PAIR REGION AT THE 5' END OF THE CHICKEN ADULT BETA-GLOBIN GENE IS ACCESSIBLE TO NUCLEASE DIGESTION. *Cell* **1981**, *27*, 45-55.
- (99) Korolev, N.; Berezhnoy, N. V.; Eom, K. D.; Tam, J. P.; Nordenskiöld, L. A universal description for the experimental behavior of salt-(in)dependent oligocation-induced DNA condensation. *Nucleic Acids Research* **2009**, *37*, 7137-7150.
- (100) Nayvelt, I.; Thomas, T.; Thomas, T. J. Mechanistic differences in DNA nanoparticle formation in the presence of oligolysines and poly-L-lysine. *Biomacromolecules* **2007**, *8*, 477-484.
- (101) Cakara, D.; Kleimann, J.; Borkovec, M. Microscopic Protonation Equilibria of Poly(amidoamine) Dendrimers from Macroscopic Titrations. *Macromolecules* **2003**, *36*, 4201-4207.
- (102) Fita, I.; Campos, J. L.; Puigjaner, L. C.; Subirana, J. A.; Luzzati, V. X-ray diffraction study of DNA complexes with arginine peptides and their relation to nucleoprotamine structure. *Journal of Molecular Biology* **1983**, *167*, 157-177.
- (103) Hud, N. V.; Milanovich, F. P.; Balhorn, R. Evidence of Novel Secondary Structure in DNA-Bound Protamine Is Revealed by Raman Spectroscopy. *Biochemistry* **1994**, *33*, 7528-7535.

- (104) Ruiz-Chica, J.; Medina, M. A.; Sanchez-Jimenez, F.; Ramirez, F. J. Fourier transform Raman study of the structural specificities on the interaction between DNA and biogenic polyamines. *Biophysical Journal* **2001**, *80*, 443-454.
- (105) Ouameur, A. A.; Tajmir-Riahi, H.-A. Structural Analysis of DNA Interactions with Biogenic Polyamines and Cobalt(III)hexamine Studied by Fourier Transform Infrared and Capillary Electrophoresis. *Journal of Biological Chemistry* **2004**, *279*, 42041-42054.
- (106) Boroudjerdi, H.; Netz, R. R. Interactions between polyelectrolyte-macroion complexes. *Europhysics Letters* **2003**, *64*, 413-419.
- (107) Mills, M.; Orr, B. G.; Banaszak Holl, M. M.; Andricioaei, I. Attractive Hydration Forces in DNA–Dendrimer Interactions on the Nanometer Scale. *The Journal of Physical Chemistry B* **2013**, *117*, 973-981.
- (108) Mills, M.; Orr, B.; Banaszak Holl, M. M.; Andricioaei, I. Microscopic Basis for the Mesoscopic Extensibility of Dendrimer-Compacted DNA. *Biophysical Journal* **2010**, *98*, 834-842.
- (109) Wilson, R. W.; Bloomfield, V. A. Counterion-induced condensation of deoxyribonucleic acid. A light-scattering study. *Biochemistry* **1979**, *18*, 2192-2196.
- (110) Yin, H.; Kanasty, R. L.; Eltoukhy, A. A.; Vegas, A. J.; Dorkin, J. R.; Anderson, D. G. Non-viral vectors for gene-based therapy. *Nat Rev Genet* **2014**, *15*, 541-555.
- (111) Thomas, C. E.; Ehrhardt, A.; Kay, M. A. Progress and problems with the use of viral vectors for gene therapy. *Nat Rev Genet* **2003**, *4*, 346-358.
- (112) Niidome, T.; Huang, L. Gene therapy progress and prospects: Nonviral vectors. *Gene Therapy* **2002**, *9*, 1647-1652.
- (113) Garnett, M. C. Gene-Delivery Systems Using Cationic Polymers. **1999**, *16*, 61.
- (114) Nguyen, T. T.; Shklovskii, B. I. Complexation of DNA with positive spheres: Phase diagram of charge inversion and reentrant condensation. *Journal of Chemical Physics* **2001**, *115*, 7298-7308.
- (115) Qamhieh, K.; Nylander, T.; Ainalem, M.-L. Analytical Model Study of Dendrimer/DNA Complexes. *Biomacromolecules* **2009**, *10*, 1720-1726.
- (116) Tian, W.-d.; Ma, Y.-q. Complexation of a Linear Polyelectrolyte with a Charged Dendrimer: Polyelectrolyte Stiffness Effects. *Macromolecules* **2010**, *43*, 1575-1582.
- (117) Mogurampelly, S.; Nandy, B.; Netz, R.; Maiti, P. Elasticity of DNA and the effect of dendrimer binding. *Eur. Phys. J. E* **2013**, *36*, 1-9.
- (118) Qamhieh, K.; Nylander, T.; Black, C. F.; Attard, G. S.; Dias, R. S.; Ainalem, M.-L. Complexes formed between DNA and poly(amido amine) dendrimers of different generations - modelling DNA wrapping and penetration. *Physical Chemistry Chemical Physics* **2014**, *16*, 13112-13122.
- (119) Yu, S.; Li, M. H.; Choi, S. K.; Baker, J. R.; Larson, R. G. DNA Condensation by Partially Acetylated Poly(amido amine) Dendrimers: Effects of

Dendrimer Charge Density on Complex Formation. *Molecules* **2013**, *18*, 10707-10720.

(120) Su, C.-J.; Chen, C.-Y.; Lin, M.-C.; Chen, H.-L.; Iwase, H.; Koizumi, S.; Hashimoto, T. Nucleosome-like Structure from Dendrimer-Induced DNA Compaction. *Macromolecules* **2012**, *45*, 5208-5217.

(121) Shifrina, Z. B.; Kuchkina, N. V.; Rutkevich, P. N.; Vlasik, T. N.; Sushko, A. D.; Izumrudov, V. A. Water-Soluble Cationic Aromatic Dendrimers and Their Complexation with DNA. *Macromolecules* **2009**, *42*, 9548-9560.

(122) An, M.; Parkin, S. R.; DeRouchey, J. E. Intermolecular forces between low generation PAMAM dendrimer condensed DNA helices: role of cation architecture. *Soft Matter* **2014**, *10*, 590-599.

(123) Rau, D. C.; Parsegian, V. A. Direct measurement of the intermolecular forces between counterion-condensed DNA double helices. Evidence for long range attractive hydration forces. *Biophysical Journal* **1992**, *61*, 246-259.

(124) Todd, B. A.; Adrian Parsegian, V.; Shirahata, A.; Thomas, T. J.; Rau, D. C. Attractive Forces between Cation Condensed DNA Double Helices. *Biophysical Journal* **2008**, *94*, 4775-4782.

(125) McGhee, J. D.; Wood, W. I.; Dolan, M.; Engel, J. D.; Felsenfeld, G. A 200 base pair region at the 5' end of the chicken adult  $\beta$ -globin gene is accessible to nuclease digestion. *Cell* **1981**, *27*, 45-55.

(126) Parsegian, V. A.; Rand, R. P.; Fuller, N. L.; Rau, D. C.: [29] Osmotic stress for the direct measurement of intermolecular forces. In *Methods in Enzymology*; Lester, P., Ed.; Academic Press, 1986; Vol. Volume 127; pp 400-416.

(127) DeRouchey, J. E.; Rau, D. C. Role of Amino Acid Insertions on Intermolecular Forces between Arginine Peptide Condensed DNA Helices: IMPLICATIONS FOR PROTAMINE-DNA PACKAGING IN SPERM. *Journal of Biological Chemistry* **2011**, *286*, 41985-41992.

(128) Stanley, C.; Rau, D. C. Evidence for water structuring forces between surfaces. *Current Opinion in Colloid & Interface Science* **2011**, *16*, 551-556.

(129) Kornyshev, A. A.; Leikin, S. Electrostatic interaction between helical macromolecules in dense aggregates: An impetus for DNA poly- and meso-morphism. *Proceedings of the National Academy of Sciences* **1998**, *95*, 13579-13584.

(130) Lee, I.; Athey, B. D.; Wetzel, A. W.; Meixner, W.; Baker, J. R. Structural Molecular Dynamics Studies on Polyamidoamine Dendrimers for a Therapeutic Application: Effects of pH and Generation. *Macromolecules* **2002**, *35*, 4510-4520.

(131) Hastad, C. W.; Tokach, M. D.; Goodband, R. D.; Nellssen, J. L.; Dritz, S. S.; DeRouchey, J. M.; Jones, C. L. Comparison of yellow dent and NutriDense corn hybrids in swine diets. *J Anim Sci* **2005**, *83*, 2624-2631.

(132) Boswell, C. A.; Eck, P. K.; Regino, C. A. S.; Bernardo, M.; Wong, K. J.; Milenic, D. E.; Choyke, P. L.; Brechbiel, M. W. Synthesis, characterization, and biological evaluation of integrin  $\alpha(v)\beta(3)$ -targeted PAMAM dendrimers. *Molecular Pharmaceutics* **2008**, *5*, 527-539.

- (133) Bak, D. J.; Han, S. C.; Jin, S.-H.; Lee, J. W. Synthesis of Dendrimers via Sonogashira Coupling Reaction of Alkyne-focal Frechet Type Dendrons. *Bulletin of the Korean Chemical Society* **2011**, *32*, 3211-3212.
- (134) Arima, H.; Yamashita, S.; Mori, Y.; Hayashi, Y.; Motoyama, K.; Hattori, K.; Takeuchi, T.; Jono, H.; Ando, Y.; Hirayama, F.; Uekama, K. In Vitro and In Vivo gene delivery mediated by Lactosylated Dendrimer/alpha-Cyclodextrin Conjugates (G2) into Hepatocytes. *Journal of Controlled Release* **2010**, *146*, 106-117.
- (135) Daneshvar, N.; Abdullah, R.; Shamsabadi, F. T.; How, C. W.; Aizat, M. M. H.; Mehrbod, P. PAMAM dendrimer roles in gene delivery methods and stem cell research. *Cell Biology International* **2013**, *37*, 415-419.
- (136) Hemmer, R.; Hall, A.; Spaulding, R.; Rossow, B.; Hester, M.; Caroway, M.; Haskamp, A.; Wall, S.; Bullen, H. A.; Morris, C.; Haik, K. L. Analysis of Biotinylated Generation 4 Poly(amidoamine) (PAMAM) Dendrimer Distribution in the Rat Brain and Toxicity in a Cellular Model of the Blood-Brain Barrier. *Molecules* **2013**, *18*, 11537-11552.
- (137) Kumar, A.; Yellepeddi, V. K.; Vangara, K. K.; Strychar, K. B.; Palakurthi, S. Mechanism of gene transfection by polyamidoamine (PAMAM) dendrimers modified with ornithine residues. *Journal of Drug Targeting* **2011**, *19*, 770-780.
- (138) Shadrack, D. M.; Mubofu, E. B.; Nyandoro, S. S. Synthesis of Polyamidoamine Dendrimer for Encapsulating Tetramethylscutellarein for Potential Bioactivity Enhancement. *International Journal of Molecular Sciences* **2015**, *16*, 26363-26377.
- (139) Young Joo, C.; Su Jin, K.; Yang Jee, K.; Yong-beom, L.; Hai Won, C. Comparative studies on the genotoxicity and cytotoxicity of polymeric gene carriers polyethylenimine (PEI) and polyamidoamine (PAMAM) dendrimer in Jurkat T-cells. *Drug & Chemical Toxicology* **2010**, *33*, 357-366.
- (140) Zarebkohan, A.; Najafi, F.; Moghimi, H. R.; Hemmati, M.; Deevband, M. R.; Kazemi, B. Synthesis and characterization of a PAMAM dendrimer nanocarrier functionalized by SRL peptide for targeted gene delivery to the brain. *European Journal of Pharmaceutical Sciences* **2015**, *78*, 19-30.
- (141) Li, X.; Takashima, M.; Yuba, E.; Harada, A.; Kono, K. PEGylated PAMAM dendrimer-doxorubicin conjugate-hybridized gold nanorod for combined photothermal-chemotherapy. *Biomaterials* **2014**, *35*, 6576-6584.
- (142) He, H.; Li, Y.; Jia, X.-R.; Du, J.; Ying, X.; Lu, W.-L.; Lou, J.-N.; Wei, Y. PEGylated Poly(amidoamine) dendrimer-based dual-targeting carrier for treating brain tumors. *Biomaterials* **2011**, *32*, 478-487.
- (143) Zhu, S.; Hong, M.; Zhang, L.; Tang, G.; Jiang, Y.; Pei, Y. PEGylated PAMAM Dendrimer-Doxorubicin Conjugates: In Vitro Evaluation and In Vivo Tumor Accumulation. *Pharmaceutical Research* **2010**, *27*, 161-174.
- (144) Fant, K.; Esbjörner, E. K.; Jenkins, A.; Grossel, M. C.; Lincoln, P.; Nordén, B. Effects of PEGylation and Acetylation of PAMAM Dendrimers on DNA Binding, Cytotoxicity and in Vitro Transfection Efficiency. *Molecular Pharmaceutics* **2010**, *7*, 1734-1746.

- (145) Kolhatkar, R. B.; Kitchens, K. M.; Swaan, P. W.; Ghandehari, H. Surface Acetylation of Polyamidoamine (PAMAM) Dendrimers Decreases Cytotoxicity while Maintaining Membrane Permeability. *Bioconjugate Chemistry* **2007**, *18*, 2054-2060.
- (146) Yu, S.; Li, M.-H.; Choi, S.; Baker, J.; Larson, R. DNA Condensation by Partially Acetylated Poly(amido amine) Dendrimers: Effects of Dendrimer Charge Density on Complex Formation. *Molecules* **2013**, *18*, 10707.
- (147) Hunter, A. C.; Moghimi, S. M. Therapeutic synthetic polymers: a game of Russian roulette? *Drug Discovery Today* **2002**, *7*, 998.
- (148) Moghimi, S. M.; Symonds, P.; Murray, J. C.; Hunter, A. C.; Debska, G.; Szewczyk, A. A two-stage poly(ethylenimine)-mediated cytotoxicity: implications for gene transfer/therapy. *Molecular Therapy* **2005**, *11*, 990-995.
- (149) Rattan, R.; Vaidyanathan, S.; Wu, G. S. H.; Shakya, A.; Orr, B. G.; Banaszak Holl, M. M. Polyplex-Induced Cytosolic Nuclease Activation leads to Differential Transgene Expression. *Molecular pharmaceuticals* **2013**, *10*, 3013-3022.
- (150) Vaidyanathan, S.; Anderson, K. B.; Merzel, R. L.; Jacobovitz, B.; Kaushik, M. P.; Kelly, C. N.; van Dongen, M. A.; Dougherty, C. A.; Orr, B. G.; Banaszak Holl, M. M. Quantitative Measurement of Cationic Polymer Vector and Polymer-pDNA Polyplex Intercalation into the Cell Plasma Membrane. *ACS Nano* **2015**, *9*, 6097-6109.
- (151) Honig, D.; DeRouchey, J.; Jungmann, R.; Koch, C.; Plank, C.; Radler, J. O. Biophysical Characterization of Copolymer-Protected Gene Vectors. *Biomacromolecules* **2010**, *11*, 1802-1809.
- (152) Gabrielson, N. P.; Pack, D. W. Acetylation of polyethylenimine enhances gene delivery via weakened polymer/DNA interactions. *Biomacromolecules* **2006**, *7*, 2427-2435.
- (153) Forrest, M. L.; Meister, G. E.; Koerber, J. T.; Pack, D. W. Partial Acetylation of Polyethylenimine Enhances In Vitro Gene Delivery. *Pharmaceutical Research*, *21*, 365-371.
- (154) Xianghui, L.; Jennifer, W. Y.; David, M. L. Addition of "Charge-Shifting" Side Chains to Linear Poly(ethyleneimine) Enhances Cell Transfection Efficiency. *Biomacromolecules* **2008**, *9*, 2063-2071.
- (155) Waite, C. L.; Sparks, S. M.; Uhrich, K. E.; Roth, C. M. Acetylation of PAMAM dendrimers for cellular delivery of siRNA. *BMC Biotechnology* **2009**, *9*, 1-10.
- (156) Raspaud, E.; Durand, D.; Livolant, F. Interhelical spacing in liquid crystalline spermine and spermidine-DNA precipitates. *Biophysical Journal* **2005**, *88*, 392-403.
- (157) Qiu, X.; Andresen, K.; Lamb, J. S.; Kwok, L. W.; Pollack, L. Abrupt Transition from a Free, Repulsive to a Condensed, Attractive DNA Phase, Induced by Multivalent Polyamine Cations. *Physical Review Letters* **2008**, *101*, 228101.
- (158) An, M.; Hutchison, J. M.; Parkin, S. R.; DeRouchey, J. E. Role of pH on the Compaction Energies and Phase Behavior of Low Generation PAMAM-DNA Complexes. *Macromolecules* **2014**, *47*, 8768-8776.

- (159) Braun, C. S.; Vetro, J. A.; Tomalia, D. A.; Koe, G. S.; Koe, J. G.; Middaugh, C. R. Structure/function relationships of polyamidoamine/DNA dendrimers as gene delivery vehicles. *Journal of Pharmaceutical Sciences* **2005**, *94*, 423-436.
- (160) Boas, U.; Heegaard, P. M. H. Dendrimers in drug research. *Chemical Society Reviews* **2004**, *33*, 43-63.
- (161) Kesharwani, P.; Jain, K.; Jain, N. K. Dendrimer as nanocarrier for drug delivery. *Progress in Polymer Science* **2014**, *39*, 268-307.
- (162) Laznickova, A.; Biricova, V.; Laznicek, M.; Hermann, P. Mono(pyridine-N-oxide) DOTA analog and its G1/G4-PAMAM dendrimer conjugates labeled with Lu-177: Radio labeling and biodistribution studies. *Applied Radiation and Isotopes* **2014**, *84*, 70-77.
- (163) Menjoge, A. R.; Kannan, R. M.; Tomalia, D. A. Dendrimer-based drug and imaging conjugates: design considerations for nanomedical applications. *Drug Discovery Today* **2010**, *15*, 171-185.
- (164) Mignani, S.; El Kazzouli, S.; Bousmina, M.; Majoral, J.-P. Expand classical drug administration ways by emerging routes using dendrimer drug delivery systems: A concise overview. *Advanced Drug Delivery Reviews* **2013**, *65*, 1316-1330.
- (165) Mignani, S.; Majoral, J.-P. Dendrimers as macromolecular tools to tackle from colon to brain tumor types: a concise overview. *New Journal of Chemistry* **2013**, *37*, 3337-3357.
- (166) Pasupathy, K.; Lin, S.; Hu, Q.; Luo, H.; Ke, P. C. Direct plant gene delivery with a poly(amidoamine) dendrimer. *Biotechnology Journal* **2008**, *3*, 1078-1082.
- (167) Perez-Martinez, F. C.; Carrion, B.; Cena, V. The Use of Nanoparticles for Gene Therapy in the Nervous System. *Journal of Alzheimers Disease* **2012**, *31*, 697-710.
- (168) Perez-Martinez, F. C.; Carrion, B.; Lucio, M. I.; Rubio, N.; Herrero, M. A.; Vazquez, E.; Cena, V. Enhanced docetaxel-mediated cytotoxicity in human prostate cancer cells through knockdown of cofilin-1 by carbon nanohorn delivered siRNA. *Biomaterials* **2012**, *33*, 8152-8159.
- (169) Pourianazar, N. T.; Mutlu, P.; Gunduz, U. Bioapplications of poly(amidoamine) (PAMAM) dendrimers in nanomedicine. *Journal of Nanoparticle Research* **2014**, *16*.
- (170) Severson, S.; Tomalia, D. A. Dendrimers in biomedical applications-reflections on the field. *Advanced Drug Delivery Reviews* **2012**, *64*, 102-115.
- (171) Severson, S.; Tomalia, D. A. Commentary - Dendrimers in biomedical applications - reflections on the field. *Advanced Drug Delivery Reviews* **2005**, *57*, 2106-2129.
- (172) Ziemba, B.; Matuszko, G.; Bryszewska, M.; Klajnert, B. Influence of dendrimers on red blood cells. *Cellular & Molecular Biology Letters* **2012**, *17*, 21-35.

- (173) Cheng, Y. Y.; Xu, T. W.; Fu, R. Q. Polyamidoamine dendrimers used as solubility enhancers of ketoprofen. *European Journal of Medicinal Chemistry* **2005**, *40*, 1390-1393.
- (174) Peng, S.-F.; Su, C.-J.; Wei, M.-C.; Chen, C.-Y.; Liao, Z.-X.; Lee, P.-W.; Chen, H.-L.; Sung, H.-W. Effects of the nanostructure of dendrimer/DNA complexes on their endocytosis and gene expression. *Biomaterials* **2010**, *31*, 5660-5670.
- (175) Wu, H. M.; Pan, S. R.; Chen, M. W.; Wu, Y.; Wang, C.; Wen, Y. T.; Zeng, X.; Wu, C. B. A serum-resistant polyamidoamine-based polypeptide dendrimer for gene transfection. *Biomaterials* **2011**, *32*, 1619-1634.
- (176) Zhu, K.; Guo, C.; Xia, Y.; Lai, H.; Yang, W.; Wang, Y.; Song, D.; Wang, C. Transplantation of novel vascular endothelial growth factor gene delivery system manipulated skeletal myoblasts promote myocardial repair. *International Journal of Cardiology* **2013**, *168*, 2622-2631.
- (177) Hussain, M.; Shchepinov, M. S.; Sohail, M.; Benter, I. F.; Hollins, A. J.; Southern, E. M.; Akhtar, S. A novel anionic dendrimer for improved cellular delivery of antisense oligonucleotides. *Journal of Controlled Release* **2004**, *99*, 139-155.
- (178) Intra, J.; Salem, A. K. Fabrication, Characterization and In Vitro Evaluation of Poly(D,L-Lactide-co-Glycolide) Microparticles Loaded With Polyamidoamine-Plasmid DNA Dendriplexes for Applications in Nonviral Gene Delivery. *Journal of Pharmaceutical Sciences* **2010**, *99*, 368-384.
- (179) Kang, C.; Yuan, X.; Li, F.; Pu, P.; Yu, S.; Shen, C.; Zhang, Z.; Zhang, Y. Evaluation of folate-PAMAM for the delivery of antisense oligonucleotides to rat C6 glioma cells in vitro and in vivo. *Journal of Biomedical Materials Research Part A* **2010**, *93A*, 585-594.

## Vita

Min An was born in Datong, Shanxi Province, China.

### Education

Master Degree, Institute of Microbiology Chinese Academy of Sciences, Beijing, 2010

Bachelor Degree, School of Chemical Engineering & Technology, China University of Mining & Technology

### Publications

- (1) An, M., Hutchison, J. M., Parkin, S. R., DeRouchey, J. E. Role of pH on the Compaction Energies and Phase Behavior of Low Generation PAMAM-DNA Complexes. *Macromolecules* 2014, 47, 8768-8776.
- (2) An, M.; Parkin, S. R.; DeRouchey, J. E. Intermolecular forces between low generation PAMAM dendrimer condensed DNA helices: role of cation architecture. *Soft Matter* 2014, 10, 590-599.
- (3) An, M., Gao, F., Qi, J., Li, F., Liu, X. Expression and crystallographic studies of a fungal immunomodulatory protein LZ-8 from a medicinal fungus *Ganoderma lucidum*. *Chinese Journal of Biotechnology*, 2010, 26(11):1563-1568.

### Conference presentations

2013 The 245<sup>th</sup> ACS national meeting & exposition, New Orleans, LA.

2013 The 27<sup>th</sup> Gibbs conference, Carbondale, Illinois.

2013 The 2<sup>nd</sup> Bluegrass molecular biophysics symposium, Lexington, KY

2014 The 66<sup>th</sup> Southeastern Regional Meeting of the American Chemical Society, Nashville, TN.

2014 The 28<sup>th</sup> Gibbs conference, Carbondale, Illinois.

2014 The 3<sup>rd</sup> Bluegrass molecular biophysics symposium, Lexington, KY

### Professional Affiliations

Member of American Chemical Society (ACS) 2013–present

Graduate student in Department of Chemistry, University of Kentucky 2010–present